# Ultrasound Contrast Agents

## acoustic characterization and diagnostic imaging

This thesis was prepared at the laboratory of Experimental Echocardiography, Erasmus University Rotterdam, The Netherlands.

The scientific work presented in this thesis was partly supported by Gist-brocades, Delft, The Netherlands.

Cover illustration: Bubble bonanza

ISBN: 90-9013278-3



Printed by: Optima Grafische Communicatie, Rotterdam.

# Ultrasound Contrast Agents
## acoustic characterization and diagnostic imaging

# Ultrageluids Contrastmiddelen
## akoestische karakterisering en beeldvorming voor de klinische diagnostiek

**PROEFSCHRIFT**

ter verkrijging van de graad van doctor
aan de Erasmus Universiteit Rotterdam
op gezag van de Rector Magnificus
Prof.dr. P.W.C. Akkermans M.A.
en volgens besluit van het College voor Promoties

De openbare verdediging zal plaatsvinden op
woensdag 19 januari 2000 om 15.45 uur

door

**Peter Johan Anton Frinking**

geboren te Bussum

PROMOTIECOMMISSIE

| | |
|---|---|
| **PROMOTOR:** | Prof.dr.ir. N. Bom |
| **OVERIGE LEDEN:** | Dr.ir. N. de Jong, tevens copromotor |
| | Dr. F.J. ten Cate, tevens copromotor |
| | Prof.dr.ir. C.J. Snijders |
| | Prof.dr.ir. J.A.E. Spaan |
| | Prof.dr. H. Torp |

Financial support by the Interuniversity Cardiology Institute of the Netherlands (ICIN) for the publication of this thesis is gratefully acknowledged.

Also, financial contributions of Bracco Research S.A. (Geneva, Switzerland), Schering AG (Berlin, Germany) and GE Vingmed Ultrasound (Horten, Norway) are gratefully acknowledged.

*Voor Barbara*

# Contents

# CHAPTER 1

# General introduction

## 1.1 The heart

The human circulatory system is the transport system that supplies nutrients and oxygen ($O_2$) to the tissues, returns carbondioxide ($CO_2$) to the lungs and other products of metabolism to the kidneys, functions in the regulation of body temperature, and distributes hormones and other agents that regulate cell function[1]. The blood is the carrier of these substances, and is pumped through a closed system of blood vessels (the vascular system) by the heart. At any one time, only 5% of the circulating blood is in the capillaries, but this 5% is in a sense the most important part of the blood volume because it is across the systemic capillary walls that $O_2$ and nutrients enter the interstitial fluid and $CO_2$ and waste products enter the blood stream[2]. The exchange across the capillary walls is essential to the survival of all tissues in the body. Consequently, the pumping action of the heart is fundamental to adequate nutrition of cells and maintenance of the internal environment by blood.

A long-axis cross-section of the heart is shown schematically in figure 1.1. The heart consists of four chambers, *viz.*, the left and right atrium and ventricle, respectively. The ventricular cavities are separated by the septum. The left atrium is separated from the left ventricle by the mitral valve, and the right atrium from the right ventricle by the tricuspid valve. The right side of the heart takes care of the pulmonary circulation, while the left side takes care of the peripheral circulation of the body. For the pulmonary circulation, blood with a low oxygen content flows into the right atrium. Upon relaxation, blood from the right atrium flows into the

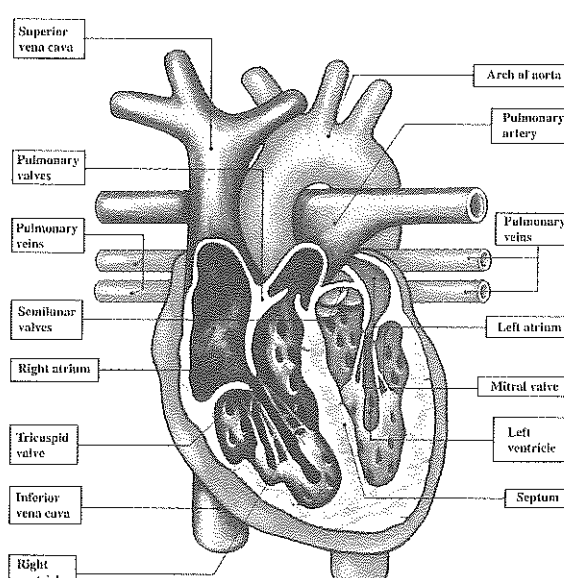


**Figure 1.1** *Schematic long-axis anterier view of a cross-section of the heart. Reprinted with permission (Bryan Edwards Publishing Corp., Anaheim, CA, USA).*

right ventricle, and with the next heart beat it is pumped to the lungs where it is enriched with oxygen. At the same time, blood enriched with oxygen flows from the lungs into the left atrium and ventricle, and subsequently is pumped via the aorta into the body. The heart chambers are covered with a strong muscle, the myocardium, which is responsible for the pumping action of the heart.

The myocardium is supplied with blood through the coronary arteries to fulfill its function. When the blood supply to a portion of the myocardium is reduced, the cells are partially deprived of $O_2$, which is called ischemia. When the blood supply to part of the myocardium is severely compromised, muscle cells die and the area becomes necrotic, *i.e.*, a myocardial infarction occurs[3]. The cause of myocardial infarction is usually occlusion of a coronary artery by a thrombus in a region narrowed by atherosclerotic plaques. Acute myocardial infarction remains one of the most common causes of death in the western world.

Myocardial perfusion is generally assessed using medical imaging modalities that rely on radionuclides, such as positron emission tomography (PET), and single proton emission computed tomography (SPECT). However, these imaging modalities use ionizing radiation, are not repeatable and are expensive. Myocardial contrast echocardiography (MCE), on the other hand, is a new and promising technique that may be used as an alternative to PET and SPECT, and is based on diagnostic ultrasound imaging. Ultrasound imaging has several advantages compared to SPECT and PET, *viz.*, it does not use ionizing radiation, it is repeatable and relatively cheap.

## 1.2 Ultrasound imaging

Diagnostic ultrasound imaging is based on transmitting and receiving sound waves with frequencies ranging from 1–50 MHz. The waves are generated by a transducer consisting of piezo-electric crystals which convert electric signals into ultrasonic pulses[4]. The transmitted wave propagates through a medium until it hits a reflecting object, and the reflected wave is received by the same transducer. The time between transmission and reception is directly related to the distance from the source to the reflecting object by the assumption that the speed of propagation is constant in the medium. Ultrasound can travel through water and soft tissue, and is therefore a suitable technique for non-invasive imaging of structures inside the human body. One of the major benefits is that it is harmless for soft tissue, opposed to X-ray imaging and nuclear imaging techniques. Until now no indications have been found that state otherwise at the energy levels that are currently used in diagnostic ultrasound imaging.

The resolution of ultrasound imaging is directly related to the frequency used, *i.e.*, the higher the frequency the better the resolution will be. However, high frequency ultrasound waves are more attenuated than low frequency ultrasound waves, which limits the penetration depth. Consequently, the frequencies used for imaging are a trade-off between optimal resolution and desired penetration depth. Typical frequencies of 2–7.5 MHz are used to image large organs in the body. The imaging resolution obtained with these frequencies is in the order of millimeters. When the organ that has to be imaged is small and the transducer can be placed close to the region of interest, the frequency can be increased. Typical frequencies for intravascular applications (*i.e.*, from inside a blood vessel) ranges between 20 and 50 MHz, which corresponds to an imaging resolution in the order of 75 $\mu$m.

## 1.3 Ultrasound imaging of the heart

The history of ultrasound in cardiology started in 1954 when Edler and Hertz used a single element transducer to produce an A-mode (amplitude-mode) image on a normal cathode ray tube[5]. In A-mode imaging, the amplitude of an echo is displayed as a function of depth[6]. This important breakthrough initiated the development of new imaging modalities. In M-mode (motion-mode) imaging, the amplitude of an echo is transformed into a grey level, and the positions of the echoes are recorded as a function of time. This enables the study of motion of reflecting structures[5], which is useful especially for imaging moving objects such as the beating heart. The first ultrasound M-mode images of the heart were produced by Edler and Hertz[5]. In the period from 1960 until early 1970 great progress has been made in real-time 2-dimensional (2D) imaging through advances in transducer technology, electronics and theoretical acoustic fundamentals.

A 2D sector image is constructed when the sound beam is swept through the scanning plane, either by mechanical steering (mechanical sector scanners) or by electronical steering (electronic sector scanners). With a mechanical sector scanner, a single acoustic element is mechanically rotated around an axis. In this way, the element is pointed in the desired direction while transmitting the sound pulses and receiving the echoes. In electronic sector scanners, better known as array transducers, which contain several acoustic elements in line, the transducer is fixed in position while the beam is steered electronically. The elements can be activated subsequently, like with linear array transducers[7], resulting in a linear scan. The elements can also be activated almost simultaneously like with phased array transducers, where the phase relations of the individual acoustic elements are changed. By rapid electronic switching, 2D cross-sectional images are created without moving the transducer, and therefore allows real-time imaging. Like with M-mode imaging, the amplitude of the echoes is transformed into grey levels and a B-mode (brightness-mode) image is obtained. In 1968, Somer[8] constructed

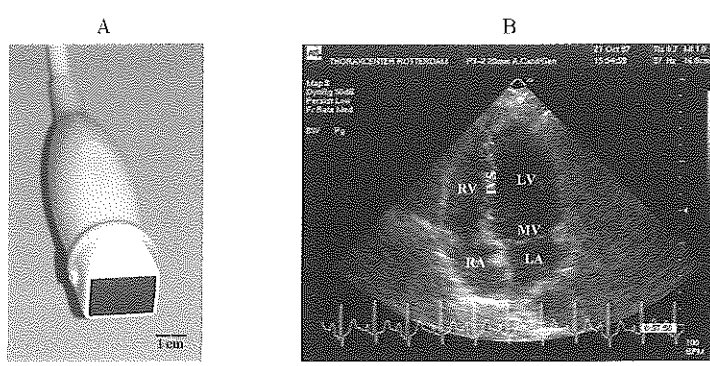


**Figure 1.2** *(A) Image of a trans-thoracic phased array transducer.(B) Typical ultrasound image of the heart, showing an apical four chamber view. RV=right ventricle; RA=right atrium; LV=left ventricle; LA=left ventricle; IVS=intraventicular septum; MV=mitral valve.*

the first phased array transducer for intracranial B-mode imaging. The phased array technique was refined by Thurstone and von Ramm[9], and is still the most widespread technique used in cardiac ultrasound. Three types of transducers that are currently used in echocardiography will briefly be described below.

**Trans-thoracic echocardiography.** When the transducer is placed on the thorax of a patient, the ultrasound scanning technique is called trans-thoracic echocardiography (TTE, figure 1.2). Since the heart is not located near the transducer, relative low ultrasound frequencies (1–5 MHz) are used to obtain enough penetration. However, this results in a limited imaging resolution. Additionally, the sound waves have to pass the ribs and the lungs, which are the main sources of attenuation and artifacts. Therefore, the footprint of a phased array transducer used for cardiac applications is small (figure 1.2A), since it has to be placed between the ribs. With this types of transducer, 2D images of the heart can be obtained as shown in figure 1.2B, where the four heart cavities are clearly depicted.

**Trans-esophageal echocardiography.** The majority of the patients visiting the cardiologist can be screened by means of TTE. However, for some patients it is not possible to obtain echo images of sufficient quality with TTE to allow diagnostic interpretation. In this situation trans-esophageal echocardiography (TEE) may provide definitive diagnostic information[10]. TEE is based on transducer miniaturization which makes it possible to image the heart from the esophagus, *i.e.*, the transducer is swallowed by the patient and positioned right behind the heart. Figure 1.3 shows a pediatric high frequency (7.5 MHz) varioplane TEE transducer[10]. In case of congenital heart diseases, for example, newborn babies of 1 week old can be imaged and diagnosed with this small transducer.

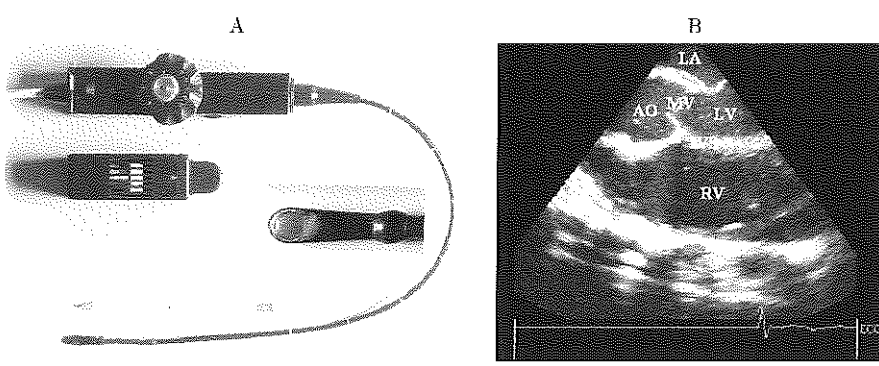


**Figure 1.3** *(A) Pediatric high frequency (7.5 MHz) varioplane TEE probe. (B) Anatomic view of the heart of a baby obtained with the varioplane TEE probe shown in (A). LA=left atrium; AO=aorta; MV=mitral valve; LV=left ventricle; IVS=intraventricular septum; RV=right ventricle.*

The advantage of TEE is that the ultrasound waves are not hampered by the chest wall and echographic artifacts created by the lungs and ribs[11]. Since the transducer is positioned close to the heart, higher frequencies (5–7.5 MHz) can be used, and therefore, a higher imaging resolution can be obtained. Another application of TEE is in the operation room. During

surgery, continuous cardiac monitoring of the left ventricular function can be obtained without intervening with the surgical procedure.

**Intravascular ultrasound.** Small arteries, like coronary arteries, can not be imaged with sufficient resolution with TTE and TEE. Intravascular ultrasound (IVUS) is a technique to acoustically survey arteries from within the lumen by means of a catheter (figure 1.4A). Cross-sectional images of a vessel are generated by sweeping the ultrasound beam sequentially in a 360° scan angle, either mechanically[12] or electronically[13]. With this technique, real-time cross-sectional images of the vessel wall and possible plaque depositions can be obtained[14] (figure 1.4B). IVUS images provide tomographic information of the vessel, contrary to angiographic imaging techniques which only provide a projection of the vessel. Therefore, IVUS provides different diagnostic information as compared to X-ray angiography.

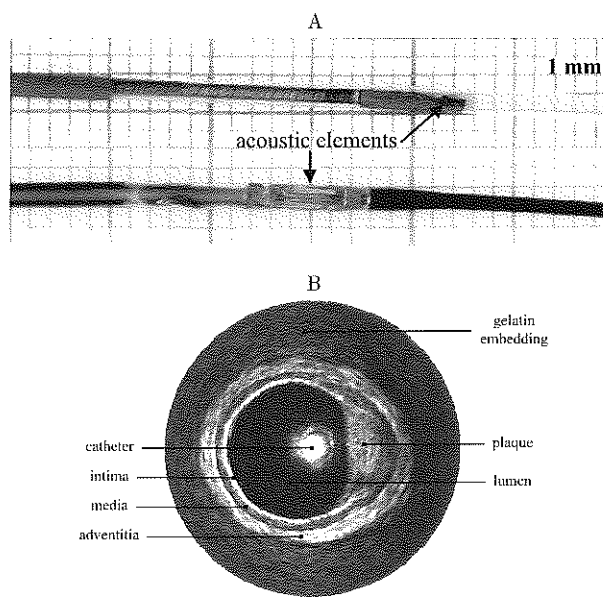


**Figure 1.4** *(A) Intravascular ultrasound catheters (IVUS). Top: mechanical rotating single-element catheter. Bottom: electronically switched phased array catheter consisting of 64 elements (EndoSonics Corporation, Rancho Cordova, CA, USA). IVUS image of an iliac artery (B). The 3-layered structure of the vessel wall, i.e., intima, media and adventitia, and a plaque at 3 o'clock are clearly visible (courtesy E.I. Céspedes, EndoSonics Corporation, Rancho Cordova, CA, USA and C.L. de Korte. Erasmus University, Rotterdam, The Netherlands).*

## 1.4 Ultrasound contrast agents

With TTE, the scattering of blood is low compared to the scattering of surrounding tissue. Normally, blood flow in large vessels is detected with Doppler techniques. Nevertheless, for the

assessment of myocardial perfusion, the scattering of blood is approximately 30–40 dB lower than the scattering of myocardial tissue[15,16]. The scattering of blood can be enhanced by using an ultrasound contrast agent, which allows imaging of organ blood flow.

Contrast echocardiography started when Gramiak and Shah noted that the intracardiac injection of indocyanine green dye produced a cloud of echoes on the M-mode echocardiogram[17]. Moreover, it was noted that the injection of almost any liquid through a small bore needle or catheter would produce this contrast effect. The source of this effect was attributed to the generation of microbubbles during injection as a result of cavitation mechanisms. Currently, some production methods of ultrasound contrast agents are based on the principle of cavitation[18]. Therefore, theoretical expressions describing cavitation have proven to be very useful for understanding the interaction between ultrasound and gas bubbles. Atchley[19] has given an excellent overview of the historical background on cavitation.

Contrast echocardiography is a diagnostic method for the imaging of blood flow within vessels, heart chambers and left ventricular myocardium. Basically two different types of information can be obtained, *viz.*, anatomical information like the distribution of the contrast agent within the heart, and physiological information like changes of flow. From 1980 until now, extensive research has been performed in order to make contrast echocardiography an established diagnostic technique. In the beginning of this period, investigators were forced to use home-made contrast agents. Later on, the first commercial agents became available although still in the experimental stage.

In 1989, Ophir and Parker[20] gave a summary of the use of ultrasound contrast agents in medical imaging. Five types of agents with different physical properties were classified, *viz.*, free gas bubbles, encapsulated gas bubbles, colloidal suspensions, emulsions and aqueous solutions. In those days, it was a main challenge to produce the ideal contrast agent which met the following criteria[21]:

- proportional distribution of the agent within the heart chamber or myocardium according to the blood flow distribution
- stability of the agent to persist during the time of analysis or longer
- small size of the agent (less than 8–10 $\mu$m in diameter) enabling them to pass through the pulmonary system
- constant concentration
- physiological inert

Current contrast agents meet most of these criteria, and have mean diameters ranging between 3–5 $\mu$m. They contain either air or gases that dissolve poorly in the blood. Additionally, the agents can be stabilized by encapsulation to avoid rapid disappearance. More than ten agents are currently under investigation and tested in clinical trails (table 1.1). However, there are only three transpulmonary agents commercially available, *viz.*, Levovist® (Schering AG, Berlin, Germany), Albunex® and Optison™ (Mallinckrodt, St. Louis, USA).

**Table 1.1** *Status of transpulmonary ultrasound contrast agents that are currently under investigation or being evaluated in clinical trails, and commercially available (due to the rapid development of ultrasound contrast agents, this list is likely to be out of date at the time of publication of this thesis; December 1999).*

| Name | Manufacturer | Type (shell / gas) | Status | Available |
|---|---|---|---|---|
| Albunex® | MBI/Mallinckrodt | Sonicated HSA* / Air | Approved | USA / Europe |
| Levovist® | Schering AG | Galactose / Air | FDA not approved / Approved in Europe | Europe / Japan |
| Echogen™ | Sonus/Abbott | Dodecafluoropentane (DDFP) in a sucrose solution | Approved USA / Europe | |
| SonoVue™ | Bracco | Phospholipid / Sulfur hexafluoride | Phase II/III | |
| Optison® | MBI/Mallinckrodt | Sonicated HSA* / Perfluorocarbon | Approved | USA / Europe |
| Quantison™ | Quadrant Ltd. | Spray-dried HSA* / Air | Phase II Europe | |
| Definity™ | Dupont Merck/InaR$_x$ | Liposomes / Perfluorocarbon | FDA approved | |
| Sonazoid™ | Nycomed | Polymer / Sulfur hexafluoride | Phase II Europe | |
| Imagent® | Alliance/Schering | Surfactant membrane / Perfluorohexane - air | Phase III USA | |
| Bisphere® | Point Biomedical | Polymer - HSA* / Air | Phase I | |
| AI-700 | Acusphere Inc. | Polymer (PLGA) / Low solubility gas | Phase I USA | |

* = human serum albumin

## 1.5 Aim and organization of this thesis

As its utilization as an imaging tool, diagnostic ultrasound is second only to X-ray. Ultrasound traditionally has been performed without a contrast agent unlike other forms of diagnostic imaging, such as CT or MRI. However, a considerable number of ultrasound examinations produce suboptimal results. Ultrasound contrast agents have the potential to enhance such images by increasing the contrast between diseased and normal tissue or organs. Better quality images provide physicians with the information they need for a diagnosis and, in many cases, prevent patients from undergoing additional testing.

New contrast-specific detection strategies are continuously being developed and have resulted in improved ultrasound contrast images. However, the "holy grail", *i.e.*, perfusion imaging, still is yielded by disappointing results. The aim of the study described in this thesis was to acoustically characterize ultrasound contrast agents, and to develop a contrast-specific detection strategy based on contrast-specific characteristics.

In chapter 2, a Rayleigh-Plesset-like equation is derived, which describes both the linear and the nonlinear characteristics of shell encapsulated gas bubbles. Experimental results show

that theory and model agree reasonably well for moderate acoustic pressures, for agents like Quantison™, Myomap™ and Albunex®. Of particular interest is, however, the transient enhanced scattering phenomenon, shown by the majority of contrast agents at high acoustic pressures. This phenomenon is described in chapter 3, and explained by a "dualistic" scattering characteristic of the bubbles, which is not shown by tissue and, therefore, is a unique signature for contrast agents.

A novel imaging strategy is introduced in chapter 4, that specifically employs the transient behavior of ultrasound contrast agents. In chapter 5, this imaging method is extended for cardiac applications, *i.e.*, contrast-agent detection within moving tissue. In chapter 6, an overview is given of ultrasound contrast imaging methods that are currently available or under investigation.

As was stated by Tickner[22]: "A non-invasive cath-lab has long been a dream in the medical community". Currently, parameters like blood flow and cardiac pressure are measured invasively by the use of catheters. Determination of blood flow by contrast echocardiography has extensively been studied. In chapter 7, a novel technique is described for non-invasive determination of the local pressure by measuring the disappearance time of free gas bubbles. Free gas bubbles are released from encapsulated gas bubbles, and a pressure disappearance-time relationship is determined. Instead of gas, other compounds like drugs can be released from microspheres. In chapter 8, a preliminary study is presented on ultrasound directed drug delivery by means of microcapsule carriers. This may be a new potential technique for local drug treatment.

Acoustical measurements have already proven to provide useful information about the interaction between ultrasound and the contrast agent. However, optical techniques may provide direct visual information, especially about phenomena that are not fully understood yet, like the transient behavior. In chapter 9, a method is described to study the oscillations of single bubbles in a ultrasound field, in real time. Such a study is of great importance since it could improve and expand our understanding of the interaction between ultrasound and the contrast agent.

# References

1. W. F. Ganong, *Review of medical physiology (pg 414).* Los Altos: Lange Medical Publications, 4th ed., 1969.

2. W. F. Ganong, *Review of medical physiology (pg 468).* Los Altos: Lange Medical Publications, 4th ed., 1969.

3. W. F. Ganong, *Review of medical physiology (pg 443).* Los Altos: Lange Medical Publications, 4th ed., 1969.

4. P. N. T. Wells, *Biomedical Ultrasonics.* London: Academic Press, 1977.

5. I. Edler and C. H. Hertz, "The use of the ultrasonic reflectoscope for the continuous recording of the movements of heart walls," *K. Fysiogr. Sällst. Lund Förshung*, vol. 24, pp. 1–19, 1954.

6. J. J. Wild and J. M. Reid, "Application of echo ranging techniques to the determination of structures of biological tissues," *Science*, vol. 115, p. 226, 1952.

7. N. Bom, C. T. Lancée, J. Honkoop, and P. G. Hugenholtz, "Ultrasonic viewer for cross-sectional analyses of moving cardiac structures," *Biomed Eng*, vol. 6, no. 11, pp. 500–503, 1971.

8. J. C. Somer, "Electronic sector scanning for ultrasonic diagnosis," *Ultrasonics*, vol. 6, no. 3, pp. 153–159, 1968.

9. F. L. Thurstone and O. T. von Ramm, "A new ultrasound imaging technique employing two dimensional electronic beam steering," in *Acoustical Holography and Imaging* (P. S. Green, ed.), vol. 5, pp. 249–259, Plenum Press, 1974.

10. K. K. Djoa, N. de Jong, A. H. Cromme-Dijkhuis, C. T. Lancée, and N. Bom, "Two decades of trans-esophageal phased array probes," *Ultrasound Med Biol*, vol. 22, no. 1, pp. 1–9, 1996.

11. N. de Jong, N. Bom, and C. T. Lancée, "Esophageal echocardiography," in *IEEE Eng Med Biol Soc*, pp. 3–6, 1986.

12. P. N. T. Wells, "Developments in medical ultrasonics," *World Med Electron*, vol. 66, pp. 272–277, 1966.

13. N. Bom, C. T. Lancée, and F. C. van Egmond, "An ultrasonic intracardiac scanner," *Ultrasonics*, vol. 10, pp. 72–76, 1972.

14. E. J. Gussenhoven, C. E. Essed, P. Frietman, F. Mastik, C. T. Lancée, C. Slager, P. W. Serruys, P. Gerritsen, H. Pieterman, and N. Bom, "Intravascular echographic assessment of vessel wall characteristics: A correlation with histology," *Intern J Cardiac Imaging*, vol. 4, pp. 105–116, 1989.

15. K. K. Shung, R. A. Sigelmann, and J. M. Reid, "Scattering of ultrasound by blood," *IEEE Trans Biomed Eng*, vol. 23, no. 6, pp. 460–467, 1976.

16. J. G. Miller, J. E. Perez, and J. G. Mottley, "Myocardial tissue characterization: An approach based on quantative backscatter and attenuation," in *IEEE Ultrason Symp*, pp. 782–793, 1983.

17. R. Gramiak and P. M. Shah, "Echocardiography of the aortic root," *Invest Radiol*, vol. 3, pp. 356–366, 1968.

18. S. B. Feinstein, F. J. ten Cate, W. Zwehl, K. Ong, G. Maurer, C. Tei, P. M. Shah, S. Meerbaum, and E. Corday, "Two dimensional contrast echocardiography. I: *In vivo* development and quantitative analysis of echo contrast agents," *J Am Coll Card*, vol. 3, pp. 14–20, 1984.

19. A. A. Atchley and L. A. Crum, "Acoustic cavitation and bubble dynamics," in *Ultrasound: Its chemical, physical and biological effects* (K. S. Suslick, ed.), pp. 1–64, Weinheim: Verlaggesellschaft, 1988.

20. J. Ophir and K. J. Parker, "Contrast agents in diagnostic ultrasound," *Ultrasound Med Biol*, vol. 15, no. 4, pp. 319–333, 1989.

21. P. Widimsky and F. J. ten Cate, "Contrast echocardiography: Principles and developments," in *Cardiac Ultrasound*, pp. 63–67, 1988.

22. E. G. Tickner, "Precision microbubbles for right site intracardiac pressure and flow measurements," in *Contrast echocardiography* (R. S. Melzter and J. R. T. C. Roelandt, eds.), vol. 15, pp. 313–324, London: Martinus Nijhoff, 1082.

# CHAPTER 2

# Acoustic modeling of shell-encapsulated gas bubbles at moderate acoustic pressures


## Abstract

*Existing theoretical models do not adequately describe the scatter and attenuation properties of ultrasound contrast agents with a relatively thick shell like Quantison™. An adapted version of the Rayleigh-Plesset equation, where the shell is described by a viscoelastic solid, is proposed and validated for this agent. The linear attenuation and scattering properties were predicted based on the measured size distribution. For all the results, the difference between measured and calculated scattering was less than 3 dB. The nonlinear response was minimal because of the high stiffness of the shell. The model was also used for predicting the scatter and attenuation properties of other contrast agents like Myomap™ and Albunex®.*



Based on the publication: "Acoustic modeling of shell-encapsulated gas bubbles" by Peter J.A. Frinking and Nico de Jong. *Ultrasound in Medicine and Biology, vol. 24, no. 4, pp. 523–533, 1998.*

## 2.1 Introduction

Nowadays, conventional diagnostic ultrasound systems provide excellent information of structures and function of different kind of organs. However, low volume flow or very small vessels associated with tumor vascularity often are difficult to detect using current diagnostic ultrasound systems. Furthermore, evaluating the perfusion of tissue to a certain organ currently is not feasible and may, in the future, become possible with the help of ultrasound contrast agents. Crucial criteria for ultrasound contrast agents to be successful include their ability to pass through the lung circulation after an intravenous injection and that they survive the maximum pressure developed in the left ventricle. For passing through the pulmonary system, the diameter should be less than 8–10 $\mu$m [1]. However, free-air bubbles (first generation ultrasound contrast agents) of this size tend to disappear within 1 second[2], depending on the dissolved gas concentration of the liquid. Encapsulating the small gas bubbles by a relatively thin albumin shell (Albunex®, Molecular Biosystems, San Diego, California, USA) or stabilization by galactose and palmitic acid(Levovist®, Schering AG, Berlin, Germany) prevents them from rapid disappearance. These are the so-called second generation agents, which show good opacification of the left ventricle cavity. The third generation contrast agents can be distinguished by prolongation of the life-times either by increasing the stiffness of the bubble shell (Quantison™, Quadrant Ltd., Notingham, UK; Sonovist®, Schering AG, Berlin, Germany) or by using gases that dissolve poorly in blood (Optison™, Molecular Biosystems, San Diego, USA; SonoVue™, Bracco Research S.A., Geneva, Switzerland; Imagent US, Alliance Pharmaceuticals, San Diego, USA; Echogen™, Sonus Pharmaceuticals, Bothell, USA; Aerosomes™, ImaRx Pharmaceuticals, Tucson, USA). Thus, the microbubbles persist for a long time, allowing extensive examinations of heart functions, as well as the micro- and macrovasculatures. Using new technologies such as harmonic imaging[3], these agents allow echographic myocardial opacification.

### Previous related work

Although bubble dynamics has been a field of research since the mid-1800s, a first theoretical description of the behavior of bubbles exposed to an external pressure field was developed by Lord Rayleigh[4]. Since then, much research has been carried out and resulted in an extensive description of the behavior of small gas bubbles under acoustical stimulation. Free gas bubbles are perfect scattering objects for ultrasound[5,6,7]. However, encapsulated gas bubbles behave differently. Changed mechanical properties such as resonance and viscous or friction damping are introduced by the shell and influence the acoustic properties.

de Jong et al.[8,9,10] and de Jong and Hoff[11] developed a theoretical description for the behavior of encapsulated gas bubbles, which was validated by extensive experimental results. Treating the shell as surface layers of elastic solids, they adapted Medwin's[6] approach describing the behavior of resonating gas bubbles, and the Rayleigh-Plesset equation describing the nonlinear motion of encapsulated gas bubbles. By introducing elasticity and shell friction parameters, they calculated the scatter and extinction cross-section of Albunex®. By fitting their theoretical model to transmission measurements, they were able to estimate these two parameters. They concluded that encapsulation results in an increase of the resonance frequency and a decrease

of the scattering amplitude. They also found that the second-harmonic response for Albunex® is 20–30 dB lower than the fundamental response for an acoustic pressure of 50 kPa, and is much lower than for free gas bubbles.

Work done by Church[12] is based on theoretical derivations and describes the effect of encapsulation on individual and collective bubble oscillations. By including the shell as a continuous layer of incompressible solid elastic material, he derived a Rayleigh-Plesset-like equation. The equation predicts that the surface layer supports a strain that counters the Laplace pressure (surface tension) and thereby stabilizes the bubble against dissolution. An analytical solution of this equation was presented, which includes both the fundamental and second-harmonic response. Adapting the dispersion relation, he showed that the change in acoustical velocity in liquids containing suspensions of bubbles is affected by the shell. All examples include the influence of the shell parameter from no shell to a shell elasticity of 150 MPa. For values of 88 MPa for the shell elasticity and 1.77 Pa·s for the shell viscosity, his conclusions agreed with those of the de Jong and Hoff[11] concerning scattering and attenuation of Albunex®.

Hoff[13] proposed an approach describing the shell of the encapsulated bubble by a complex Young's modulus derived from the Kelvin-Voigt model for viscoelastic solids. The stiffness of the shell reduces the compressibility of the particles, resulting in an increase of the resonance frequency. The viscosity of the shell increases the damping constant of the particle-liquid system, decreasing the scattering amplitude. Implementing this in the linear model of Medwin[6], the calculated attenuation spectra were fitted to the measured spectra, giving values for the shell elasticity and viscosity. He concluded that the acoustic attenuation spectra can be predicted with this model.

In this chapter the ultrasound contrast agent Quantison™ is described. First, an overview is given of the basic properties, such as size and mechanical stability. Next, a Rayleigh-Plesset-like equation will be derived describing the scatter and attenuation characteristics as a function of frequency of encapsulated gas bubbles. Experimental results show that theory and model agree reasonably well for Quantison™ as well as for other agents such as Myomap™ (Quadrant Ltd., Nottingham, UK), formerly known as Quantison-Depot™, and Albunex®. All three agents consist of air bubbles encapsulated by an albumin shell. Besides the scatter and attenuation properties, the scattering-to-attenuation ratio ($STAR$), a measure for the scatter effectiveness of the contrast agent, will be discussed. Finally, the second-harmonic response of Quantison™ will be calculated. The models described by de Jong et al.[8,9,10], de Jong and Hoff[11] and Church[12] are limited for predicting the acoustic properties of encapsulated gas bubbles with a relatively thin shell. Therefore, the approach used in this chapter is based on the viscoelastic approach described by Hoff[13]. However, his description is only valid for low acoustic amplitudes, *i.e.*, in the linear range. In this chapter, a more general formula is developed, which describes both the linear and the nonlinear motion of the bubble.

## 2.2 Quantison™

Quantison™ consists of air bubbles encapsulated by a shell of human albumin, which closely resembles native soluble human serum albumin. The shell is formed by spray-drying a solution of human albumin and is stabilized by heat fixation or chemical cross-linking. The final product

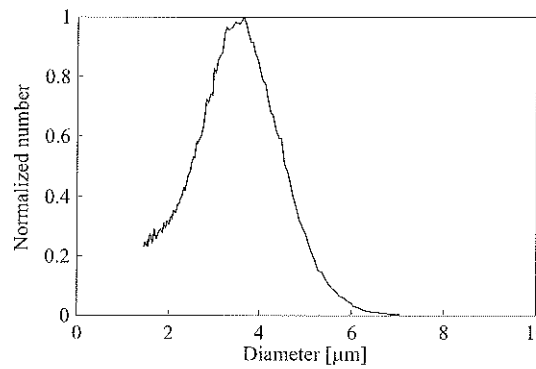


**Figure 2.1** *Normalized size distribution of Quantison™ with diameters ranging from 1.46 to 7 μm. Distribution was measured with the Coulter Counter® Multisizer II with an aperture of 70 μm employing 256 channels.*

is a dry powder that must be resuspended before use. The mean diameter is 3.2 $\mu$m and less than 0.5% of the bubbles are larger than 6 $\mu$m. The size distribution, as measured with a Coulter Counter® Multisizer II (Coulter Electronics, Lutton, UK), is shown in figure 2.1. The shell thickness is 200–300 nm and proportional to the bubble diameter. Figure 2.2 shows an electron microscopic recording of the cross-section of a single fractionated Quantison™ bubble; from this figure the thickness of the shell can be appreciated. As a result of the relatively thick shell, the Quantison™ bubbles are robust and able to withstand static pressures up to 600 mmHg without losing the air it contains. The density of the air-filled bubbles is approximately 780 kg/m$^3$. The particle concentration is about $1.5\times10^9$ bubbles per ml, which corresponds to 8 $\mu$l of air per ml.

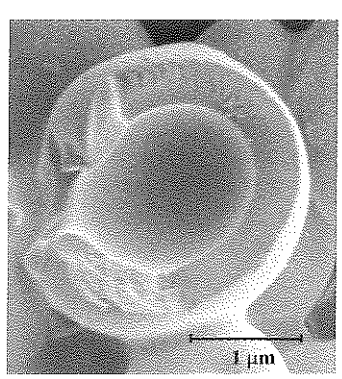


**Figure 2.2** *Electron microscopic view of a "fractionated" Quantison™ microsphere.*

## 2.3 Theory

To examine the dynamics of shell-encapsulated gas bubbles, a model developed by Rayleigh is used as the theoretical basis. The bubble is considered to be spherical and surrounded by an incompressible liquid of infinite extent. The liquid is assumed to be Newtonian, so the viscosity is constant. The bubble volume is defined by a single variable, the radius, and the motion is assumed to be spherically symmetric. The wavelength of the ultrasound field is much larger than the radius of the bubble and only the motion of the bubble surface is of interest. The equation of motion of the bubble wall is given by[14]:

$$\rho R\ddot{R} + \frac{3}{2}\rho\dot{R}^2 = p_L - p_\infty, \tag{2.1}$$

where

$R$ = instantaneous bubble radius
$\dot{R}$ = first time derivative of the radius
$\ddot{R}$ = second time derivative of the radius
$\rho$ = density of the surrounding medium
$p_L$ = liquid pressure at the bubble wall
$p_\infty$ = liquid pressure at infinity.

The liquid pressure at infinity can be expanded to $p_o + P(t)$, with

$p_o$ = hydrostatic pressure
$P(t)$ = time-varying applied acoustic pressure
$t$ = time.

From this point, the present derivation deviates from the standard derivation of the Rayleigh-Plesset equation. The assumption is made that the presence of the shell completely dominates the motion of the bubble wall. Therefore, the bubbles are considered to be elastic particles, which have an effective bulk modulus, $K_{eff}$, describing the elasticity, and a friction parameter, $S_F$, describing the viscosity of the shell. For a spherical volume $V$ deformed by a quasi-static pressure change $\triangle P$, which is uniform over the bubble surface, the volume strain is $-\triangle V/V$ and the effective bulk modulus is given by[15]:

$$K_{eff} = -V\frac{\Delta P}{\Delta V}. \tag{2.2}$$

Since the volume is spherical symmetric and defined by the radius, the volume strain can be written as:

$$\frac{\Delta V}{V} = \left(\frac{R}{R_o}\right)^3 - 1, \tag{2.3}$$

where $R_o$ is the equilibrium bubble radius. Combining equations (2.2) and (2.3) gives:

$$\Delta P = -K_{eff}\left(\left(\frac{R}{R_o}\right)^3 - 1\right). \tag{2.4}$$

The pressure change $\triangle P$, which causes the volume change of the bubble, can be split into three parts: 1) the liquid pressure at the bubble wall ($p_L$), 2) the pressure caused by damping of the bubble-liquid system ($p_d$) and 3) the hydrostatic pressure ($p_o$), giving:

$$\Delta P = p_L + p_d - p_o. \tag{2.5}$$

Substitution of equations (2.4) and (2.5) into equation (2.1), and using the expanded expression for $p_\infty$ yields:

$$\rho R\ddot{R} + \frac{3}{2}\rho\dot{R}^2 = -K_{eff}\left(\left(\frac{R}{R_o}\right)^3 - 1\right) - p_d - P(t). \tag{2.6}$$

An expression for $p_d$ can be derived from the equation of motion of a damped forced oscillator[14], equating the damping pressure, multiplied by the bubble surface, to the damping force:

$$4\pi R^2 p_d = \beta\dot{R}, \tag{2.7}$$

where $\beta$ is the mechanical resistance. Together with the expressions of Medwin[6] for the total damping coefficient, $\delta_{tot} = \beta/(\omega m)$ and the effective mass $m = 4\pi R^3\rho$, the damping pressure can be written as:

$$p_d = \delta_{tot}\rho\omega R\dot{R}, \tag{2.8}$$

where $\omega$ is the angular frequency. Equations (2.6) and (2.8) give the final expression:

$$\rho R\ddot{R} + \frac{3}{2}\rho\dot{R}^2 = -K_{eff}\left(\left(\frac{R}{R_o}\right)^3 - 1\right) - \delta_{tot}\omega\rho R\dot{R} - P(t), \tag{2.9}$$

which is the Rayleigh-Plesset-like equation describing the motion of the wall of an encapsulated gas bubble.

The total damping coefficient $\delta_{tot}$ is the sum of four components,

$$\delta_{tot} = \delta_{rad} + \delta_{vis} + \delta_{th} + \delta_{fr}, \tag{2.10}$$

where the first three terms on the right are described by Medwin[6]:

$\delta_{rad}$ = damping due to reradiation
$\delta_{vis}$ = the damping due to shear viscosity in the surrounding medium
$\delta_{th}$ = the damping due to thermal conductivity.

The last component, $\delta_{fr}$, is the damping due to internal friction or viscosity of the shell and is given by Hoff[16]:

$$\delta_{fr} = \frac{3S_F}{\omega\rho R^2}. \tag{2.11}$$

## Limitations

Comparing equation (2.9) with the standard Rayleigh-Plesset equation for an ideal gas bubble[9], several comments can be made. The vapor pressure is neglected because, for a free-air bubble in water at room temperature, its contribution is only around 1% of the bulk modulus. So, for encapsulated bubbles, which have a higher effective bulk modulus, its contribution will be even smaller. Surface tension is neglected because there is no direct liquid-gas interface. The viscous and reradiation damping coefficients are assumed to be the same as for free gas bubbles, because they occur in the fluid and are independent of the presence of the shell. The presence of the shell has an effect on the thermal damping. It is considered that the shell has a heat capacity that is insufficient to exchange the energy from the gas to the liquid during expansion and compression. This means that there is no substantial net flow of heat into the liquid and that the process is adiabatic. Additional limitations may occur for nonlinear bubble oscillations. The damping coefficients as well as the effective bulk modulus and friction parameter are derived from linear theory and therefore are independent of the applied acoustic pressure.

## Scattering cross-section of a single bubble

The solution of equation (2.9) results in an instantaneous radius, velocity and acceleration of the bubble wall. The scattered sound pressure, $p_s(n\omega)$, at the bubble wall (including higher harmonics) in the frequency domain is[17]:

$$|p_s(n\omega)| = \left|\rho n\omega R_o \dot{R}(n\omega)\right|, \tag{2.12}$$

where $n$ is the harmonic number ($n = 1, 2, 3, ..., 1/2, 1/3, ...$). The scattering cross-section, $\sigma_s(\omega, R)$, is used as the parameter defining the acoustical behavior of the bubble and is defined as the quotient of the scattered power and the incident acoustic intensity. The general expression for the scattering cross-section in the frequency domain including higher harmonics is:

$$\sigma_s(n\omega) = 4\pi R_o^2 \frac{|p_s(n\omega)|^2}{|P(\omega)|^2}, \tag{2.13}$$

where $P(\omega)$ denotes the applied acoustic pressure.

## Mixture of bubbles

For a mixture of bubbles, the scattering cross-section can be calculated under the assumption that: 1) the bubbles are uniformly and homogeneously distributed, and 2) multiple scattering is negligible. Thus, every bubble can be considered as an individual scattering object. For a given size distribution, the scattering cross-section of each individual bubble is multiplied by the respective number of each bubble size. The scattering coefficient (total scattering cross-section

per unit volume), $\mu_s(\omega)$, then is obtained by summation of all the individual contributions according to ($n = 1$):

$$\mu_s(\omega) = \sum_{R_i} N(R_i)\,\sigma_s(\omega, R_i), \tag{2.14}$$

where $N(R_i)$ is the number of bubbles with a radius $R_i$.

The total energy loss or attenuation for an acoustical beam traveling through a screen of bubbles is called the extinction coefficient, $\mu_e(\omega)$, and is given by[8]:

$$\mu_e(\omega) = \mu_a(\omega) + \mu_s(\omega), \tag{2.15}$$

where $\mu_a(\omega)$ is the absorption coefficient. Using the expression for the absorption coefficient derived by Coackly and Nyborg[17]:

$$\mu_a(\omega) = \sum_{R_i} N(R_i)\,\sigma_s(\omega, R_i)\left(\frac{\delta_{tot}(\omega, R_i)}{\delta_{rad}(\omega, R_i)} - 1\right), \tag{2.16}$$

the extinction coefficient is given by:

$$\mu_e(\omega) = \sum_{R_i} N(R_i)\,\sigma_s(\omega, R_i)\frac{\delta_{tot}(\omega, R_i)}{\delta_{rad}(\omega, R_i)}. \tag{2.17}$$

## Scattering-to-attenuation ratio

The attenuation of the acoustical beam traveling through a screen of bubbles can cause shadowing of underlying biological structures and is currently not considered to be a useful parameter. An effective contrast agent, therefore, is defined by good scattering properties and low attenuation. In their work on standardization of ultrasound contrast agents, Bouakaz et al.[18] suggested using, in addition to the backscatter coefficient, the scattering-to-attenuation ratio ($STAR$), as an improved measure for the effectiveness of the contrast agent. The $STAR$ is defined as:

$$STAR(\omega) = \frac{\mu_s(\omega)}{\mu_e(\omega)}. \tag{2.18}$$

Substituting equation (2.15) into equation (2.18) gives:

$$STAR(\omega) = \frac{\mu_s(\omega)}{\mu_a(\omega) + \mu_s(\omega)}, \tag{2.19}$$

where $\mu_s(\omega)$ represents that part of the energy that is scattered away omnidirectionally by the bubbles. On the other hand, $\mu_a(\omega)$ represents that part of the energy that is dissipated by the bubbles. Therefore, the lower the absorption of the incoming plane wave, the higher the $STAR$. A maximum value of $STAR = 1$ is obtained when there is no absorption.

## 2.4 Simulations

Equation (2.9) was solved by using the fourth-order Runga-Kutta method implemented using Matlab® Simulink® (The Mathworks Inc., Natick, USA) running on a personal computer. A fixed step-size was used to simplify fast Fourier transformations (FFT), which is related to the frequency of the applied acoustic wave. A sinusoidal wave was chosen and tapered taking a cosine window for the first five periods to quickly reach a steady-state condition. In this study, an acoustic pressure of 25 kPa was used to calculate the linear response, and an acoustic pressure of 100 kPa was used to calculate the nonlinear response. The initial values at $t = 0$ were $R = R_o$ and $\dot{R} = 0$. FFT was applied on the bubble wall velocity after steady state had been reached. The remainder of the physical constants used were the liquid density, $\rho = 998$ kg/m$^3$ and the liquid viscosity, $\eta = 0.001$ Pa·s. All material properties were determined by their initial conditions and were considered to be constant during bubble oscillation, the lumped constant approach.

## 2.5 Measurements

### Experimental setup

de Jong and Hoff[11] described the measurement set-up that was used for the experiments. Three broadband (100% of the central frequency at the −20-dB level) single-element transducers, with center frequencies of 2, 5 and 10 MHz (Panametrics, Waltham, USA) were used and covered a total frequency band ranging from 1–12 MHz. They were all focused at 75 mm and had apertures of 25, 18 and 12 mm, respectively. The transducers were mounted in a waterbath as illustrated in figure 2.3. Short, single-cycle, pulses were generated and received by a pulser/receiver (5052 PR, Panametrics). The received signals could be amplified from −40 dB to +40 dB. The amplified signals were low-pass filtered to minimize noise and avoid

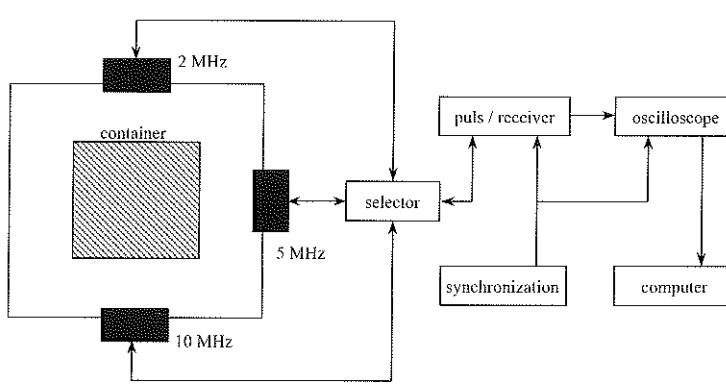


**Figure 2.3** *Schematic setup for acoustic scatter and attenuation measurements.*

aliasing, and were digitized by a LeCroy 9400A (LeCroy, Chestnut Ridge, USA) digital oscilloscope (100 MHz, 8 bits). A pulse generator (PM 5712, Philips, Stockholm, Sweden) was used for synchronization. The signals were recorded over a time window of 10 $\mu$s, with a sampling frequency of 50 MHz, and transferred to a personal computer for further analysis.

The bubble container was made of PMMA (Perspex). The distance from the front to the back wall of the container was 60 mm. The front had an angle of 15° with the acoustical axis of the transducers, to minimize multiple reflections. At the level of the acoustical axis, an acoustical window with a diameter of 40 mm was made of 30-$\mu$m-thick TPX® foil (Mitsui Petrochemical Industries, ltd., Tokyo, Japan). The back wall of the container was used as a flat plate reflector for reference measurements.

## Procedure

The response of the back wall of the container, filled with pure Isoton® II (Isoton® is a particle free phosphate buffered saline with an added dispergent; Coulter Electronics), placed at the focal distance of the transducers, was measured and used as the reference measurement $I_{ref}(\omega)$. Then the contrast agent was added into the container, and the response of the back wall was measured again, $I_{atten}(\omega)$. The relationship between the measured and the calculated attenuation is given by[8]:

$$\frac{I_{atten}(\omega)}{I_{ref}(\omega)} = \exp\left(-\mu_e(\omega)\, d_1\right), \tag{2.20}$$

where $d_1$ is the distance traveled through the bubble container.

To determine the scattering, first the container was repositioned with the front of the container at a distance of approximately 70 mm from the transducers. Then the intensity of the acoustic field scattered by the bubbles, $I_{scatter}(\omega)$, was measured. This measurement was normalized by the reference measurement and corrected for the perspex reflector. The relationship between the measured and the calculated scattering is given by[11]:

$$\frac{I_{scatter}(\omega)}{I_{ref}(\omega)} \frac{16z^2}{D^2} = \mu_s(\omega)\, d_2, \tag{2.21}$$

where

$d_2$ = the window length
$z$ = the distance from the scattering volume to the transducer
$D$ = the diameter of the transducer.

Equation (2.21) includes the correction for the limited aperture of the transducer and is only valid for curved transducers, placing the scattering volume in the focus where the far-field condition is valid. The scattered acoustic field is attenuated by the scatterers themselves as it

travels through the suspension. The scattered signal $A(\omega)$ can be corrected for this attenuation by[11]:

$$A_{corr}(\omega) = A(\omega)\, 10^{\frac{\alpha(\omega) d_z}{10}}, \tag{2.22}$$

where

$A_{corr}(\omega)$ = the corrected scattered signal
$\alpha(\omega)$ = the attenuation at angular frequency $\omega$ (in dB/cm).

Every measurement consisted of 62 traces to obtain a reliable measurement of the scattering of all bubble sizes present in the distribution. After FFT, the average power spectra were calculated and smoothed using a moving window with a width of 200 kHz to remove radio frequency (RF) noise. Before each measurement, the bubble suspension was stirred gently. The repetition rate was set to 1 Hz to ensure that the mixture changed enough to achieve independent scatter spectra from the recorded time traces.

Values for the effective bulk modulus, $K_{eff}$, and the friction parameter of the bubble material, $S_F$ (equation (2.9)), were calculated by fitting the theoretically calculated extinction coefficient to the measured extinction coefficient by minimizing the absolute difference.

## 2.6 Results

The scatter and attenuation properties of Quantison™, Myomap™and Albunex® were measured as described in the measurement section and calculated according to the model described in the theory section. The figures show the measured results and the theoretical results, expressed in dB/cm.

### Scattering and attenuation of Quantison™

Figures 2.4A and 2.4B show the measured transmission (= 1−attenuation) and scattering properties of a 1:250 dilution of resuspended Quantison™, which corresponds to $6.6\times10^6$ microbubbles per ml. The agreement at overlapping frequencies for the different transducers confirms the independence of the measurements on the transducer characteristics. A minimum in transmission at 4 MHz of −3 dB/cm can be clearly appreciated and indicates the resonance frequency. At lower frequencies, a Rayleigh response can be observed, and above 4 MHz the transmission increases with frequency, which is opposite to the behavior of normal biological tissue. Note that the resonance frequency for air bubbles with the same size distribution would be lower than 4 MHz. The resonance frequency for encapsulated gas bubbles is higher due to the presence of the shell. The scattering of the same dilution is depicted in figure 2.4B and shows that the scattering is independent of the frequency above 4 MHz, with a value of −30 dB/cm. For lower frequencies, the scattering increases with frequency, also according to the Rayleigh theory.

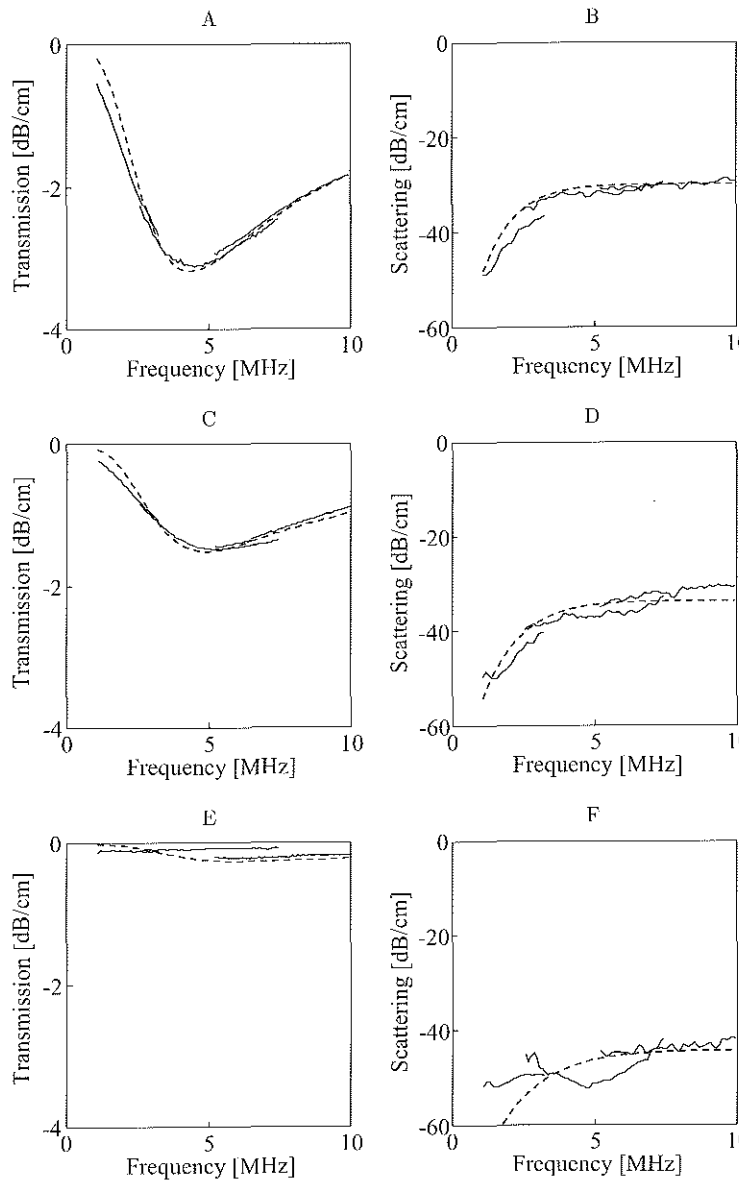


**Figure 2.4** *Transmission and scattering vs. frequency for Quantison™. ——= measured spectrum; -----= calculated spectrum using the size distribution shown in figure 2.1 and bulk modulus $K_{eff}$ = 17.4 MPa and friction parameter $S_F$ = 5.0 Pa·s. A and B are for an unfiltered dilution of 1:250; C and D for a dilution of 1:150, filtered through a 5 μm filter; E and F for a dilution of 1:150, filtered through a 3 μm filter.*

After performing the acoustic measurements, the theoretical transmission curve (dotted line in figure 2.4A) was calculated by using the measured size distribution of the same Quantison™ batch (figure 2.1). Minimizing the absolute difference between the measured and theoretical spectra resulted in values of $K_{eff} = 17.4$ MPa and $S_F = 5.0$ Pa·s. These parameters were then used, together with the size distribution, to calculate the scattering (dotted line in figure 2.4B).

Figures 2.4C–D and 2.4E–F show the results for a filtered Quantison™ dilution of 1:150 ($11 \times 10^6$ microbubbles per ml) with Nuclepore™ (Coster Corp., Cambridge, MA, USA) mechanical filters with pore sizes of 5 and 3 $\mu$m, respectively. Thus, the influence of different parts of the size distribution on the scatter and attenuation characteristics was determined. For the 5-$\mu$m filtered dilution, a less dominant minimum in transmission can still be appreciated at a frequency of 5 MHz. For the 3-$\mu$m filtered dilution, the transmission was practically flat. This indicates that the main contribution to attenuation is due to bubbles larger then 3 $\mu$m in diameter. The results for the scattering show that there is a decrease in scattering level as a function of bubble diameter. Also, there is an increase in frequency, from 4–6 MHz, above which the scattering is independent of the frequency. For both dilutions, the corresponding size distributions were measured with the Coulter Counter® (Coulter Electronics) Multisizer II and used to calculate the theoretical transmission and scattering curves. In both calculations, the same values for the effective bulk modulus and friction parameter were used as determined in figures 2.4A and 2.4B. This means that these parameters are independent of the bubble diameter and results from the fact that the shell thickness is proportional to the bubble diameter. In all experiments, the difference between the measured and calculated scattering was less than 3 dB/cm. For the 3-$\mu$m filtered dilution, it was difficult to measure the scattering below 5 MHz. Because of the low concentration of bubbles after filtering, the scattered signal hardly exceeded the noise level.

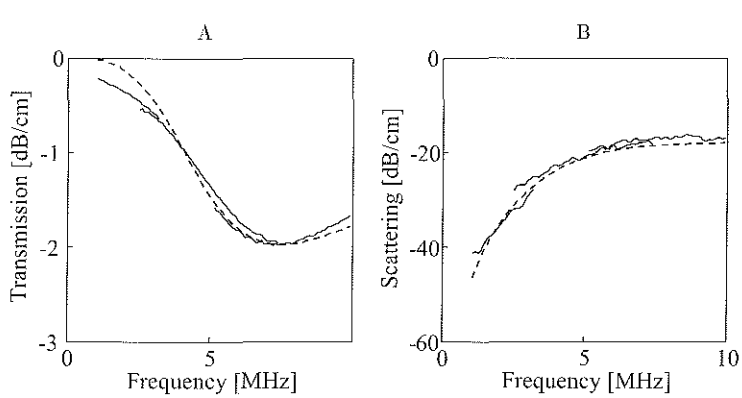


**Figure 2.5** *Transmission (A) and scattering (B) vs. frequency for Myomap™. ——= measured spectrum; -----= calculated spectrum using size distribution shown in figure 2.6. $K_{eff}$ = 78.4 MPa and $S_F$ = 5.1 Pa·s.*

## Scattering and attenuation of Myomap™

Figures 2.5A and 2.5B show the measured and calculated results for a Myomap™ dilution of 1:150 ($1\times10^5$ microbubbles per ml). This agent, which also consists of air bubbles encapsulated by a shell of human albumin such as Quantison™, has a mean size of 10 $\mu$m (figure 2.6). The calculated values for the effective bulk modulus and friction parameter are $K_{eff}$ = 78.4 MPa and $S_F$ = 5.1 Pa·s. The large bulk modulus of Myomap™ is a result of a higher stiffness compared to Quantison™. This is caused by the shell, which is more than three times thicker than the Quantison™ shell. This also explains why, although the bubbles are larger than the Quantison™ bubbles, *i.e.*, expecting a lower resonance frequency, the resonance frequency is higher instead.

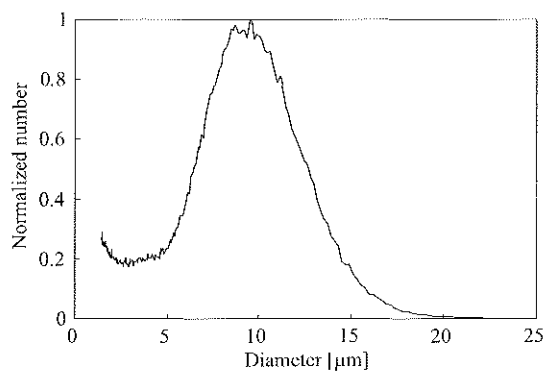


**Figure 2.6** *Normalized size distribution of Myomap™ with diameters ranging from 1.46 to 23.5 µm. Measured with the Coulter Counter® Multisizer II with an aperture of 70 µm employing 256 channels.*

## Scattering and attenuation of Albunex®

Figures 2.7A and 2.7B show the results for Albunex®. The size distribution and results of previously published measurements[11] of filtered Albunex® with a 12-$\mu$m pore size mechanical filter were used for the calculation of the effective bulk modulus and friction parameter. The calculated values are $K_{eff}$ = 1.3 MPa and $S_F$ = 0.1 Pa·s. Also the measurements for Albunex® filtered with 8-, 5- and 3-$\mu$m mechanical filters[11] were used, and the values for $K_{eff}$ and $S_F$ are: 2.0 MPa and 0.1 Pa·s, 6.2 MPa and 0.11 Pa·s and 9.8 MPa and 0.11 Pa·s, respectively. In this case, the effective bulk modulus and friction parameter are dependent on the bubble diameter. This confirms data reported by Hoff[13] and is explained by the fact that the thickness of the Albunex® shell is independent of the diameter, and therefore the stiffness increases for smaller bubbles.

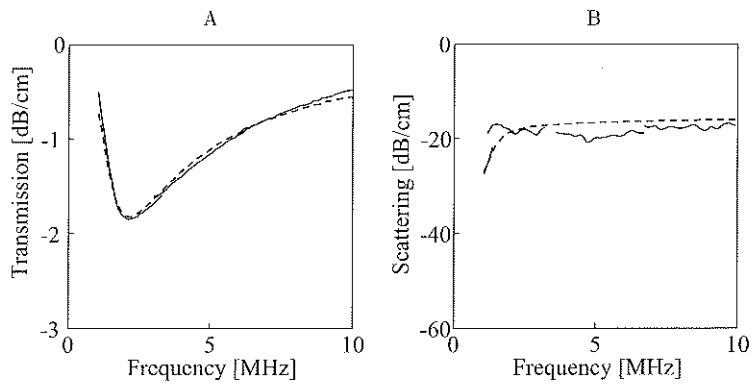


**Figure 2.7** *Transmission (A) and scattering (B) vs. frequency for Albunex®. —— = measured spectrum; -----= calculated spectrum using corresponding size distribution. $K_{eff}$ = 1.3 MPa and $S_F$ = 0.1 Pa·s.*

## *STAR* of Quantison™and Myomap™

Using equation (2.18), the *STAR* was calculated for Quantison™ and Myomap™. The concentrations of the agents was different, nevertheless, for low concentrations and low acoustic pressures, the *STAR* is independent of the concentration. Figure 2.8 depicts a bar graph of the *STAR* at five different frequencies. For Quantison™, the *STAR* is low due to a high stiffness and friction parameter of the shell and increases as a function of frequency. For frequencies between 1 and 10 MHz, which are used for medical diagnosis, the *STAR* is around 0.1%,

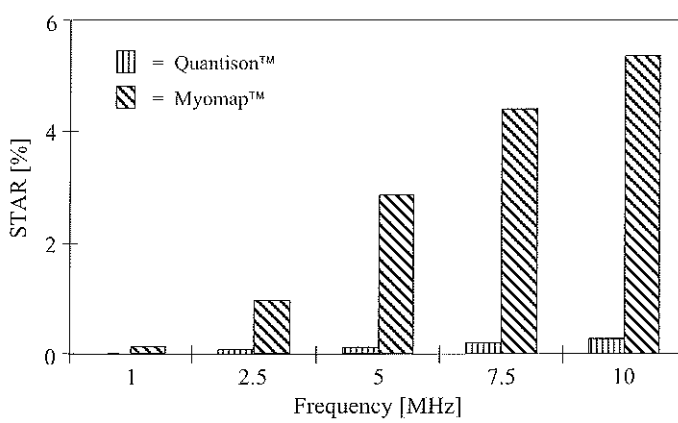


**Figure 2.8** *The scattering-to-attenuation ratio (STAR) for Quantison™ and Myomap™ at frequencies of 1, 2.5, 5, 7.5 and 10 MHz. The variability is around 1% of the values (not shown).*

meaning that the absorption is 1000 times larger than the scattering. For Myomap™, the $STAR$ is higher in spite of a higher stiffness. However, the bubbles are larger and the friction parameter is almost similar to the friction parameter of Quantison™, giving a higher scattering and lower absorption compared to Quantison™. The value of the $STAR$ is around 2–3% at 5 MHz, meaning that the absorption is 50 times larger than the scattering.

### Nonlinear behavior of Quantison™

One of the special characteristics of gas bubbles is that the bubbles start to oscillate non-linearly when the applied acoustic pressure is increased[7,9,19]. However, the nonlinear response of encapsulated bubbles is much smaller. Figure 2.9 shows the result of equation (2.9) for an applied acoustic pressure of 100 kPa, by using $n = 1$ and $n = 2$ in equation (2.13), *i.e.*, calculating the fundamental (figure 2.9A) and second-harmonic responses (figure 2.9B) of Quantison™. A 60-dB difference can be observed between the fundamental and second-harmonic response, and it is obvious from this result that Quantison™ shows negligible second-harmonic response at this acoustic pressure. The lack of harmonic response was confirmed experimentally for applied acoustic pressures up to 100 kPa. No harmonic components above the noise level (−55 dB/cm) could be measured.

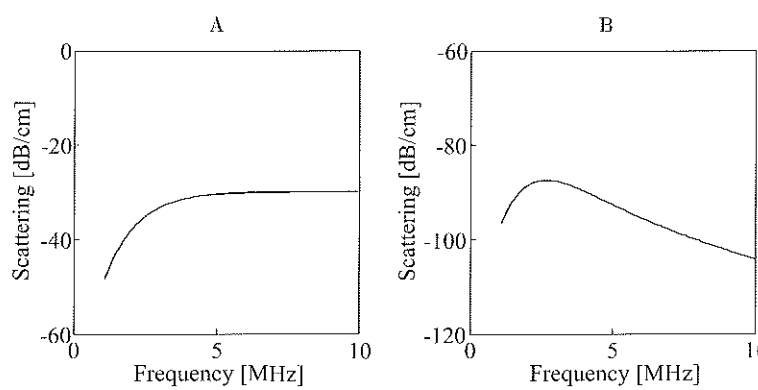


**Figure 2.9** *Calculated scattering spectra of Quantison™ using the size distribution shown in figure 2.1. Bulk modulus $K_{eff}$ = 17.4 MPa and friction parameter $S_F$ 5.0 Pa·s. (A) Fundamental response ($n = 1$ in equation (2.13)); (B) Second-harmonic response ($n = 2$ in equation (2.13)) at an acoustic pressure of 100 kPa.*

## 2.7 Discussion and conclusions

In this chapter, the idea introduced by Hoff[13] to treat the shell of an encapsulated gas bubble as a viscoelastic solid was expanded to a Rayleigh-Plesset-like equation. The effective bulk modulus and friction parameter, describing the elasticity and viscosity of the shell, were found

by fitting the calculated transmission spectrum to the measured transmission spectrum. These parameters were subsequently used to calculate the scattering. With the same model, the transmission and scattering of the ultrasound contrast agents Quantison™, Myomap™ and Albunex® were calculated. For all the results, the difference between measured and calculated scattering was less than 3 dB/cm.

The effective bulk modulus of Quantison™ (17.4 MPa) is 124 times the bulk modulus of air, which is 0.14 MPa at adiabatic conditions and an ambient pressure of 1 atm. However compared to water (2250 MPa), this is only 0.7%. For Albunex®, the effective bulk modulus (1.3 MPa) is nine times the bulk modulus of air. This demonstrates the dominant character of the shell, even for an encapsulated gas bubble with a very thin shell[12].

For Quantison™, the shell thickness is proportional to the bubble diameter, meaning that the stiffness and, therefore, the effective bulk modulus, are independent of the bubble diameter. For Albunex®, however, the shell thickness is independent of the bubble diameter[8], *i.e.*, the stiffness increases for smaller bubbles. This means that the effective bulk modulus is depending on the bubble diameter and increases with decreasing bubble diameter. The dependence of the effective bulk modulus of Albunex® on the bubble diameter also is reported by Hoff[13].

With previous models[8,9,11,12] it is not possible to calculate the transmission and scattering of Quantison™ and Myomap™. Both models were specifically developed for Albunex®, *i.e.*, encapsulated gas bubbles with a relatively thin shell. The thin-shell assumption is not valid for agents where the shell comprises a considerable part of the bubble volume (e.g. Quantison™ and Myomap™). The fact that the transmission and scattering of Albunex® can be calculated with the present model, indicates that this model may be used for agents with a thick or thin shell.

The assumptions made to neglect vapor pressure and surface tension should be reconsidered for modeling other agents. Different methods for stabilizing the gas can have an effect on these assumptions. Also, a substantial net flow of heat into the liquid may occur in these situations. This means that the process should be considered polytropic instead of adiabatic. For free gas bubbles, however, the model described in this chapter no longer holds and the standard Rayleigh-Plesset equation should be used.

The *STAR* can be used to describe the acoustic efficiency of ultrasound contrast agents. The *STAR* of Quantison™ and Myomap™ was calculated and ranges from 0.1%–5% for frequencies between 1 and 10 MHz. The *STAR* for Albunex® ranges from 2% to 18%[18] in the same frequency range. This means that Albunex® shows a higher acoustical efficiency than Quantison™. However, these values are only valid for low acoustic pressures. At high acoustic pressures, nonlinear transient effects appear. It has been reported that for acoustic pressure higher than 200 kPa, the measured scattering coefficient of Quantison™ abruptly increases[20,21]. The increase is transient and reaches a level of 20 dB for an acoustic pressure of 1.8 MPa, and can not be predicted by the theoretical model described in this chapter (figure 2.10). Measurement and calculation agree for applied pressures less than 200 kPa. For applied pressures above 200 kPa the measurement and calculation deviate.

In figure 2.9, it is shown that Quantison™ shows hardly any second-harmonic response at an acoustic pressure of 100 kPa. Even for acoustic pressures up to 2 MPa, the model described in this chapter predicts a second-harmonic response that still does not exceed the

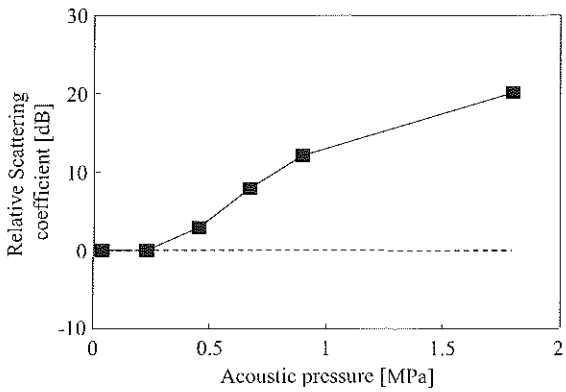


**Figure 2.10** *Relative measured (——) and calculated (-----) scattering coefficient of Quantison™ as a function of the applied acoustic pressure.*

noise level of −55 dB/cm. However, it has been reported[20,21] that, above an acoustic pressure of 200 kPa, the spectrum of the measured scattering signal broadens up and contains harmonics with amplitudes comparable to the amplitude of the fundamental frequency.

We have developed a theoretical model that predicts accurately the linear and nonlinear response of encapsulated gas bubbles. However, the model does not predict the abrupt increase in scattering at applied acoustic pressures above 200 kPa (figure 2.10). An explanation is that, at these high acoustic pressures, free-air bubbles are released from the Quantison™ microspheres. This phenomenon is described in detail in the next chapter.

# References

1. J. C. Hogg, "Neutrophil kinetics and lung injury," *Physiological review*, vol. 67, no. 4, 1987.

2. P. S. Epstein and M. S. Plesset, "On the stability of gas bubbles in liquid-gas solutions," *J Chemical Physics*, vol. 18, no. 11, pp. 1505–1509, 1950.

3. P. N. Burns, J. E. Powers, and T. Fritzsch, "Harmonic imaging: A new imaging and Doppler method for contrast enhanced ultrasound," *Radiology*, vol. 185 (P), p. 142, 1992.

4. Lord Rayleigh (J. W. Strutt), "On the pressure developed in a liquid during the collapse of a spherical cavity," *Philos Mag*, vol. 34, pp. 94–98, 1917.

5. A. L. Anderson and L. D. Hampton, "Acoustics of gas-bearing sediments 1. Background," *J Acoust Soc Am*, vol. 67, no. 6, pp. 1865–1889, 1980.

6. H. Medwin, "Counting bubbles acoustically: A review," *Ultrasonics*, no. 1, pp. 7–13, 1977.

7. D. L. Miller, "Ultrasonic detection of resonant cavitation bubbles in a flow tube by their second-harmonic emissions," *Ultrasonics*, pp. 217–224, 1981.

8. N. de Jong, L. Hoff, T. Skotland, and N. Bom, "Absorption and scatter of encapsulated gas filled microspheres: Theoretical considerations and some measurements," *Ultrasonics*, vol. 30, no. 2, pp. 95–103, 1992.

9. N. de Jong, R. Cornet, and C. T. Lancée, "Higher harmonics of vibrating gas filled microspheres. Part one: Simulations," *Ultrasonics*, vol. 32, pp. 447–453, 1994.

10. N. de Jong, R. Cornet, and C. T. Lancée, "Higher harmonics of vibrating gas filled microspheres. Part two: Measurements," *Ultrasonics*, vol. 32, pp. 455–459, 1994.

11. N. de Jong and L. Hoff, "Ultrasound scattering properties of Albunex® microspheres," *Ultrasonics*, vol. 31, no. 3, pp. 175–181, 1993.

12. C. C. Church, "The effect of an elastic solid surface layer on the radial pulsations of gas bubbles," *J Acoust Soc Am*, vol. 97, no. 3, pp. 1510–1521, 1995.

13. L. Hoff, "Acoustic properties of shell-encapsulated, gas filled ultrasound contrast agents," in *IEEE Ultrason Symp*, vol. 2, (San Antonio, USA), pp. 1441–1444, 1996.

14. T. G. Leighton, *The acoustic bubble*. London: Academic Press, 1994.

15. D. Tabor, *Gasses, liquids and solids*. New York: Cambridge University Press, 1987.

16. L. Hoff, "Acoustic properties of ultrasonic contrast agents," *Ultrasonics*, vol. 34, no. 2–5, pp. 591–593, 1996.

17. W. T. Coakley and L. N. Nyborg, "Cavitation: Dynamics of gas bubbles; applications," in *Ultrasound: Its applications in medicine and biology* (F. J. Fry, ed.), vol. 3, pp. 77–159, Amsterdam: Elsevier Scientific Publishing Company, 1978.

18. A. Bouakaz, N. de Jong, and C. Cachard, "Standard properties of ultrasound contrast agents," *Ultrasound Med Biol*, vol. 24, no. 3, pp. 469–72, 1998.

19. B. Schrope, V. L. Newhouse, and V. Uhlendorf, "Simulated capillary blood flow measurements using a nonlinear ultrasonic contrast agent," *Ultrasonic Imaging*, vol. 14, no. 2, 1992.

20. N. de Jong, P. J. A. Frinking, F. J. ten Cate, and P. van der Wouw, "Characteristics of contrast agents and 2D imaging," in *IEEE Ultrason Symp*, vol. 2, (San Antonio, USA), pp. 1449 1458, 1996.

21. P. J. A. Frinking and N. de Jong, "Modelling of ultrasound contrast agents," in *IEEE Ultrason Symp*, vol. 2, (Toronto, Canada), pp. 1601 1604, 1997.

# CHAPTER 3

# Scattering properties of encapsulated gas bubbles at high ultrasound pressures


## Abstract

*Encapsulated types of contrast agents possess a specific acoustic signature. When the applied acoustic pressure exceeds a threshold, the scattering level increases abruptly for a short time. A "dualistic" character of the encapsulated gas bubbles explains this signature for Quantison™ (air bubbles encapsulated by a shell of human albumin). For acoustic pressures below the threshold, the bubbles act as encapsulated gas bubbles and are stable linear or nonlinear scatterers, depending on the applied acoustic pressure. For acoustic pressures above the threshold, the bubbles rupture and release the contained gas, subsequently acting as a free gas bubbles. The effect is transient and lasts until the released free gas bubbles are dissolved in the surrounding liquid. This explanation was investigated experimentally and evaluated by theoretical models. A 15–20-dB increase in scattering, the appearance of higher harmonics, and a finite duration of the effect was measured and agreed with corresponding theory. Therefore, ultrasound in combination with this "dualistic" character suggests that encapsulated gas bubbles can be construed as a robust vehicle for localized delivery of free gas bubbles, the ultimate ultrasound contrast agent.*



Based on the publication: "Scattering properties of encapsulated gas bubbles at high ultrasound pressures" by Peter J.A. Frinking, Nico de Jong and E. Ignacio Céspedes. *Journal of the Acoustical Society of America, vol. 105, no. 3, pp. 523–533, 1999.*

## 3.1 Introduction

The most important purpose of ultrasound contrast agents, up till a few years ago, was to enhance the acoustic signal from blood-filled regions. This allows better characterization of perfusion and blood flow for B-mode images and for Doppler modes. Nowadays, new imaging

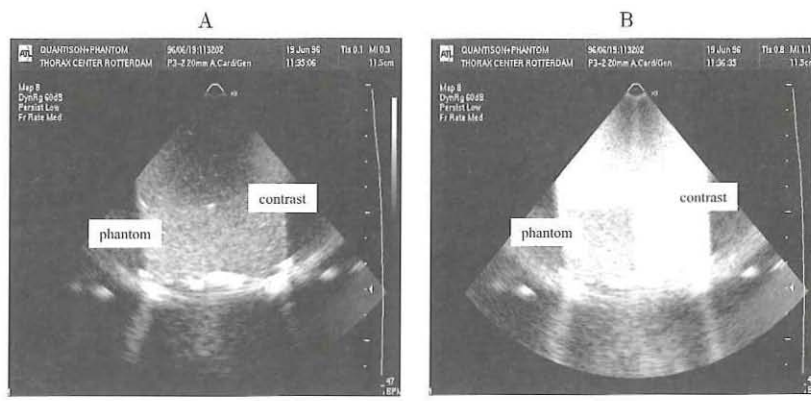


**Figure 3.1** *B-mode images of Quantison™ and a tissue-mimicking phantom made of 1% agar and 0.5% Carborundum (SiC) scatterers (particle sizes ranging from 5–8 μm). (A) MI=0.3. (B) MI=1.1.*

techniques are being explored that take advantage of the nonlinear acoustic property of the bubbles, like second-harmonic imaging[1,2]. With these techniques, the discrimination between contrast and surrounding tissue can be improved. This becomes quite apparent for increased acoustic pressures and small bubbles[3]. However, due to the presence of a shell, the scatter efficiency and nonlinear response of encapsulated gas bubbles are much lower than for free gas bubbles[4,5,6] (chapter 2). The shell serves as a stabilizing goal, since the life span of free gas bubbles, the ultimate ultrasound contrast agent, is limited.

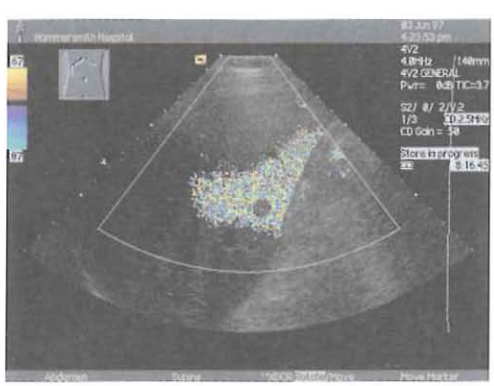

**Figure 3.2** *Loss-off-correlation imaging of Levovist® in the liver. The mosaic color pattern is caused by random Doppler shifts due to agent rupture. Note the absence of the mosaic pattern in the small lesion (courtesy: D.O. Cosgrove, Hammersmith Hospital, London, UK).*

Nevertheless, encapsulated types of contrast agents (e.g. Sonovist®, Schering AG, Berlin, Germany and Quantison™, Quadrant Ltd., Nottingham, UK) possess a specific acoustic signature[7,8]. When the applied acoustic pressure exceeds a specific threshold, the scattering level increases abruptly for a short time. In conventional B-mode imaging, this transiently enhanced scattering is visualized as an increased echogenicity (figure 3.1) and in Color Doppler imaging as a colored mosaic map that is detectable even without flow (figure 3.2). Furthermore, the scattered signal becomes highly nonlinear and is very well suited for second-harmonic imaging. This particular signature has been addressed by several names, *viz.*, acoustically stimulated acoustic emission[7], power enhanced scattering[8], flash echo imaging[9], scintillation sonography[10], etc. The effect, however, is transient, and most effective when the ultrasound wave hits the bubbles for the first time. This has led to the development of intermittent imaging[11] as a new imaging modality, where single scans are made at regular time intervals (e.g. 0.2 1 Hz), resulting in an increased efficacy of the agent. Despite the variety of given names, it seems that the acoustic signature observed for different contrast agents is comparable and generally associated with bubble rupture and enhanced scattering.

Takeuchi[10] reported similar effects observed with thermoplastic (poly-vinylidenchloride-acryluitoryl) micro balloons as a mimicking contrast agent. Bright echoes, harmonic response and spectral broadening as observed with normal contrast agents are described. The effects are explained by shell breakage, followed by release of the encapsulated gas, and last for 1–5 ms, equivalent to the dissolution time of the gas in the surrounding liquid.

In this chapter, the phenomenon observed for Quantison™ is explained by a "dualistic" character of the encapsulated gas bubbles, which is related to the applied acoustic pressure. For low acoustic pressures, below a threshold, the bubbles act as encapsulated gas bubbles and are stable linear or nonlinear scatterers, depending on the applied acoustic pressure. For acoustic pressures above the threshold, the bubbles rupture and release the contained gas, subsequently acting as a free gas bubbles. The irreversible effect is transient and lasts until the released free gas bubbles are dissolved in the surrounding liquid. This explanation is supported by three experiments and corresponding theoretical models. First, the enhancement of the scattering is measured and simulated using a free gas bubble model. Second, the appearance of higher harmonics are measured and simulated according to the same model, since it has been shown that for free gas bubbles the nonlinear response is superior compared to encapsulated gas bubbles[5,6]. Finally, the finite duration of the effect is measured and related to the theoretical persistence of the generated free gas bubbles. This is demonstrated by comparing the measured disappearance time of the gas bubbles to calculated values.

## 3.2 Theory

### Enhanced scattering

The Rayleigh-Plesset (RPNNP) equation is used as a free gas bubble model. The bubble is considered to be spherically symmetric and surrounded by a liquid of infinite extent, with a constant viscosity. The bubble volume is defined by a single variable, the radius, and the motion is assumed to be spherically symmetric. The wavelength of the ultrasound field is assumed to be

much larger than the bubble diameter, and only the motion of the bubble surface is of interest. It is assumed that the vapor pressure remains constant during the compression and expansion phase, and that there is no rectified diffusion during the short period of exposure to ultrasound. The gas in the bubble is assumed to be ideal and compressed and expanded according to the ideal gas law with the polytropic exponent $\Gamma$ remaining constant during vibration. The final expression for the RPNNP equation is given by[6]:

$$\rho R\ddot{R} + \frac{3}{2}\rho\dot{R}^2 = p_{go}\left(\frac{R_o}{R}\right)^{3\Gamma} + p_v - p_o - \frac{2\sigma}{R} - \delta_{tot}\omega\rho R\dot{R} - P(t), \tag{3.1}$$

where

$R$ = instantaneous bubble radius
$\dot{R}$ = first time derivative of the radius
$\ddot{R}$ = second time derivative of the radius
$\rho$ = density of the surrounding medium
$R_o$ = initial bubble radius
$p_{go}$ = initial gas pressure in the bubble
$\Gamma$ = polytropic exponent of the gas
$p_v$ = vapor pressure
$p_o$ = ambient pressure
$\sigma$ = surface tension
$\delta_{tot}$ = total damping coefficient
$\omega$ = angular frequency of the applied acoustic field
$P(t)$ = time-varying applied acoustic pressure
$t$ = time.

The initial gas pressure inside the bubble, $p_{go}$, is given by:

$$p_{go} = \frac{2\sigma}{R_o} + p_o - p_v, \tag{3.2}$$

and the expression for the total damping coefficient is given by:

$$\delta_{tot} = \delta_{rad} + \delta_{vis} + \delta_{th}, \tag{3.3}$$

where

$\delta_{rad}$ = damping coefficient due to reradiation
$\delta_{vis}$ = damping coefficient due to viscosity of the surrounding medium
$\delta_{th}$ = damping coefficient due to heat conduction.

Expressions for the damping coefficients and for the polytropic exponent are given by Medwin[12]. After solving equation (3.1) numerically, the scattering cross-section, defined as the scattered power by the bubble divided by the incident acoustic intensity, can be calculated as described in chapter 2 equation (2.13).

## Nonlinear response

In addition to the increase in scattered power at the fundamental frequency, the scattered power at higher harmonic components of the fundamental frequency increases as well for free gas bubbles compared to encapsulated gas bubbles[5,6]. Free gas bubbles oscillate non-linearly when the applied acoustic pressure is increased, an effect that becomes extremely apparent for bubbles smaller than 10 $\mu$m in diameter[3]. For example, for an applied acoustic pressure of 50 kPa, a 3-$\mu$m diameter free-air bubble, insonified at 1-MHz, shows harmonic components that can exceed the scattering level at the fundamental frequency. This strong harmonic behavior is predicted by equation (3.1). For encapsulated gas bubbles, the effect is subdued as a result of the extra damping introduced by the shell. For Quantison™, it has been shown that for an acoustic pressure of 100 kPa, the second-harmonic response is more than 60 dB below the fundamental response (chapter 2, figure 2.9).

## Disappearance time

Small free gas bubbles tend to disappear quickly in a liquid, e.g. air bubbles of 2 $\mu$m in diameter persist for only a few milliseconds in a saturated liquid under normal conditions[13]. With the omission of translatory bubble motion, the change in equilibrium radius over time is given by:

$$\frac{dR}{dt} = DL\left(\frac{\frac{C_i}{C_o} - 1 - \frac{2\sigma}{Rp_o}}{1 + \frac{4\sigma}{3Rp_o}}\right)\left(\frac{1}{R} + \frac{1}{\sqrt{\pi Dt}}\right), \tag{3.4}$$

where

$R$ = bubble radius
$t$ = time
$D$ = diffusion coefficient
$L$ = Ostwald coefficient
$\frac{C_i}{C_o}$ = ratio of the dissolved gas concentration to the saturation concentration
$\sigma$ = surface tension
$p_o$ = ambient pressure.

The surface tension (first bracketed term in equation (3.4)) is the mechanism responsible for the disappearance of a gas bubble in a gas-saturated liquid. The second bracketed term resembles the penetration depth that denotes how far the gas diffuses into the liquid. The diffusion constant is a property of the gas and the surrounding liquid. The Ostwald coefficient is the ratio of the amount of gas per unit volume dissolved in the surrounding liquid and in the gas phase[14]. The diffusion coefficient and the Ostwald coefficient determine the rate of decrease of the bubble radius, which is a direct measure for the disappearance rate of the bubble. Thus, microbubbles filled with gases having smaller diffusion and Ostwald coefficients will persist longer.

## 3.3 Experimental setup and procedure

For all the experiments, the contrast agent Quantison™ was used. The acoustic characteristics, like scattering and attenuation, at moderate acoustic pressures, has been described in chapter 2.

### Enhanced scattering

The experimental setup is illustrated in figure 3.3. A 0.5- or 1-MHz single element transducer (Panametrics, Waltham, USA) focused at 75 mm, with an aperture of 37 mm, was mounted in a water tank. These transducers were used to transmit a high-amplitude ultrasound burst (acoustic pressure of 1.6 MPa). The peak negative acoustic pressures were measured with a calibrated hydrophone (PVDFZ44-0400, Specialty Engineering Associates, Soquel, USA). A sine wave burst, 10 cycles, was generated by a Wavetek signal generator (Wavetek I, model 144, Wavetek, San Diego, USA) and amplified by a 60-dB linear power amplifier (A-500, ENI, Rochester, USA). The amplitude was adjusted by a separate variable attenuator (355C/D, HP, Palo Alto, USA). Two broadband (100% of the central frequency at the −20-dB level) single element transducers, with center frequencies of 2 and 5 MHz (Panametrics) were mounted perpendicularly to the first transducer. The two transducers cover a combined frequency band from 1 to 7.5 MHz. They are both focused at 75 mm and have apertures of 25 and 18 mm, respectively. Short, single-cycle, low-amplitude pulses (acoustic pressure of 100 kPa) were generated, 0.6 ms after the high-amplitude burst, and received by a pulser/receiver (5052 PR, Panametrics). The received signals could be amplified from −40 dB to +40 dB by the pulser/receiver. The amplified signals were low-pass filtered to minimize noise and avoid aliasing, and were digitized by a LeCroy 9400A (LeCroy, Chestnut Ridge, NY, USA) digital oscilloscope (100 MHz, 8 bits). The signals were recorded over a time window of 10 $\mu$s, were sampled at 50 MHz, and transferred to a personal computer for further analysis. Two pulse generators (pulser I and

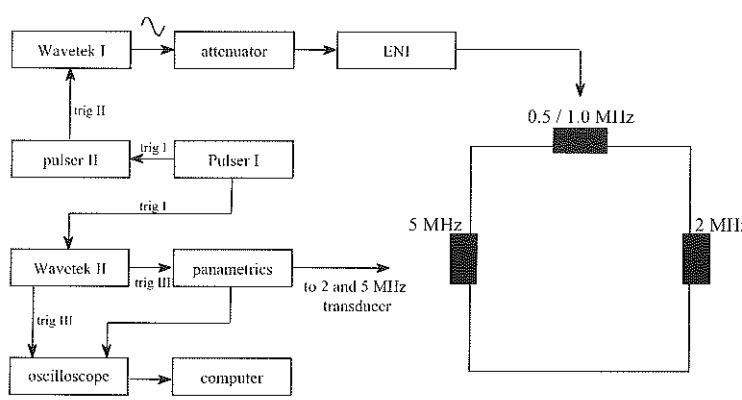


**Figure 3.3** *Schematic setup for measuring the enhanced scattering.*

II, PM 5712, Philips, Stockholm, Sweden) and a Wavetek signal generator (Wavetek II, model 144, Wavetek,) were used for synchronization. The triggering sequences are shown in figure 3.4A.

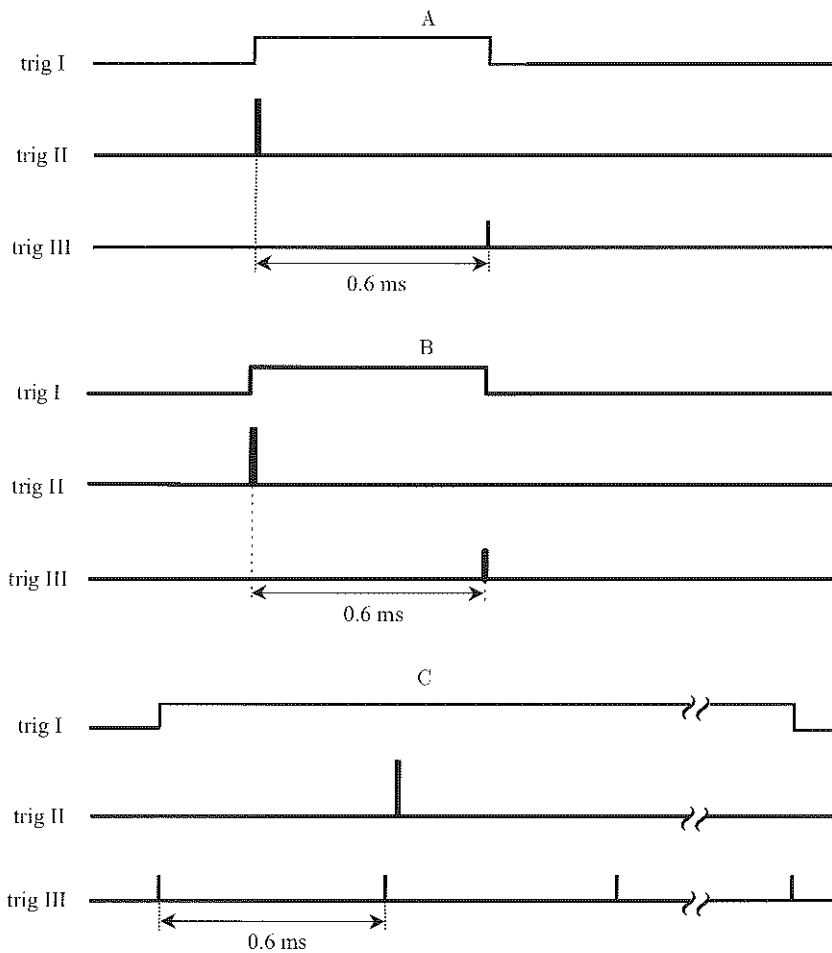


**Figure 3.4** *Schematic representation of the triggering sequences used. (A) The enhanced scattering was measured 0.6 ms after transmission of the high acoustic amplitude burst. (B) The same as (A), only the duration of the low acoustic amplitude burst was set to 10 µs. (C) By changing the frequency of Wavetek II to 1.6 kHz, the enhanced scattering could be measured with a PRI of 0.6 ms after the high acoustic amplitude burst, to monitor the disappearance of the bubbles. Note that the high-amplitude burst was transmitted immediately after the second low-amplitude pulse.*

The experiments were conducted at room temperature. The water tank was filled with Isoton® II (Coulter Electronics, Lutton, UK), which was left standing overnight and therefore was air saturated. The response of a steel flat-plate reflector, placed at the focal distance of the 2 and 5 MHz transducer, was measured and used as a reference measurement. After that, the contrast agent was added and the response of the steel flat-plate reflector was measured again, to determine the additional attenuation caused by the contrast agent. The intensity of the scattered acoustic field with and without the high amplitude burst was measured and the scattering cross-section was determined, taking into account the reflection properties of the steel flat-plate reflector, the transducer characteristics, and the attenuation of the contrast agent itself (chapter 2). The scattering cross-section was calculated by averaging 62 independent measurements. After fast Fourier transformation (FFT), the average power spectra were calculated and smoothed using a moving window with a width of 200 kHz to remove radio frequency (RF) noise. During the measurement, the bubble suspension was continuously stirred by a magnetic stirrer.

## Nonlinear response

Figure 3.5 shows the setup used for measuring the nonlinear response with and without the high-amplitude burst (acoustic pressure of 1.6 MPa). The burst was generated as described in the previous section with the 0.5 MHz transducer. A narrow-band sine wave (1 MHz; 10 cycles) was generated by a Wavetek signal generator (Wavetek II, model 144, Wavetek) and amplified (acoustic pressure of 100 kPa) by a linear power amplifier (ARS 05-40-40, Orsay, France). This signal was directed to a 1-MHz single-element, broadband transducer (100% of the central frequency at the −20-dB level), with an aperture of 37 mm, that was mounted in

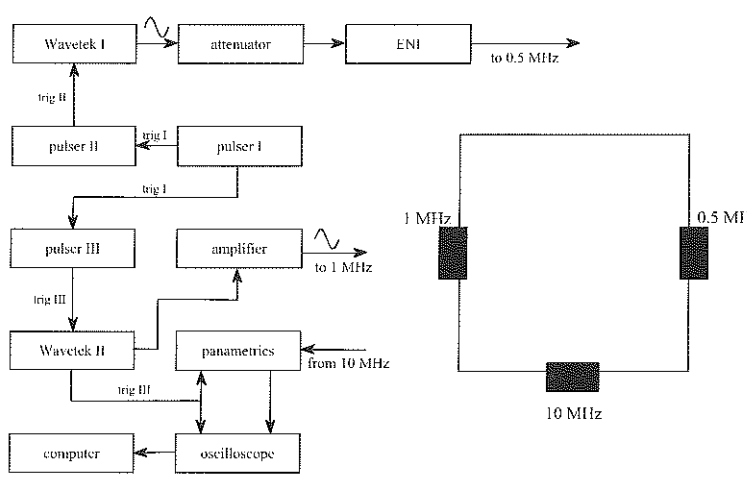


**Figure 3.5** *Schematic setup for measuring the nonlinear response.*

line with the 0.5-MHz transducer. The response of the 1-MHz signal was received by a 10-MHz single-element, broadband transducer (flat response within 3 dB between 1 and 10 MHz) that was mounted perpendicular to the 0.5- and 1-MHz transducers. The average scattered power was calculated over the FFT of 10 time traces as received with the 10-MHz transducer at a repetition rate of 1 Hz. Pulsers I, II and III (PM 5712 and PM 5716, Philips) were used for synchronization. The triggering sequences are shown in figure 3.4B (pulse III was set to 10 $\mu$s).

### Disappearance time

The disappearance time was measured using the setup shown in figure 3.3A. Only the 5 MHz transducer was used in pulse/echo mode. The frequency of Wavetek II was set to 1.6 kHz. Thus, a sequence of low-amplitude pulses (acoustic pressure of 100 kPa) was generated with a pulse-repetition interval (PRI) of 0.6 ms, so as to measure the evolution of the generated free gas bubbles over time. The high amplitude burst (acoustic pressure of 1.6 MPa; 0.5 MHz; 10 cycles) was transmitted immediately after the second low-amplitude pulse. The triggering sequences are shown in figure 3.4C. Again, the Isoton® was air saturated.

## 3.4 Results and discussion

### Enhanced scattering

Figure 3.6A (solid lines) shows the scattered spectrum of a Quantison™ dilution of 1:4500, which corresponds to $3.3\times10^5$ microspheres per ml, when the high-amplitude burst was turned

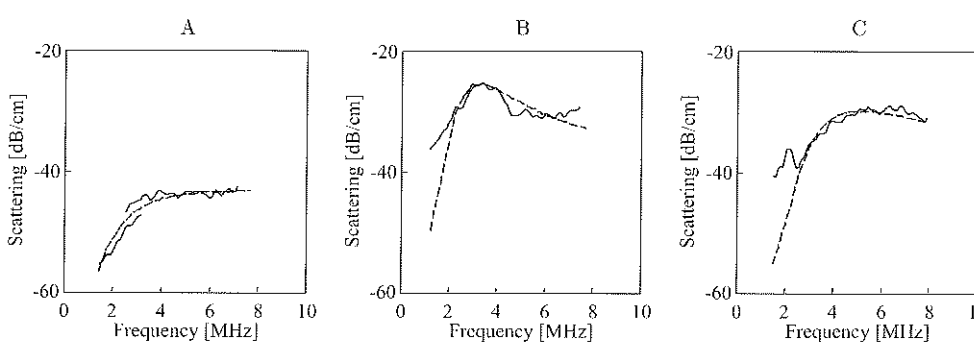


**Figure 3.6** *(A) Scattering vs. frequency of a dilution of 1:4500 of Quantison™ measured without the high-amplitude ultrasound burst. —— = measured spectrum, -----= theoretical spectrum using the size distribution shown in figure 3.7A. (B), —— = measured spectrum 0.6 ms after the transmission of the 0.5-MHz high-amplitude ultrasound burst at the same region. -----= theoretical spectrum using the size distribution shown in figure 3.7B. (C) The same as in (B) but now the 1-MHz transducer was used for generating the high-amplitude burst. —— = measured spectrum; -----= theoretical spectrum using the size distribution shown in figure 3.7C.*

off. This is the typical scattering response of Quantison™ at low acoustic pressure, and is described in detail in chapter 2. The scattering increases as a function of frequency below 4 MHz, and is independent of frequency above 4 MHz with a maximum value of −43 dB/cm. Figures 3.6B and 3.6C (solid lines) show the enhanced scattering, measured at the same region, 0.6 ms after this region was insonified by the high-amplitude burst (at 0.5- and 1-MHz, respectively). An increase in scattering of 10 to 20 dB/cm can be observed, compared to figure 3.6A. Additionally, in figure 3.6B a maximum at 3 MHz, the resonance frequency, which is characteristic for free gas bubbles, can clearly be appreciated. In figure 3.6C, this maximum is shifted and broadened. A possible explanation of this effect is that the 1-MHz transducer generated smaller gas bubbles than the 0.5-MHz transducer. For smaller gas bubbles the resonance frequency increases. Additionally, the damping increases, resulting in a broadening and decrease of the resonance peak.

The dotted line in figure 3.6A shows the scattering of Quantison™ according to the theoretical model (chapter 2). The size distribution of Quantison™, shown in figure 3.7A, as measured with a Coulter Counter™ Multisizer II (Coulter Electronics) was used in the model. The dotted lines in figures 3.6B and 3.6C represent the theoretical spectra of the enhanced scattering induced by the 0.5- and 1-MHz transducers, respectively, and were calculated by means of equation (3.1). Note that in this case the size distribution of the generated gas bubbles is not known *a priori*. Hence, a normal distribution was assumed. The mean and standard deviation of the distributions were estimated by minimizing the absolute difference between measured and simulated spectra. This resulted in a mean and standard deviation of 2.00 ± 0.48 $\mu$m, for the 0.5-MHz transducer (figure 3.7B) and 1.20 ± 0.46 $\mu$m, for the 1-MHz transducer (figure 3.7C). It can be appreciated that with this simple approach, a reasonable agreement between measurements and theory was obtained and, from figure 3.7, that different sizes of free gas bubbles were generated for different frequencies of the high-amplitude burst (smaller bubbles for higher frequencies). Possible explanations are that for different frequencies the gas bubbles

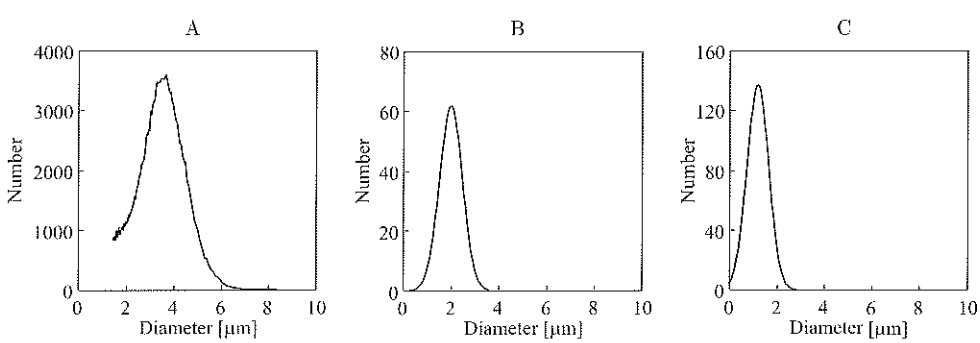


**Figure 3.7** *(A) Size distribution of Quantison™ measured with the Coulter Counter™ Multisizer II with an aperture of 70 $\mu$m employing 256 channels (diameters ranging from 1.45 to 8.33 $\mu$m). (B) Estimated distribution from the measured spectrum in figure 3.6B. (C) Estimated distribution from the measured spectrum in figure 3.6C.*

originate from different parts of the Quantison™ distribution, that different gas bubbles are generated from the Quantison™ bubbles within the same range of the size distribution or that the gas bubbles split into smaller bubbles after release.

Finally, from the theoretical results it can be concluded that the total number of free gas bubbles is about 1% of the total number of the Quantison™ bubbles present in the suspension (notice the different scales of figures 3.7A, 3.7B and 3.7C). This means that only a very small amount of Quantison™ bubbles were actively involved in releasing free gas bubbles.

## Nonlinear response

Figure 3.8A shows the scattered power spectra received by the 10-MHz transducer. The measurements were corrected for the finite aperture[4], the characteristics of the 10-MHz transducer and the electronics. The dotted line represents the spectrum of Quantison™ bubbles (dilution of 1:4500) insonified by the 1-MHz burst without the high-amplitude burst. The spectrum shows no response at higher harmonics of the fundamental frequency. The solid line represents the spectrum measured 0.6 ms after the Quantison™ bubbles were insonified by the high-amplitude burst. Two phenomena can be observed after insonification of the agent with the high-amplitude burst, *viz.*, the spectrum shows an increase at the fundamental frequency of 20 dB and the appearance of higher harmonics of the fundamental frequency. The second harmonic is less than 6 dB below the fundamental frequency. Imaging modalities that rely on the nonlinear response of ultrasound contrast agents will therefore result in increased sensitivity.

Figure 3.8B shows the theoretical power spectrum of the generated free gas bubbles using equation (3.1). Since the frequency of the high-amplitude burst was 0.5 MHz, it was assumed that the generated gas bubbles had the size distribution shown in figure 3.7B. The 1-MHz burst was recorded and used as an input to the model. The magnitude was adjusted to 100 kPa.

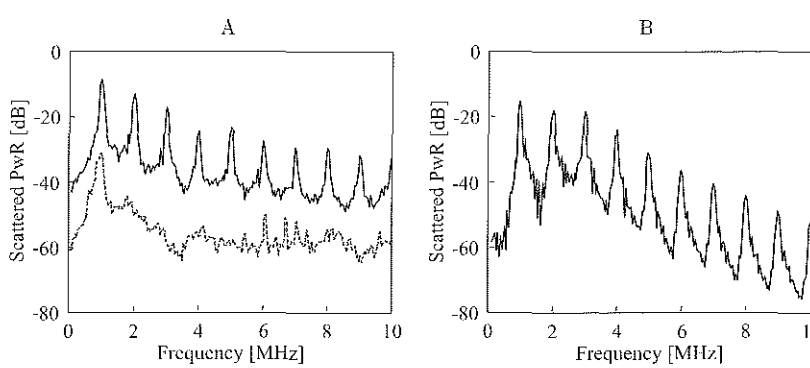


**Figure 3.8** *(A)Received scattered power of Quantison™ by a 10-MHz single element transducer (corrected for transducer characteristics). The signal was generated by a 1-MHz transducer (acoustic pressure of 100 kPa; 10 cycles), without the high amplitude burst (-----) and 0.6 ms after the high-amplitude burst (——). (B) Theoretical power spectrum using equation (3.1) and the size distribution of figure 3.7B. The acoustic pressure was 100 kPa and the actual transmitted burst was used as input signal.*

## Disappearance time

Figure 3.9 shows the backscattered signal from the released air bubbles recorded at intervals of 0.6 ms. The decreasing amplitude is ascribed to the gradual shrinkage and eventual disolution of the bubbles. The persistence of the air bubbles was measured over time and is shown in figure 3.9A. This figure represents a sequential recording of 62 traces covering a total acquisition time of 37 ms. The high-amplitude burst was transmitted immediately after the second low-amplitude pulse. This can be appreciated from figure 3.9A by the fact that the amplitude abruptly increases after two pulses. The scattering amplitude decreases as a function of time, representing the slow diffusion of the released gas into the surrounding liquid. This is depicted in detail by figure 3.9B at three time points, *viz.*, 0, 15 and 30 ms after transmitting the high-amplitude burst (see corresponding locations in figure 3.9A). After 30 ms, the increase in scattering amplitude has completely disappeared.

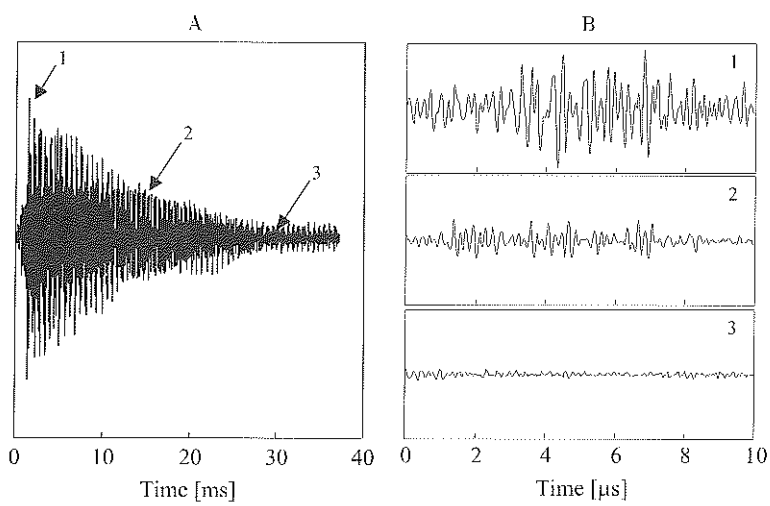


**Figure 3.9** *The release and disappearance of air bubbles from Quantison™. (A) Sequence representation of pulse echo response from successive survey pulses (100 kPa; 5 MHz; 0.6 ms interval). Scattering of Quantison™ up to 1.2 ms. The high-amplitude burst (1.6 MPa; 0.5 MHz; 10 cycles) was applied at 1.2 ms. (B) The enhanced scattering decays over time. Top panel: immediately after transmission of the high-amplitude burst; middle panel: after 15 ms; bottom panel: after 30 ms, corresponding to the locations marked in (A) by 1, 2 and 3, respectively.*

Figures 3.10A and 3.10B (solid lines) show the energy as a function of time, within each time trace, for the gas bubbles generated by the 0.5- and 1-MHz transducers, respectively. The disappearance time, $t_d$, was estimated from the 95% decay point in these figures. The mean value and standard deviation of a set of ten sequence recordings was 28.8 ± 2.4 ms for the 0.5-MHz transducer, and 16.3 ± 2.3 ms for the 1-MHz transducer. The theoretical disappearance curves were calculated by using the size distributions of figures 3.7B and 3.7C as

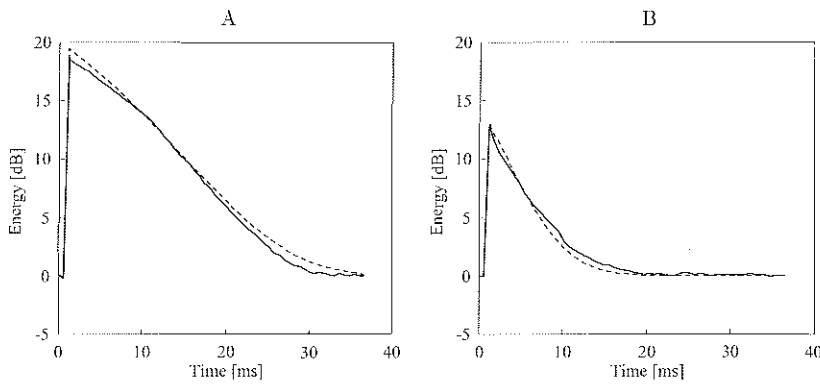


**Figure 3.10** *The energy as calculated from the scattering response of the generated free gas bubbles with the 0.5-MHz transducer, (A), and with the 1-MHz transducer, (B).* ——*= measurement;* -----*= theory.*

the starting distributions. Every 0.6 ms, the size distributions were recalculated by means of equation (3.4), and the scatter spectra were calculated at the corresponding time points using equation (3.1). The spectra include the scattering of the Quantison™ bubbles (dilution of 1:4500). Figures 3.10A and 3.10B (dotted lines) show the energy as a function of time as determined from the calculated spectra for the 0.5- and 1-MHz transducer, respectively. The energy was calculated by integrating the scattering over a frequency band ranging from 2–8 MHz. Also, the disappearance time was measured for gas bubbles generated at different frequencies of the high-amplitude burst (at a fixed amplitude of 1.6 MPa and a fixed number of cycles). The results are listed in table 3.1 and show a decrease in disappearance time for increasing frequencies. The corresponding bubble diameters were calculated by means of equation (3.4).

**Table 3.1** *Disappearance time of generated free air bubbles from Quantison™ as a function of frequency in saturated Isoton® under standard conditions (mean ± STD). The second row shows the corresponding bubble diameters as calculated by means of equation (3.4).*

| Frequency [MHz] | 0.5 | 1 | 2 | 5 |
|---|---|---|---|---|
| $t_d$ [ms] | 28.8 ± 2.4 | 16.3 ± 2.0 | 11.6 ± 2.2 | 5.1 ± 2.1 |
| Diameter [$\mu$m] | 2.8 | 2.3 | 2.0 | 1.4 |

## Final remarks

As was stated before, the effect described in this chapter is transient. In figure 3.11 the change of the acoustical properties, *viz.*, transmission and scattering are shown. This figure shows the transmission and scattering spectra of a dilution of 1:250 of Quantison™. This concentration was chosen to induce a clear minimum in transmission of −3 dB/cm at 4 MHz. The spectra

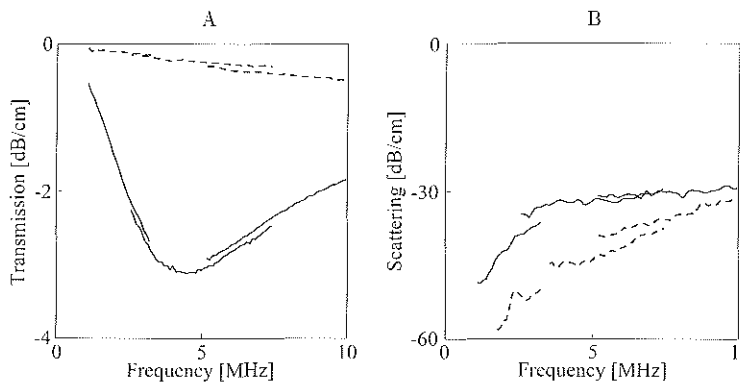


**Figure 3.11** *Transmission (A) and scattering (B) versus frequency for Quantison™. Before (——) and after (-----) Quantison™ had been put under an ultrasound machine and exposed to high acoustic pressure waves (MI=1.1) for 15 min. The dilution was 1:250.*

were measured before and after a continuous insonation for 15-min with a commercial diagnostic scanner at the highest power setting (MI of 1.1 at 2.5 MHz), and are shown in figure 3.11 by the solid and dotted lines, respectively. The Quantison™ was continuously stirred. It can be appreciated from figure 3.11A that the minimum of the transmission spectrum at 4 MHz has completely disappeared from within this frequency range, after the Quantison™ was exposed to high power insonification. A minimum in transmission as shown in figure 3.11A is a typical characteristic for free or encapsulated gas bubbles. For the scattering, figure 3.11B, the difference is really apparent for frequencies below 10 MHz. An explanation is that, at these particular settings of the ultrasound machine, only the larger bubbles were destroyed.

The bubbles were not completely destroyed after insonification by the high-amplitude burst. Figures 3.12A and 3.12B are microscopic images of Quantison™ before and after high power sonification, respectively. Before exposure, the microspheres appear to be darker than after exposure (see arrows in figure 3.12B). This may be an indication that the encapsulated air was replaced by the surrounding liquid. Also, liquid-filled bubbles are less compressible than gas-filled bubbles and, therefore, are ineffective scatterers. Thus, the bubbles became "transparent", both optically and acoustically. Note, however, that figures 3.12A and 3.12B do not show the same particles but are just particles of a sample before, and other particles of the same sample after insonification.

The results in table 3.1 show a decrease in calculated bubble size as a function of the applied frequency of the high-amplitude burst. This implies that particular bubble sizes can be selectively released. Also, the simulations indicate that only about 1% of all the bubbles present were ruptured by the high acoustic amplitude burst. A possible explanation is that the shell of some of the encapsulated gas bubbles possess weak spots that are easily ruptured. This means that the release of free gas bubbles from encapsulated gas bubbles can be optimized by machine settings and available bubble sizes, and tuned for specific purposes. For example, the

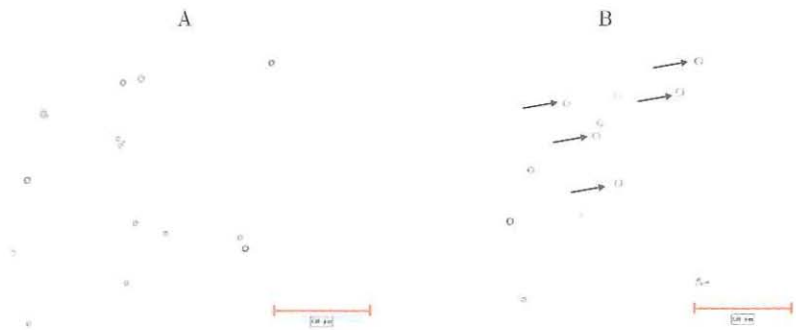


**Figure 3.12** *Microscopic photograph of Quantison™ diluted in Isoton® at a magnification of 200×. (A) before and (B) after Quantison™ was put under an ultrasound machine and exposed to high acoustic pressure waves for 15 minutes. The arrows indicate fluid-filled microspheres.*

presence of free gas bubbles can be used for purposes other than imaging, such as non-invasive assessment of gas concentration, temperature or ambient pressure (chapter 7). These potential applications are supported by the fact that the disappearance time of gas bubbles depends on the dissolved gas concentration, temperature and ambient pressure. Also, other gases like perfluor gases, which have lower diffusion and Ostwald coefficients, may be used. This results in longer disappearance times, so that the released gas bubbles can be used for a longer period of time.

Finally, pharmacological applications may be possible. Certain drugs can be incorporated into the shell or attached to its surface. Using ultrasound at high acoustic peak pressures, these drugs may be released from their microspheric carrier at specific locations within the human body (chapter 8). This means that drug treatment can be locally delivered, resulting in a lower systemic drug level.

## 3.5 Conclusions

In this chapter, a three-way demonstration is provided, that the enhanced transient scattering observed when encapsulated gas bubbles are exposed to ultrasound pulses of high-peak pressures exceeding a threshold can be explained by the release of free gas bubbles. Encapsulated gas bubbles are robust and last in the circulation but their scatter efficiency and nonlinear response are suboptimal. The scatter efficiency and nonlinear response of free gas bubbles, however, are far superior but their life span is limited to milliseconds. Therefore, ultrasound in combination with this "dualistic" character suggests that encapsulated gas bubbles can be construed as a robust vehicle for localized delivery of free gas bubbles, the ultimate ultrasound contrast agent.

# References


1. B. Schrope, V. L. Newhouse, and V. Uhlendorf, "Simulated capillary blood flow measurements using a nonlinear ultrasonic contrast agent," *Ultrasonic Imaging*, vol. 14, no. 2, 1992.

2. P. N. Burns, J. E. Powers, and T. Fritzsch, "Harmonic imaging: A new imaging and doppler method for contrast enhanced ultrasound," *Radiology*, vol. 185 (P), p. 142, 1992.

3. D. L. Miller, "Ultrasonic detection of resonant cavitation bubbles in a flow tube by their second-harmonic emissions," *Ultrasonics*, pp. 217 224, 1981.

4. N. de Jong and L. Hoff, "Ultrasound scattering properties of Albunex® microspheres," *Ultrasonics*, vol. 31, no. 3, pp. 175–181, 1993.

5. C. C. Church, "The effect of an elastic solid surface layer on the radial pulsations of gas bubbles," *J Acoust Soc Am*, vol. 97, no. 3, pp. 1510–1521, 1995.

6. N. de Jong, R. Cornet, and C. T. Lancée, "Higher harmonics of vibrating gas filled microspheres. Part one: Simulations," *Ultrasonics*, vol. 32, pp. 447–453, 1994.

7. V. Uhlendorf and C. Hoffmann, "Nonlinear acoustical response of coated microbubbles in diagnostic ultrasound," in *IEEE Ultrason Symp*, vol. 3, (Cannes, France), pp. 1559 1562, 1994.

8. N. de Jong, P. J. A. Frinking, F. J. ten Cate, and P. van der Wouw, "Characteristics of contrast agents and 2D imaging," in *IEEE Ultrason Symp*, vol. 2, (San Antonio, USA), pp. 1449–1458, 1996.

9. F. Moriyasu and Y. Kono, "Flash echo imaging of liver disease," in *The leading edge in diagnostic ultrasound*, (Atlantic City, USA), 1998.

10. Y. Takeuchi, "Industrial use of thermoplastic micro-balloon to mimic the contrast agents and its *in vitro* behaviour including increased gas dynamics," in *IEEE Ultrason Symp*, vol. 2, (Toronto, Canada), pp. 1579–1582, 1997.

11. T. R. Porter and F. Xie, "Transient myocardial contrast after initial exposure to diagnostic ultrasound pressures with minute doses of intravenously injected microbubbles. Demonstration and potential mechanisms," *Circulation*, vol. 92, no. 9, pp. 2391–2395, 1995.

12. H. Medwin, "Counting bubbles acoustically: A review," *Ultrasonics*, no. 1, pp. 7–13, 1977.

13. P. S. Epstein and M. S. Plesset, "On the stability of gas bubbles in liquid-gas solutions," *J Chemical Physics*, vol. 18, no. 11, pp. 1505–1509, 1950.

14. A. Kabalnov, D. Klein, T. Pelura, E. Schutt, and J. Weers, "Dissolution of multicomponent microbubbles in the bloodstream. 1: Theory," *Ultras Med Biol*, vol. 24, no. 5, pp. 739–49, 1998.

# CHAPTER 4

# Release burst imaging of ultrasound contrast agents


## Abstract

*A novel ultrasound contrast imaging technique is described that optimally employs the rupture of the contrast agent. It is based on a combination of multiple high frequency, broadband, detection pulses and a separate release burst. The detection pulses are used to survey the target before and after the rupture of the contrast agent. In this way, both processes (imaging and release) can be optimized separately. The presence of the contrast agent is simply detected by correlating or subtracting the signal responses of the detection pulses. Because the time delay between the detection pulses can be very short, the subtraction is less affected by tissue motion and can be performed in real time. In vitro measurements showed that by using a release burst, the detection sensitivity increased 12 to 43 dB for different types of contrast agents. In the presence of a moving phantom, the increase in sensitivity was 22 dB. This new method is very sensitive for contrast agent detection in fundamental imaging mode and, therefore, nonlinear propagation effects do not limit the maximum obtainable sensitivity for contrast agent detection. However, due to the inherent disruption of the contrast agent, the method has to operate in an intermittent way.*



Based on the publication: "A novel ultrasound contrast imaging approach based on the combination of multiple imaging pulses and a separate release burst" by Peter J.A. Frinking, E. Ignacio Céspedes, Johan Kirkhorn, Hans Torp and Nico de Jong. Accepted for publication in: *IEEE Transactions on Ultrasonics, Ferroelectrics and Frequency Control, 1999.*

## 4.1 Introduction

The utilization of ultrasound contrast agents, to extend the capabilities of ultrasound imaging, has resulted in the development of a variety of auxiliary methods of operation. These methods exploit specific acoustic signatures of contrast agents, and are designed to improve the sensitivity of ultrasound imaging systems for contrast agent detection in the presence of tissue, which can be defined as agent-to-tissue ratio. Harmonic-contrast imaging[1], for example, exploits the highly nonlinear scattering behavior of gas bubbles, which is not shown by tissue. Although conventional harmonic-contrast imaging offers limited success in perfusion imaging applications, its combination with Doppler techniques (e.g. color Doppler, power Doppler) is one of the most sensitive imaging modes currently available in terms of agent-to-tissue ratio.

There is, however, a tradeoff between the detectability of ultrasound contrast agents and imaging resolution[2]. The limited bandwidth of current transducers force the bandwidth of the transmitted wave to be narrow to minimize the spectral overlap between the fundamental and second harmonic parts of the received spectrum. Additionally, for high bandwidth imaging pulses, which are preferable for high resolution imaging, the harmonic and Doppler spectra will broaden and, therefore, the precision for detecting the contrast agent will decrease. New techniques like pulse inversion and pulse inversion Doppler[3] largely overcome the contrast detection-resolution tradeoff. However, nonlinear propagation continues to limit the performance of harmonic-contrast and pulse inversion methods. Although minimized by applying adjusted Doppler filters for agent and tissue properties[4], the maximum obtainable sensitivity to detect contrast is limited.

In chapter 3, it has been shown that encapsulated types of contrast agents possess a "dualistic" scattering character, with a particular behavior occurring at acoustic pressures above a threshold. At these acoustic pressures, the scattering increases dramatically due to the nonlinear behavior of the contrast agents, e.g. Quantison™ (Quadrant Ltd., Nottingham, UK) and Sonovist® (Schering AG, Berlin, Germany). This is explained by the fact that free gas bubbles are released as the encapsulating shells are ruptured by a high power ultrasound burst. The result is a transient enhancement of the scattering, where the duration of the effect is related to the persistence of the free gas bubbles in the medium. With small variations, this particular signature has been addressed by several names for the different types of contrast agents; acoustically stimulated acoustic emission (ASAE)[5], power-enhanced scattering (PES)[6] , scintillation sonography[7], flash-echo imaging[8], etc.

In conventional B-mode imaging, the enhanced scattering may be visualized as bright echogenic areas (figure 3.1). Although the increase in echogenicity is substantial, in hyperechoic regions or very small vessels where the number of bubbles is low, e.g. the myocardium, echoes from surrounding tissue can easily mask this increased echogenicity. As an example, figure 4.1 depicts the backscatter coefficient spectra for blood[9], normal myocardium[10,11] and of a tissue-mimicking phantom used in this study. Figure 4.1 also shows the backscatter coefficient of intact Quantison™ (chapter 2), and of Quantison™ immediately after applying a high power ultrasound burst (chapter 3). The latter two represent the backscatter coefficient of the encapsulated gas bubbles and the released free gas bubbles, respectively. This figure illustrates that for the concentration used ($3.3\times10^5$ microspheres per ml), there is a 10–20 dB increase in the scattering for the free gas bubbles. However, it still is 5–10 dB below the scattering level

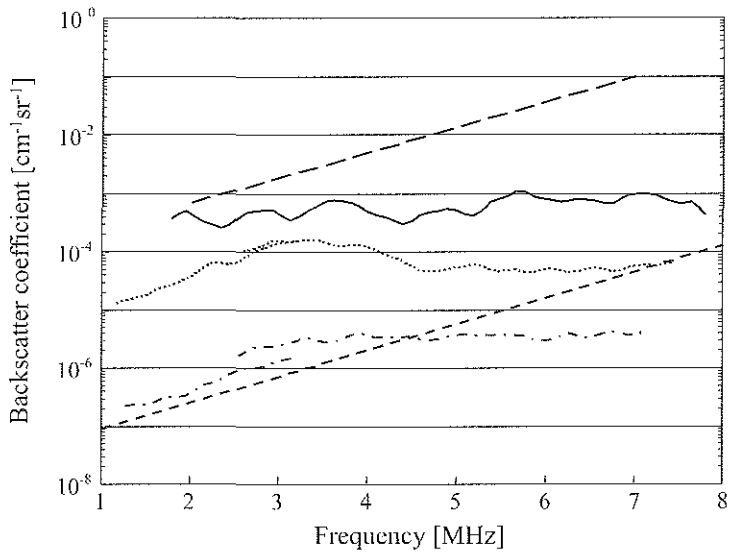


**Figure 4.1** *Backscatter coefficient for blood (-----), normal myocardium (——), tissue-mimicking phantom (——) and Quantison™ at a concentration of 1:4500 ($3.3\times10^5$ microspheres per ml) before (·····) and immediately after (· · · · ·) a high-power ultrasound burst.*

of the phantom and normal myocardial tissue. Consequently, imaging strategies based on the analysis of amplitude will still result in a low agent-to-tissue ratio.

With the current imaging techniques, gas release (contrast agent disruption) and imaging are achieved during the early part and late part of a relatively long (several cycles) transmitted burst, respectively. However, it has been reported that, for a fixed amplitude and a given number of cycles per burst, the process of releasing gas bubbles is more efficient at lower frequencies[5]. Moreover, the release also improves with more cycles in the acoustic burst for a fixed amplitude and frequency[5]. Thus, while it is well known that the imaging resolution improves for short, high frequency pulses, the process of free gas bubble release is most effective for long, low frequency bursts.

In this chapter, a new contrast imaging technique is proposed that resolves this situation by separating the imaging and release processes. Imaging, or detection pulses, are used to survey a target before and after the release of free gas bubbles from the contrast agent. Both processes, imaging (detection) and release (disruption), can be optimized separately and, therefore, this method circumvents the need to sacrifice either contrast sensitivity or imaging resolution. By comparing the scattering responses of broadband detection pulses before and after the release of free gas bubbles, high-resolution contrast imaging can be achieved with a high sensitivity for contrast agent detection.

## 4.2 Theory

The ability of a single ultrasound pulse to disrupt or modify an ultrasound contrast agent increases for high acoustic amplitudes, long pulse lengths and low frequencies. These three parameters are all present in the expression of the acoustic energy:

$$E_{acoustic} = \int_0^K (P_0 sin(2\pi f t))^2 dt = K \cdot P_0^2 \frac{1}{f} \approx K \cdot (MI)^2, \tag{4.1}$$

where

$P_0$ = acoustic pressure amplitude
$f$ = frequency
$t$ = time
$K$ = number of cycles per burst.

The mechanical index (MI) is defined by[12]:

$$MI = \frac{P_-}{\sqrt{f}}, \tag{4.2}$$

with the peak negative acoustic pressure ($P_-$) in MPa, and the frequency in MHz. Increased disruption efficiency at low frequencies can be explained by increased MI and energy. For an imaging situation where the MI is limited, because of attenuation or safety regulations, the pulse length, $K$, is the only parameter that can be used to increase the disruption efficiency. However, imaging resolution improves for short, high frequency pulses. Therefore, by separating imaging and contrast agent disruption both processes can be optimized independently.

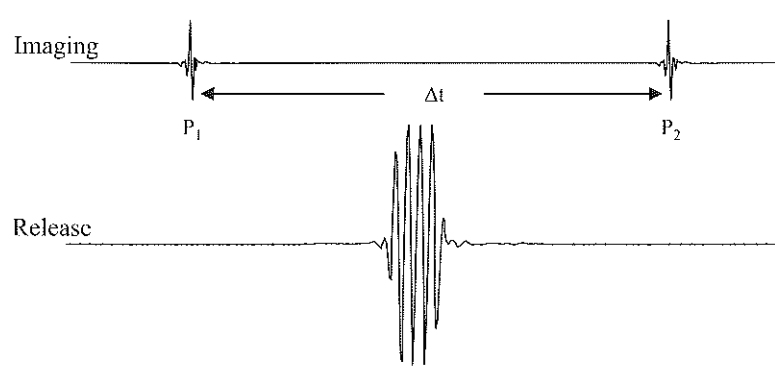


**Figure 4.2** *A typical 'multiple detection pulses release burst' sequence. Top: two low amplitude, broadband 'imaging' pulses ($P_1$ and $P_2$) are separated by a time delay of $\Delta t$. Bottom: A high amplitude, narrow band (several cycles long) 'release' burst is transmitted in between the two detection pulses. (Note that the amplitudes are not plotted on a relative scale).*

## Ultrasound contrast agent detection

Multiple detection pulses ($P_1$ and $P_2$, top of figure 4.2) are used to survey a target before and after the disruption of contrast agent by a high-power ultrasound burst, the so-called release burst (figure 4.2, bottom). The pulse-to-pulse change in the received echo signals is caused by the modification of the contrast agent or release of free gas bubbles, which exclusively occurs in areas occupied by contrast agent. The received radio frequency (RF) signals, $x(t)$, are demodulated to their baseband in-phase and quadrature (IQ) components by mixing them with two sinusoid signals, 90 degrees out of phase (figure 4.3). The demodulation frequency is $f_d$, and generally is chosen equal to the transmit frequency. Subsequently, the I and Q components are low-pass filtered and decimated, thus achieving a lower sampling frequency. In this way, phase and amplitude changes can be obtained accurately at lower sampling frequencies than by using the raw RF signals. A contrast specific signal can be obtained by temporal correlation or simple subtraction of the received RF signals before and after the release burst.

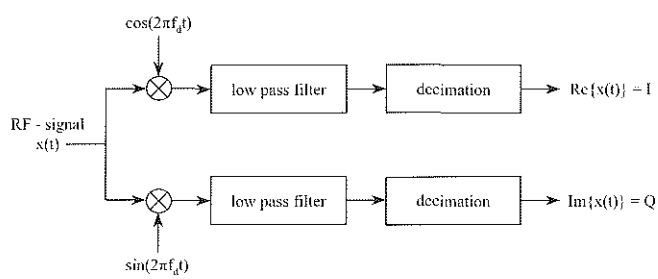


**Figure 4.3** *Baseband demodulation scheme including low-pass filtering and decimation.*

### Correlation approach

Temporal correlation analysis is performed on short, sliding, overlapping windows of the received baseband demodulated RF signals. The (normalized) correlation profile along the beam is given by:

$$\rho_{1,2}[n] = \frac{\sum_{k=1+(n-1)\Delta}^{L_o+n\Delta} \left(S_1[k]-\bar{S}_{1n}\right)\cdot\left(S_2[k]-\bar{S}_{2n}\right)^*}{\sqrt{\sum_{k=1+(n-1)\Delta}^{L_o+n\Delta} \left(S_1[k]-\bar{S}_{1n}\right)^2 \cdot \sum_{k=1+(n-1)\Delta}^{L_o+n\Delta} \left(S_2[k]-\bar{S}_{2n}\right)^2}};$$

$$n = 1 \cdots\cdots \frac{N-L_w}{\Delta} + 1, \tag{4.3}$$

where

$S_1[k]$ = demodulated RF signal before the release burst
$S_2[k]$ = demodulated RF signal after the release burst

$k$ = sample number along the beam
$n$ = window number
$N$ = total number of range samples (depth)
$L_w$ = number of range samples per window
$\bar{S}_{1n}$ = mean of $S_1$ for window n
$\bar{S}_{2n}$ = mean of $S_2$ for window n.

$$\Delta = L_w - L_o, \tag{4.4}$$

with

$L_o$ = number of overlapping range samples ($L_o < L_w$).

In case of no release burst (and assuming that there is no decorrelation), $S_1$ and $S_2$ will be similar and, consequently, $|\rho_{1,2}|$ approaches 1. On the other hand, when a release burst is used, $S_1$ and $S_2$ will be different in regions containing contrast agent due to the additional response of the released gas bubbles, and $|\rho_{1,2}|$ will approach 0, depending on the amount of released gas bubbles.

### Subtraction approach

As an alternative to correlation, in many cases the sum-absolute-difference (SAD) can be used instead of the normalized correlation coefficient[13]. The SAD method does not require multiplication nor the calculation of mean signal values, like with correlation, and thus may be faster and easier to implement. Although the SAD method is not similar to the correlation method, it is known that a minimum of SAD occurs simultaneously at maximum correlation[14]. The SAD profile along the beam direction is given by:

$$SAD_{1,2}[n] = \sum_{k=1+(n-1)\Delta}^{L_o+n\Delta} |S_1[k] - S_2[k]|; \quad n = 1 \cdots \frac{N - L_w}{\Delta} + 1, \tag{4.5}$$

where $SAD_{1,2}[n]$ is the non-normalized sum absolute difference of the windowed baseband responses $S_1$ and $S_2$.

When the window size $L_w = 1$ and $L_o = 0$, equation (4.5) simplifies to simple subtraction of the two baseband responses:

$$\delta_{1,2} = |S_1 - S_2|, \tag{4.6}$$

where $\delta_{1,2}$ is the absolute value of the difference between responses $S_1$ and $S_2$ along the beam, and will be defined as the difference profile. This is an approach used in radar and in ultrasound color flow imaging, to isolate echoes from moving structures from relatively stationary echoes, and is called the moving target indicator (MTI) technique[15,16]. Hence, when there is no motion, the background signal (clutter) is simply removed and the difference profile indicates the sensitivity to detect the contrast agent in the presence of (stationary) tissue, *i.e.*, it is a measure of the agent-to-tissue ratio.

## 4.3 Materials and methods

To evaluate the proposed imaging method, experiments were performed with single-element and phased array transducers to transmit the detection pulses. The set-up for the single element transducer was used as a fundamental test of the method. The phased array transducer was used to investigate the feasibility of implementing the method in a commercial diagnostic ultrasound scanner. For both experiments, a separate single element transducer was used to generate the release burst.

### Single element transducer

The experimental setup is illustrated in figure 4.4. A circular 2-MHz single-element transducer (Panametrics, Waltham, USA) focused at 75 mm, with an aperture of 25 mm, was mounted in a water tank. A gated sine wave burst (4 cycles) was generated by an arbitrary wave-

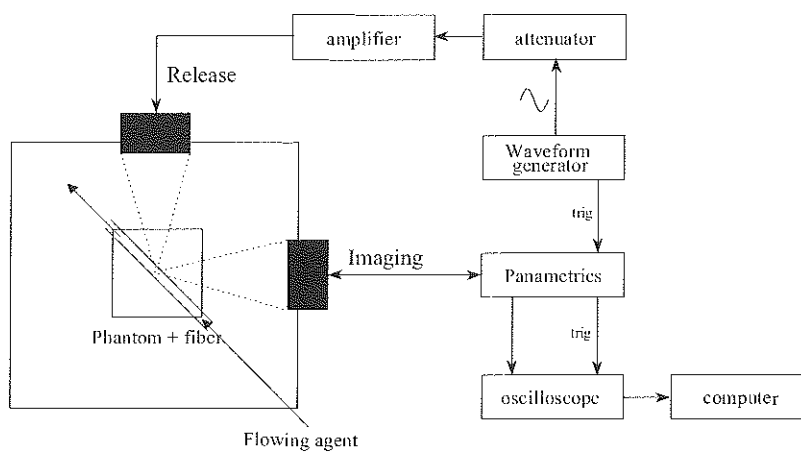


**Figure 4.4** *Setup for single element experiments.*

form generator (LW 420A, LeCroy, Chestnut Ridge, USA) and amplified by a 60 dB linear power amplifier (A-500, ENI, Rochester, USA). The amplitude was adjusted by a separate variable attenuator (355C/D, HP, Palo Alto, USA) to a peak-negative pressure, $P_- = 2$ MPa. This signal was directed to the 2-MHz transducer, and was used as release burst. A circular 5-MHz (Panametrics) broadband, single-element transducer was mounted perpendicularly to the 2-MHz transducer. This transducer was focused at 75 mm and had an aperture of 18 mm. Short, pulses (fractional bandwidth of 90% at the $-6$ dB level) were generated, before and immediately after the release burst, and received by a pulser/receiver (5052 PR, Panametrics). The peak-negative pressure was 200 kPa. The received signals were amplified 40 dB and digitized by a LeCroy 9400A (LeCroy) digital oscilloscope (100 MHz, 8 bits). The signals were

recorded over a time window of 10 $\mu$s and transferred via an IEEE 488 interface to a standard personal computer. All processing and visualization were performed off-line using Matlab® (The Mathworks Inc., Natick, USA).

## Phased array transducer

Experiments were performed with a 3.5 MHz phased array transducer of a System Five (GE Vingmed Ultrasound, Horten, Norway) ultrasound scanner (A in figure 4.5). The transmitted detection pulses had a center frequency of 3.3 MHz with a fractional bandwidth of 60% at −6 dB, and a mechanical index (MI), as displayed on the ultrasound scanner, of 0.4 and 1.2. The corresponding measured peak-to-peak pressures values, as measured with a calibrated hydrophone (PVDFZ44-0400, Specialty Engineering Associates, Soquel, CA, USA) were 0.6 and 1.5 MPa, respectively. A circular, 0.5-MHz (Panametrics) single-element transducer (B in figure 4.5) was mounted perpendicularly to the phased array transducer, and generated the release burst (10 cycles, $P_-$ of 0.6 MPa). This transducer was focused at 75 mm and had an aperture of 37 mm. 16 detection pulses were fired in one direction with a pulse repetition frequency (PRF) of 4 kHz. The release burst was synchronized to the eighth imaging pulse, giving a RF-dataset with 7 pulses before and 8 pulses after the release burst. Only the responses of pulses 7 and 9 were used.

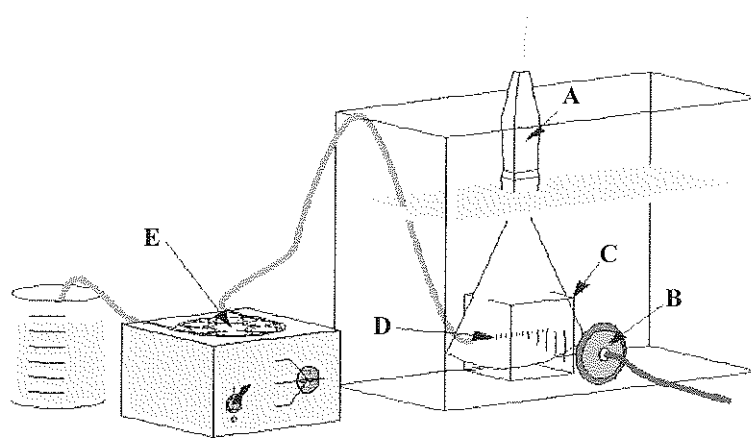


**Figure 4.5** *Setup for phased array experiments. (A) phased array transducer connected to the System Five for generating the detection pulses, (B) 0.5 MHz single element transducer which transmits the release burst, (C) tissue-mimicking phantom made from agar mixed with carborundum scattering particles, (D) synthetic capillary fiber with inner diameter of approximately 180 $\mu$m which is continuously flushed with diluted contrast agent using a roller pump (E).*

## Tissue motion

In practical diagnostic ultrasound, patient breathing and cardiac pulsation induce tissue motion. Due to tissue motion, successive echo signals from one direction can change considerably, which can be interpreted as bubble disruption. Therefore, we set up an experiment to grade the effect of tissue motion on the sensitivity to detect the contrast agent.

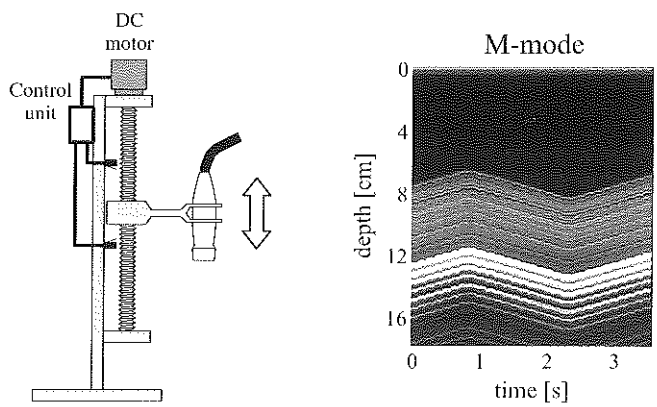


**Figure 4.6** *Left: device used to simulate 'tissue motion'. Right: M-mode recording showing the alternating up and down motion of the transducer with a peak velocity of approximately 1.5 cm/s.*

A custom made device (figure 4.6, left) was used to move the transducer of the System Five ultrasound system relative to the phantom to simulate tissue motion. The device consisted of a DC motor connected to a screw shaft moving a sliding probe holder. Two adjustable switches were mounted on the device, and a control unit changed the motor rotation direction every time one of the switches was hit by the slide. This way, the device produced an alternating up and down 'tissue motion' with a peak velocity of approximately 1.5 cm/s. Figure 4.6, right, shows a M-mode recording indicating the up and down movement of the transducer. The straight lines indicates that the transducer was moving more or less linearly. Note the 'wiggles' in the M-mode, which were caused by lateral motion of the transducer due to a slight eccentric rotation of the screw shaft.

## Phantom setup

Flow phantoms were constructed to emulate small blood vessels in tissue. A PTFE tubing (Zeus, Orangeburg, USA) with an inner diameter of 1 mm (figure 4.4), and a synthetic Cuprophan® capillary fiber (Akzo Nobel Faser AG, Germany) with an inner diameter of 180 $\mu$m (figure 4.4 and D in figure 4.5) were used as vessels. The vessels were embedded in agar blocks of 6×5×5 cm (C in figure 4.5). The agar (Agar powder CMN, Boom BV, Meppel, The Netherlands) was mixed with small carborundum particles (particle sizes ranging from 5 8 $\mu$m) to mimic high echogenic surrounding material (2% Agar with 2% carborundum). The backscatter

coefficient of the phantom is shown in figure 4.1 (solid line). A flow setup (E in figure 4.5) was constructed by connecting the vessels to a flow unit driven by a peristaltic pump (Varioperpex® 12000, LKB Bromma, Sweden) using 25 Gauge needles. A flow rate of 0.1 cc/min was used, which corresponds to an average velocity of approximately 0.2 and 5 cm/s for the 1-mm vessel and 200-$\mu$m vessel, respectively.

The transducers were aligned with the vessels by looking at the reflection of air, which was initially flushed through the vessels. For the experiment with the single element transducer, the phantom was positioned such that the vessel was located at the focus of the release and imaging transducers, *i.e.*, 75 mm from both transducers. For the experiment with the phased array transducer, the location of the vessel was 95 mm from the surface of the phased array transducer, and in the focus of the release transducer.

### Contrast agents

Three different types of contrast agents in solution were used. Quantison™ consists of air bubbles encapsulated by a relatively thick (200–300 nm) and rigid shell of human albumin. Levovist® (Schering AG, Berlin, Germany) consists of air pockets trapped in galactose sugar stabilized by palmitic acid, which after suspension behave almost identical to free air bubbles. SonoVue™ (Bracco Research S.A., Geneva, Switzerland) consists of sulfur hexafluoride gas bubbles encapsulated by a flexible phospholipid shell. All three agents have a mean bubble diameter close to 3 $\mu$m.

## 4.4 Results

### Single element transducer

Figure 4.7 shows a step-by-step representation of the proposed imaging approach with the 1-mm vessel filled with Quantison™. $R_1$ and $R_2$ (top of figure 4.7) represent the received RF signals of the two detection pulses $P_1$ and $P_2$ (figure 4.2), respectively. The absolute value of the correlation coefficient, $|\rho|$, was calculated by means of equation (4.3), for a window length of 0.5 mm and 30% window overlap. The correlation profile was constructed along the acoustical beam, *i.e.*, versus depth (middle of figure 4.7). A threshold value $|\rho|_{th}$, below which the area was recognized as a contrast rich area, was defined (in this example an empirical value of $|\rho|_{th} = 0.8$ was defined). Finally, (bottom of figure 4.7), the areas where $|\rho| < |\rho|_{th}$ were color coded and super imposed on the original B-mode image.

As an example of the SAD method, the same data used in the previous section was processed according to equation (4.5) with the same window length and overlap. The SAD profile vs. depth is expressed in dB and shown in figure 4.8A. The peak in the SAD profile indicates the presence of contrast due to its pulse-to-pulse variation compared to the surrounding phantom material. Since the SAD is not normalized, a reference value was calculated by averaging the response of the phantom over a 2-mm section next to the vessel. In this way, the sensitivity or agent-to-tissue ratio could be calculated by subtracting the reference value from the peak value, which in this particular example was 26.8 dB. The difference profile vs. depth, as calculated by

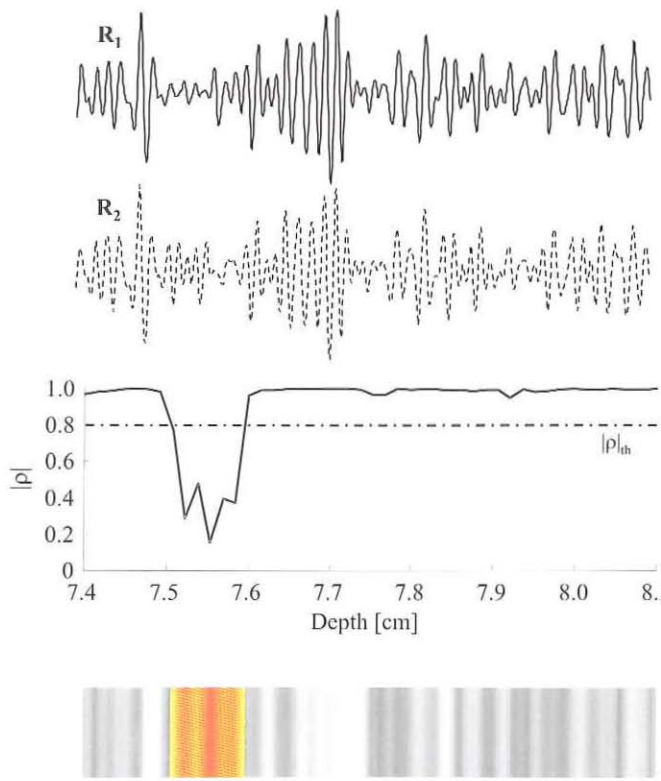


**Figure 4.7** *Schematic representation of the detection process for the 1-mm vessel filled with Quantison™. Top: Response of the two successive detection pulses (RF traces). Middle: Regions of high or low correlation can be detected along the beam by gated correlation analysis. A threshold of 80% correlation was used to detect the presence of released air bubbles. Bottom: Grey scale and color representation of phantom, based on high and low correlation regions, respectively.*

means of equation (4.6), is shown in figure 4.8B. Although the agent-to-tissue ratio increased to 29.1 dB, the vessel was clearly depicted in both methods.

In conventional B-mode imaging the detection of contrast agents is based on an enhancement of the brightness of grey-scale images. However, in hyperechoic regions or very small vessels where the concentration of contrast is low, echoes from surrounding tissue can easily mask this enhancement. For the myocardium, for example, the ratio of the blood volume containing the contrast agent and tissue is less than 10% and, consequently, the enhancement will only be several dB. Therefore, B-mode imaging results in poor contrast agent detectability in the presence of tissue. This is illustrated in figure 4.9 (top), where A-mode lines of the phantom with the 200-$\mu$m vessel and Quantison™ are shown. Three different situations are shown, *viz.*,

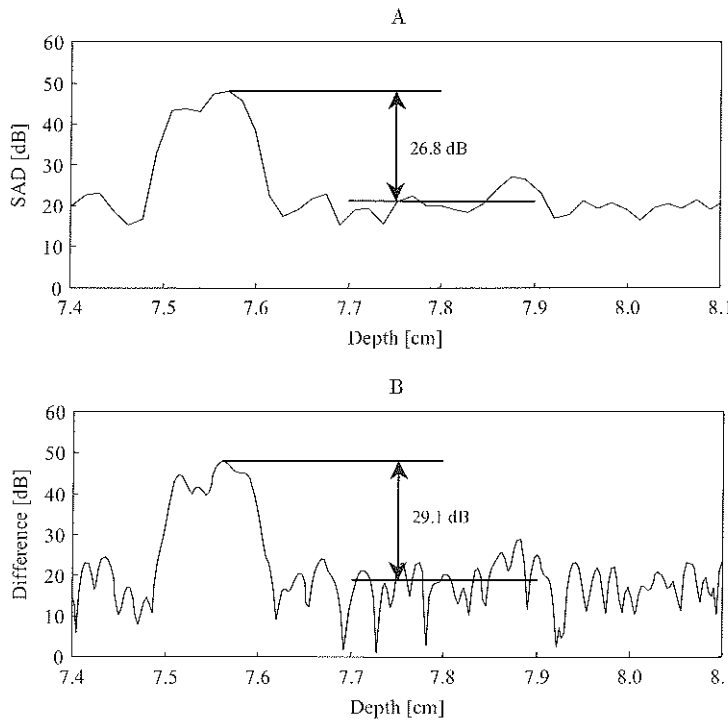


**Figure 4.8** *SAD curve (A) and difference profile (B) versus depth for the same experimental data shown in figure 4.7.*

without contrast and without release burst (line A), with contrast but without release burst (line B) and with contrast and with release burst (line C). The addition of the contrast agent hardly results in an enhancement (A and B), whereas the use of the release burst generates an enhancement of approximately 10 dB (B and C). However, the level of line C at 7.5 cm does not exceed the level of the surrounding phantom and therefore the agent-to-tissue ratio is very low. On the other hand, by the combination of the release burst strategy and subtraction processing, the stationary signal from tissue is cancelled resulting in an agent-to-tissue ratio of more than 24 dB (bottom of figure 4.9).

## Phased array transducer

Figure 4.10 shows difference profiles (in dB vs. depth) as calculated by means of equation (4.6), using the System Five phased array transducer (for the 200-$\mu$m vessel). The figure is organized as follows. The rows, *i.e.*, figure 4.10 A–C, D–F and G–I, show the results for Quantison™, Levovist® and the SonoVue™, respectively. The columns, *i.e.*, figure 4.10 A–D–G, B–E–H

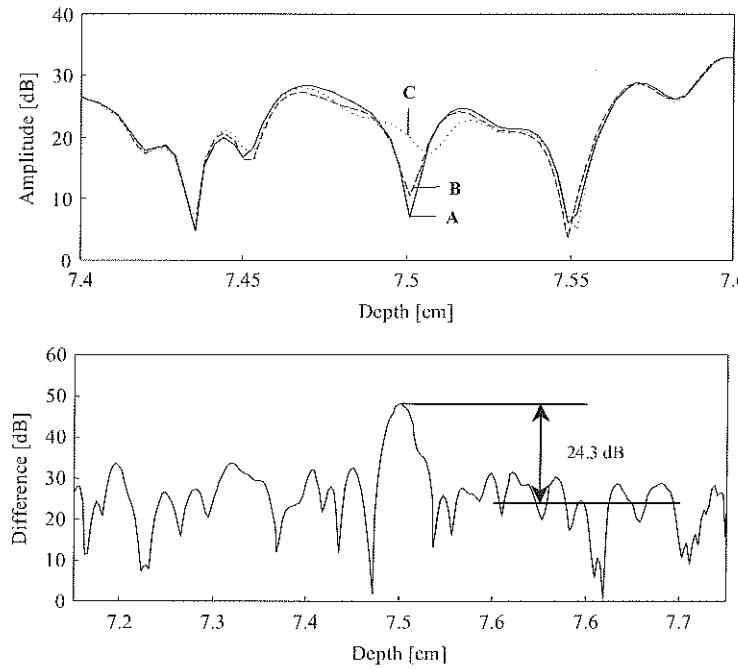


**Figure 4.9** *Experiment with the 200-μm vessel and Quantison™. Top figure shows A-mode representation of the data for three different situations, viz., without contrast and without release burst (A), with contrast but without release burst (B) and with contrast and with release burst (C). Bottom figure shows the difference profile calculated by subtracting the response of the detection pulses before and after the release burst. The sensitivity, or agent-to-tissue ratio, is calculated by the difference between the peak value and the mean value of the surrounding phantom, expressed in dB. Note that the scale of the x-axis was stretched for clarity.*

and C F I, show the results of MI = 0.4 for the detection pulses and without release burst, MI = 1.2 without release burst and MI = 0.4 with release burst, respectively. The two columns on the left are indicated in figure 4.10 as 'conventional'. This means subtracting pulse 7 and 9 and not using the release burst. The column on the right is indicated by 'release burst' and represents the new method, which means subtracting pulse 7 and 9 and using the release burst.

The vessel with contrast is located at a depth of around 9.5 cm, indicated by the peak in the difference profiles. The sensitivity, or agent-to-tissue ratio, was calculated by subtracting the reference value from the peak value. The left-most and right-most columns show that for the new method an increase in sensitivity of 43 dB, 12.5 dB and 14.8 dB can be obtained for Quantison™, Levovist® and SonoVue™, respectively. The increase in sensitivity was the highest for Quantison™, probably because the release burst was optimal for the release of gas bubbles for this agent. Further acoustic characterization should reveal what the optimal settings, like frequency, amplitude and pulse lengths of the release burst are for other contrast

agents. The peaks in figure 4.10D and 4.10G result from strong scattering and disruption by the detection pulses at a low MI, for Levovist® and SonoVue™, respectively. Note that this is not the case for Quantison™ (figure 4.10A).

The middle column of figure 4.10 shows that, for a maximum MI of 1.2 for the detection pulses and without using the release burst, a high agent-to-tissue ratio is obtained. Apparently, at this acoustic pressure free gas bubbles are released by the detection pulses. The increase in sensitivity between this configuration and the new method, *i.e.*, the middle and right most columns is only 4.2 dB, 6.8 dB and 1.6 dB for Quantison™, Levovist® and SonoVue™, respectively. However, these results were from measurements in water with the agar phantom. The

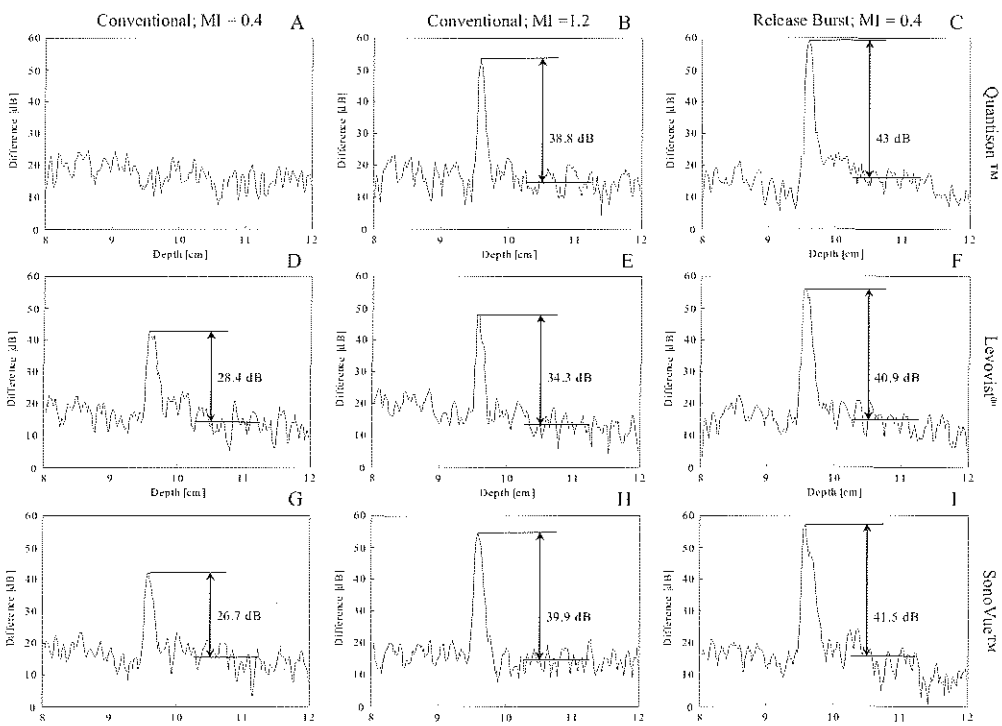


**Figure 4.10** *Difference profiles from the phantom with the 200-µm vessel and Quantison™ (A–C), Levovist® (D–F) and SonoVue™ (G–I). The left most column shows the difference profiles of two detection pulses at MI = 0.4, without using the release burst. The middle column shows the difference profiles of two detection pulses at MI = 1.2, without using the release burst. The right most column shows the difference profiles of two detection pulses at MI = 0.4, one imaging pulse before and one after the release burst. For all figures, the sensitivity, or agent-to-tissue ratio, was calculated by the difference between the peak value and the mean value of the surrounding phantom, expressed in dB.*

total attenuation of the detection pulses in this situation is only 1 dB. In tissue, on the other hand, the attenuation is much higher, especially for higher frequencies. For the settings used in this experiment (frequency of 3.3 MHz and 9.5 cm depth) the attenuation of the detection pulses in tissue would be 10–15 dB. Since the frequency of the release burst in this experiment was 0.5 MHz, the attenuation in tissue at a depth of 9.5 cm would be 2–3 dB. Therefore, for *in vivo* application, it is more realistic to compare the results of the left-most and right-most columns. Note that the peak negative pressure for the release burst was only 0.6 MPa, and that the peak negative pressure of the detection pulses at maximum MI was 2.2 MPa.

## Tissue motion

The results shown in figure 4.10 were obtained in an ideal stationary situation. Figures 4.11A and 4.11B show the results of the experiment for Quantison™ without and with tissue motion, respectively, at an MI = 0.4 for the detection pulses and with release burst. Compared to the stationary situation (A), the agent-to-tissue ratio decreased by approximately 20 dB in the case of tissue motion at a speed of 1.5 cm/s (B). However, the contrast agent was still clearly detectable.

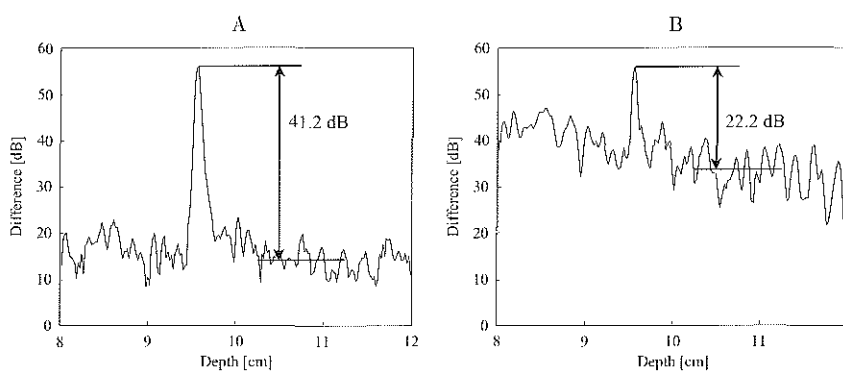


**Figure 4.11** *Difference profile from the phantom with the 200-μm vessel and Quantison™, without motion (A). Difference profile with motion, induced by moving the phased array transducer at 1.5 cm/s relative to the phantom (B).*

Due to the high sensitivity of the subtraction approach, as few as two signals can be used to detect the contrast agent in the presence of moving tissue. However, tissue motion at a velocity of 1.5 cm/s cannot be considered representative of cardiac motion, but is more representative for motion induced by patient breathing in abdominal imaging. Nevertheless, more than two signals can be used to obtain improved estimates in, for example, cardiac imaging were peak velocities of 5–10 cm/s may occur. Alternatively, clutter filters, as used with ultrasound Doppler techniques, can be used to further reduce motion artifacts[17], and will be discussed in chapter 5.

## 4.5 Discussion and conclusions

Subtraction methods have been used for some time for the detection of ultrasound contrast agents[18]. Video densitometry, for example, relies on the subtraction of pre- and post-contrast video frames[19], and was used to detect the agent in the myocardium. The method has, however, some major drawbacks. Ultrasound imaging systems apply nonlinear compression mapping and post processing techniques on the acquired RF signals before display. The purpose is to display the entire range of echoes, with a dynamic range which can be more than 100 dB, on a 30-dB range of monitor grey-levels and to produce aesthetically pleasing images. Unfortunately, this makes the subtraction of video frames ambiguous[20]. Alternative methods have been proposed that use the raw RF data instead, to obtain proper and sensitive subtraction[21]. However, for this to be effective, adequate alignment of the pre- and post-contrast data is required. Because the time intervals can be in the order of minutes, the transducer angle or position mostly changes and therefore the scan planes are not identical, resulting in residual signal from tissue. With the method proposed in this chapter, the time-interval between the two detection pulses is minimal (approximately 200–400 $\mu$s, depending on the scan depth, size of the region etc.), and thus the subtraction of the RF data can be performed in real-time, *i.e.*, it is less exposed to acquisition instabilities.

A potential limitation of the method, which applies for all imaging strategies that rely on the release of free gas bubbles or bubble disruption, is that it has to operate intermittently. Due to the bubble disruption, intermittent imaging, where single scans are made at regular time intervals (e.g. 0.2 1 Hz), is currently used to increase the life span, and therefore the efficacy of the contrast agent. However, in this mode ultrasound imaging looses its real-time character, and consequently, it is difficult to determine the position of the scanning surface. With the approach described in this chapter, the imaging can operate continuously at low acoustic pressure, *i.e.*, without disrupting the contrast agent, while the release burst operates intermittently, similar to flash-echo imaging like described by Kamiyama et al.[8]. Thus, real-time imaging can be performed, while the information of contrast rich areas will be updated after every scan of release bursts, resulting in high efficacy of the contrast agent.

With the approach described in this chapter, the power and duration of the release burst can be designed to optimize the amount, and perhaps the type, of free gas bubbles released. This, in turn, translates into a longer period of imaging per unit amount of contrast agent, or alternatively in a lower dose of contrast agent required for imaging. Additionally, optimized agent usage can reduce attenuation caused by the contrast agent itself and thus improves imaging penetration.

For the implementation in commercial ultrasound scanners, hardware changes are probably necessary. An approach under investigation is a specialized phased array transducer with two different types of transducer elements arranged in an interleaved pattern (odd-even elements). One type, e.g. the odd elements, will be used for transmitting the high-amplitude low-frequency release burst, while the second type (even elements) will be used for imaging, so transmitting a low amplitude high frequency pulse that can be used in fundamental as well as in second harmonic mode. Apart from production challenges, the odd-even element configuration may introduce additional artifacts in the images caused by grating lobes due to an effective increase of the element pitch. However, by utilizing the second harmonic field to create the images,

which is generated by propagation of the ultrasound wave through the tissue, this effect can possibly be reduced. Additionally, the advantage of the proposed approach is that for lower transmit frequencies of the release burst the acoustic pressure will be more uniform along the acoustic beam and the attenuation will be low. Thus, bubble rupture and the generation of free gas bubbles will be more uniform, resulting in uniform contrast images.

In this chapter, a novel ultrasound contrast imaging technique has been described that is based on the combination of multiple detection pulses and a separate release burst. The potential of the method to achieve high sensitivity for contrast agent detection, and high imaging resolution performance, has been demonstrated for different types of contrast agents. It can therefore be concluded that the synergy of the release burst and the real-time subtraction of signal responses of high frequency detection pulses, may result in significant image quality improvement in ultrasound contrast imaging.

# References

1. P. N. Burns, J. E. Powers, and T. Fritzsch, "Harmonic imaging: A new imaging and Doppler method for contrast enhanced ultrasound," *Radiology*, vol. 185 (P), p. 142, 1992.

2. J. E. Powers, P. N. Burns, and J. Souquet, "Imaging instrumentation for ultrasound contrast agents," in *Advances in echo imaging using contrast enhancement* (N. C. Nanda, R. Schlief, and B. B. Goldberg, eds.), pp. 139–170, Dordrecht, The Netherlands: Kluwer Acedemic Publisher, 2nd ed., 1997.

3. D. Hope Simpson, C. T. Chin, and P. N. Burns, "Pulse inversion Doppler: A new method for detecting nonlinear echoes from microbubble contrast agents," *IEEE Trans Ultrason Ferr Freq Con*, vol. 46, no. 2, pp. 372–382, 1999.

4. D. Hope Simpson, C. T. Chin, and P. N. Burns, "Perfusion imaging with pulse inversion Doppler and microbubble contrast agents: *In vivo* studies of the myocardium," in *IEEE Ultrason Symp*, vol. 2, (Sendai, Japan), 1998.

5. V. Uhlendorf and C. Hoffmann, "Nonlinear acoustical response of coated microbubbles in diagnostic ultrasound," in *IEEE Ultrason Symp*, vol. 3, (Cannes, France), pp. 1559–1562, 1994.

6. P. J. A. Frinking and N. de Jong, "Modelling of ultrasound contrast agents," in *IEEE Ultrason Symp*, vol. 2, (Toronto, Canada), pp. 1601 1604, 1997.

7. Y. Takeuchi, "Industrial use of thermoplastic micro-balloon to mimic the contrast agents and its *in vitro* behaviour including increased gas dynamics," in *IEEE Ultrason Symp*, vol. 2, (Toronto, Canada), pp. 1579–1582, 1997.

8. N. Kamiyama, F. Moriyasu, Y. Mine, and Y. Goto, "Analysis of flash echo from contrast agent for designing optimal ultrasound diagnostic systems," *Ultras Med Biol*, vol. 25, no. 3, pp. 411–420, 1999.

9. K. K. Shung, R. A. Sigelmann, and J. M. Reid, "Scattering of ultrasound by blood," *IEEE Trans Biomed Eng*, vol. 23, no. 6, pp. 460–467, 1976.

10. J. G. Miller, J. E. Perez, and J. G. Mottley, "Myocardial tissue characterization: An approach based on quantative backscatter and attenuation," in *IEEE Ultrason Symp*, pp. 782–793, 1983.

11. M. Arditi, T. Brenier, and M. Schneider, "Preliminary study in differential contrast echocardiography," *Ultras Med Biol*, vol. 23, no. 8, pp. 1185–1194, 1997.

12. J. G. Abbot, "Rationale and derivation of MI and TI: A review," *Ultras Med Biol*, vol. 25, no. 3, pp. 431–441, 1999.

13. I. A. Hein and W. D. O'Brien, "Current time-domain methods for assessing tissue motion by analysis from reflected ultrasound echoes: A review," *IEEE Trans Ultrason Ferr Freq Con*, vol. 40, no. 2, pp. 84–102, 1993.

14. L. N. Bohs and G. E. Trahey, "A novel method for angle independent ultrasonic imaging of blood flow and tissue motion," *IEEE Trans Ultrason Frerr Freq Con*, vol. 38, no. 3, pp. 280–286, 1991.

15. R. W. Barnes and F. L. Thurstone, "An ultrasound moving target indicator system for diagnostic use," *IEEE Trans Biom Eng*, vol. 18, no. 1, pp. 4–8, 1971.

16. P. A. Magnin, "A review of Doppler flow mapping techniques," in *IEEE Ultras Symp*, vol. 2, (Denver, USA), pp. 969–977, 1987.

17. J. Kirkhorn, P. J. A. Frinking, N. de Jong, and H. Torp, "Improving the sensitivity of power Doppler for ultrasound contrast imaging by using a high power release burst," in *4th Heart Centre Europ Symp Ultras Contrast Imaging*, (Rotterdam, The Netherlands), pp. 56–60, 1999.

18. M. J. Monaghan, P. J. Quigley, J. M. Metcalfe, S. D. Thomas, and D. E. Jewitt, "Digital subtraction contrast echocardiography: A new method for evaluation of regional myocardial perfusion," *Br Heart J*, vol. 59, pp. 12–19, 1988.

19. F. J. ten Cate, "Ultrasonic contrast agents for myocardial perfusion," *Imaging*, vol. 4, pp. 241–247, 1992.

20. L. J. Bos, J. J. Piek, and J. A. E. Spaan, "Background subtraction from time-intensity curves in videodensitometry: A pitfall in flow asessment using contrast echocardiography," *Ultras Med Biol*, vol. 21, no. 9, pp. 1211–1218, 1995.

21. M. J. Monaghan, J. M. Metcalfe, S. Odunlami, A. Waaler, and D. E. Jewitt, "Digital radiofrequency echocardiography in the detection of myocardial contrast following intravenous administration of Albunex®," *Eurp Heart J*, vol. 14, pp. 1200–1209, 1993.

# CHAPTER 5

# Release burst imaging of ultrasound contrast agents in moving tissue


## Abstract

*In chapter 4, a novel ultrasound contrast imaging technique was described that optimally exploits the rupture or modification of the contrast agent. This method is based on a combination of multiple high-frequency broadband detection pulses and a separate release burst. The detection pulses are used to survey the target before and after the rupture of the contrast agent. In this way, both processes (detection and release) can be optimized separately. By including more than one detection pulse before and after the release burst, temporal filters can be applied to suppress tissue clutter in fast moving regions, such as in cardiac imaging. In this way, a number of pulses are transmitted along given lines of sight to interrogate the target, similar to power Doppler techniques. Subsequently, temporal processing is applied to discriminate changes caused by disrupting contrast agent from background clutter. The method is validated for three different types of contrast agent, and is compared to harmonic power Doppler methods. The results indicate that an improvement in sensitivity in terms of agent-to-tissue ratio is achievable in dynamic situations, i.e., the method is capable of detecting the contrast agent while simultaneously suppressing clutter from slow moving tissue.*


Partly based on the manuscript: "Three-stage approach to ultrasound contrast detection" by Johan Kirkhorn, Peter J.A. Frinking, Nico de Jong and Hans Torp. To be submitted.

## 5.1 Introduction

Detecting blood flow in small vessels is of great clinical interest, since the efficiency of exchange of nutrients between blood and tissue depends on this flow. In cardiology for example, this information can reveal perfusion deficits of the myocardium. Another clinical application of current interest is tumor differentiation by blood flow measurements in the tumor. It has been shown that the mean density and the tortuousity or irregularity of the vascularity are significantly different for malignant and benign tumors[1,2]. However, small blood vessels can be hard to detect using ultrasound imaging, because the blood-to-tissue signal ratio is low. This ratio can be increased by using an ultrasound contrast agent, due to the high echogenicity of the gas bubbles.

In chapter 4, a novel ultrasound contrast imaging method has been described. The novelty of the approach is to separate the disruption or modification of the contrast agent from its detection. First, a low power detection pulse is transmitted to obtain a reference signal. This detection pulse is chosen for maximum spatial resolution and minimum contrast disruption. Second, a high-power ultrasound burst, called the *release burst*, is transmitted to modify the contrast agent and, consequently, release free gas bubbles or change the scattering properties of the contrast agent. Since the release burst is not used for imaging, it has no limitations concerning pulse length and transmit frequency, and therefore can be optimally tuned for its destructive purpose. Finally, a second detection pulse was transmitted to detect the changes that were introduced by the release burst. Based on the difference in the echo responses of the two detection pulses, a contrast specific signal is obtained.

Since this new method is based on a multi-pulse approach, it has obvious similarities with ultrasound Doppler methods. With Doppler methods, multiple pulses are transmitted along given lines of sight, and the pulse-to-pulse changes in the received echo signals are detected. In ultrasound Doppler flow measurements, the blood echo signals are corrupted with clutter signals from muscular tissue, vessel walls, etc., which can be much stronger than the blood signals even after the injection of a contrast agent. Additionally, there is always a relative movement between the ultrasound probe and the unwanted tissue targets due the beating of the heart, patient breathing and the operator moving the hand held probe. By employing specific clutter filters, these unwanted signals can be suppressed.

The simplest form of algorithms for suppressing clutter is subtracting the echoes from successive pulses, and is called *moving target indicator* (MTI)[3] or *fixed target canceller*. In chapter 4 it has been shown that this method works well for stationary situations where scattering from the contrast agent is low compared to scattering from surrounding tissue (figure 4.10). Even with induced tissue motion at a velocity of 1.5 cm/s, the contrast agent was still detectable (figure 4.11). However, in cardiology, tissue velocities can reach values between 5–10 cm/s. Therefore, more complex methods have been developed which combine the echo responses of several pulses[4,5,6]. These techniques enhance the ultrasound system's ability to separate slow moving clutter from contrast enhanced-blood, *i.e.*, it improves the system's sensitivity for contrast agent detection. This part of the system is sometimes called the *wall filter*, and is present in all forms of Doppler flow detectors[7].

In this chapter, the ultrasound contrast imaging method that has been introduced in chapter 4 is combined with a processing scheme to suppress clutter similar to those used in ultrasound

Doppler. An ensemble of pulses is transmitted in a given direction, but one of the pulses is replaced by a release burst. Additionally, a new polynomial clutter filter is applied that is specifically developed for release burst imaging. In this way, improved contrast agent detection can be obtained in the presence of highly-scattering moving tissue. The performance of release burst imaging is tested against harmonic power Doppler (HPD) imaging. For both imaging methods, the sensitivity to contrast agent detection is evaluated, together with their motion suppressing capabilities.

## 5.2 Theory

Figure 5.1 schematically shows the effect of clutter filtering in the Doppler domain. In these plots, Doppler power is projected onto the vertical axis, and the spread of Doppler frequencies is projected on the horizontal axis. The Doppler signal from stationary tissue is a strong narrow peak centered around zero Doppler frequency. The Doppler signal from moving blood is a Gaussian-shaped peak with a lower amplitude than the tissue signal and an offset in Doppler frequency, which depends on the blood velocity (figure 5.1A). The stationary tissue (clutter) signal can be as much as 40 dB higher than the signal from blood. However, the clutter can be suppressed by the use of a high-pass clutter filter, so that the blood can be detected (figure 5.1B).

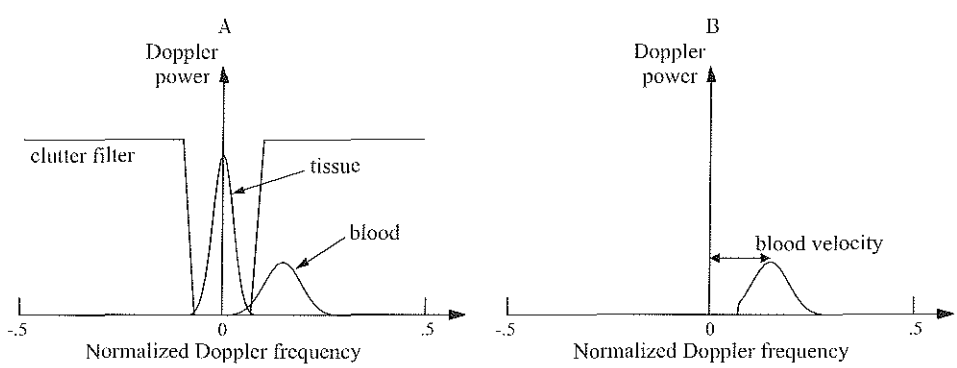


**Figure 5.1** *Representation of tissue and blood flow signal in the Doppler domain (A). Doppler power is projected on the vertical axis, the Doppler frequency is projected on the horizontal axis (the frequency is normalized to the sampling frequency). The tissue is suppressed after applying the clutter filter (B).*

Two phenomena can be noticed when a contrast agent is added to the blood pool. First, the strength of the Doppler signal from blood increases due to the highly reflective gas bubbles (figure 5.1A). Then, the power Doppler signal is the power of the signal that passes through the clutter filter (figure 5.1B). Second, the rupture of the contrast agent causes pulse-to-pulse changes in the received signals. These changes are interpreted as random Doppler shifts which means that it is not a Doppler signal due to motion but rather a measure of decorrelation,

and appears as a widening of the Doppler spectrum (figure 5.2A). The spectral broadening is apparent on the 'Doppler frequency' axis, and is represented in color Doppler imaging as a colored mosaic map (see figure 3.2). Subsequently, the clutter filter will suppress the clutter together with a substantial part of the contrast signal (figure 5.2B).

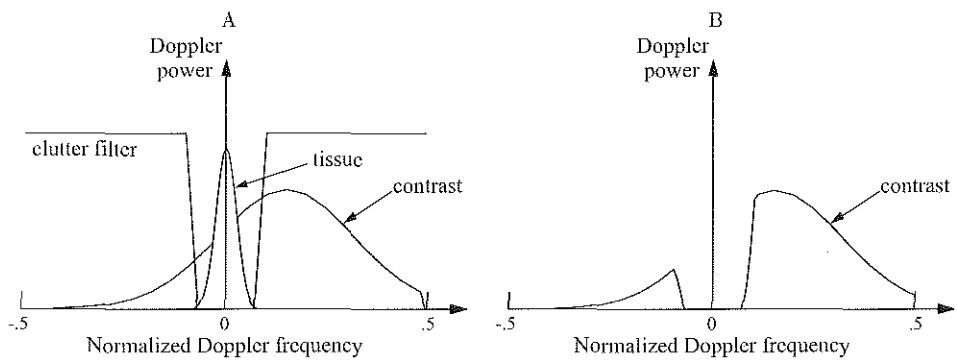


**Figure 5.2** *Effect of the addition of a contrast agent in the Doppler domain, i.e., enhancement and spectral broadening of the Doppler signal (A). The tissue clutter and a substantial part of the contrast signal is suppressed after applying the clutter filter (B).*

Blood flow velocities can be as low as 0.02 cm/s in the smallest capillary vessels[8], which is less than tissue velocity of the myocardium. Consequently, for perfusion imaging of the heart, signals from blood containing contrast agent cannot be differentiated from signals from surrounding tissue based on velocity. For low blood velocities, the Doppler spectrum from the contrast agent will be centered near zero Doppler frequency, and will be overlapped by the clutter spectrum. However, the width of the Doppler spectrum depends on the rupture rate of the contrast agent. Hence, a high rupture rate results in a wider Doppler spectrum with more of the contrast signal passing through the clutter filter. Consequently, efficient contrast agent disruption is essential for the sensitivity of Doppler methods in detecting ultrasound contrast agents.

## Signal model

The assumption is made that the scattering properties of tissue are not changed by the release burst. Furthermore, the scattered signal from the contrast agent has to be stable during the interrogation by successive pulses from a given line of sight. Additionally, the assumption is made that the amplitude of the detection pulses is low enough to prevent the contrast agent from being ruptured, and that the pulse-repetition frequency (PRF) is high enough, so that changes due to flow are minimal. The contrast agent will be modified by the release burst, *i.e.*, the contrast agent is disrupted and a variation in the signal responses from the contrast agent is detected. (Note that there may be some pulse-to-pulse variations in the signal responses from the contrast agent due to blood flow and possible modifications by the detection pulses.

This is related to the acoustic properties of the contrast agent and will differ for various types of contrast agents.)

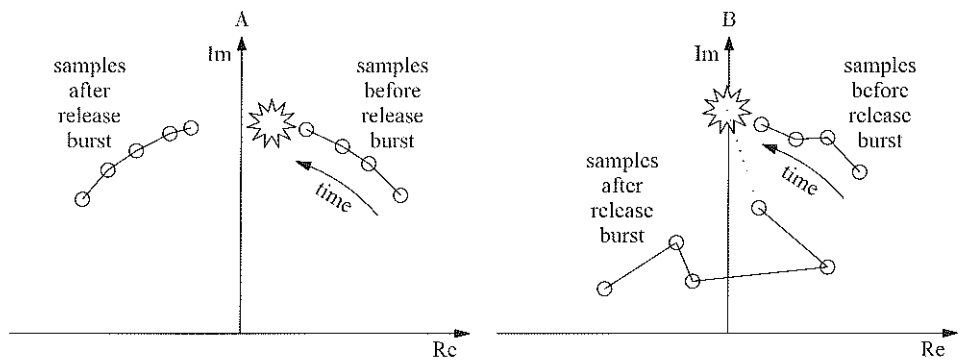


**Figure 5.3** *Complex plots of the signal model, based on a hypothetical example, showing range samples of (A) slowly moving tissue and (B) contrast agent. The release burst is indicated by the 'flash' symbol after the 4th sample.*

Figure 5.3 illustrates the expected signals from moving tissue (A) and from the contrast agent (B) in the complex domain. Complex demodulated samples from one depth range are shown counterclockwise for the successive detection pulses. The release burst is depicted by a 'flash'. For the tissue signal, the samples before and after the release burst follow the same smooth curve in the complex plane. The phase shift is caused by tissue motion. The samples from the contrast agent, on the other hand, show an almost deterministic path before the release burst. However, the contrast samples show an unpredictable behavior after the release burst, which is due to the disruption and changed scattering behavior of the contrast agent.

## Polynomial filter

Clutter filters for color flow and power Doppler imaging can be based on polynomial regression[9]. The clutter component is estimated by fitting an $N^{th}$ order polynomial to the observed samples. In this chapter, a slightly different approach is proposed. The samples before the release burst are used to calculate the polynomial, which is then extrapolated to the samples after the release burst. The power of the difference between the estimated polynomial and the observed samples after the release burst is calculated and used as a contrast specific signal.

The proposed filtering process is illustrated in figure 5.4. For moving tissue (A), the observed samples after the release burst coincide almost exactly with the estimated polynomial curve. For the contrast agent, the observed samples after the release burst are completely different from the polynomial curve. This results in a much stronger signal from the contrast agent than from tissue. A matrix implementation of the proposed polynomial filter is described in appendix A.

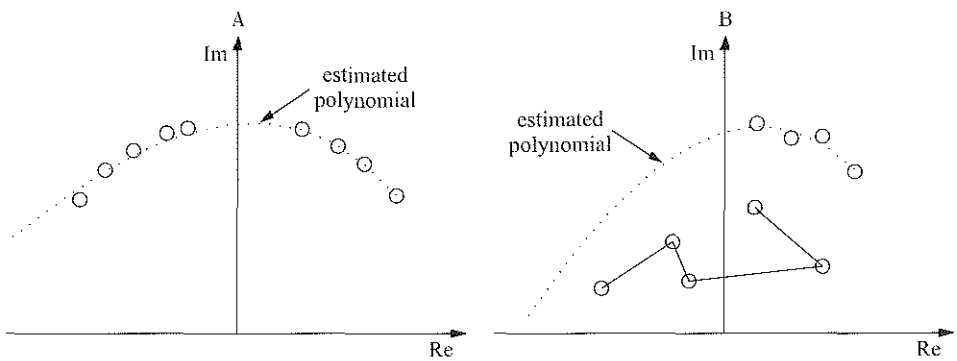


**Figure 5.4** *Principle of the proposed polynomial filtering procedure for (A) moving tissue and (B) contrast agent.*

## 5.3 Materials and methods

### Contrast agents

Three different types of contrast agents in solution were used. Quantison™ (Quadrant Ltd., Nottingham, UK) consists of air bubbles encapsulated by a relatively thick (200 300 nm) and rigid shell of human albumin. Levovist® (Schering AG, Berlin, Germany) consists of air pockets trapped in galactose sugar stabilized by palmitic acid and after suspension behave almost identical to free air bubbles. SonoVue™ (Bracco Research S.A., Geneva, Switzerland) consists of sulfur hexafluoride gas bubbles encapsulated by a flexible phospholipid shell. The used dilution for Quantison™ and SonoVue™ was 1:2000. For Levovist®, the product was suspended in 20 ml of the liquid provided. Then, 5 ml was taken and put in 2 l of Isoton® II (Coulter Electronics, Luton, UK).

### Measurement setup

#### Tissue motion

The experimental setup as described in chapter 4 was used in order to evaluate the method as proposed in this chapter. That means, a separate single-element transducer generated the release burst while the detection pulses were transmitted by a phased array transducer that was connected to a System Five ultrasound scanner (GE Vingmed Ultrasound, Horten, Norway). A custom made device (figure 4.6, left) moved the phased array transducer relative to the phantom to simulate tissue motion. In this way, an alternating up and down 'tissue motion' was produced with a peak velocity of approximately 1.5 cm/s (see also chapter 4, section 4.3).

### Release burst imaging vs. harmonic power Doppler imaging

A new series of experiments were performed to evaluate the performance of release burst imaging compared to HPD imaging as a function of the acoustic pressure. The transmit sequence was completely integrated in the System Five ultrasound scanner (GE Vingmed Ultrasound), *i.e.*, the detection pulses and the release burst were transmitted by the same phased array transducer. The machine settings for these experiments are listed in table 5.1. The acoustic

**Table 5.1** *Machine settings of the System Five ultrasound scanner (GE Vingmed Ultrasound). The second and third column on the left show the machine settings for the release burst method. The right most column shows the settings for HPD.*

| | Detection pulses | Release burst | Harmonic power Doppler |
|---|---|---|---|
| Frequency [MHz] | 1.7 | 1.7 | 1.7 |
| Pressure (p-p) [MPa] | 0.16–1.0 | 1.6 | 0.2 1.5 |
| Pulse length [cycles] | 2 | 4 | 2 and 4 |
| # of pulses | 6 | 1 | 6 |
| PRF [kHz] | 4 | | 4 |

pressure of the release burst was fixed to 1.6 MPa, while the pressure for the detection pulses was varied with a maximum of 1.0 MPa. The maximum pressure for the HPD method was 1.5 MPa. Two pulse lengths were chosen for the HPD method. The 2-cycle pulse length was

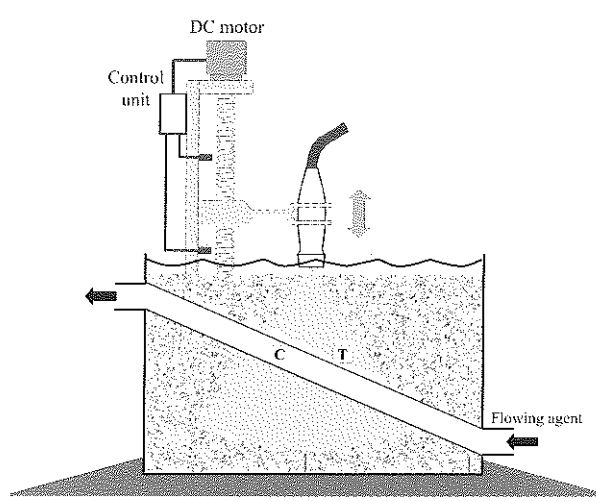


**Figure 5.5** *Experimental setup showing motion device, the phased array transducer and the phantom with the latex tube. The two ROI's, one in the tube and one in the phantom, are indicated by C and T, respectively.*

similar to the detection pulses of the release burst method and was most optimal for imaging. The 4-cycle pulse length was similar to the release burst and was optimal for contrast agent disruption.

The experimental setup is shown in figure 5.5. A ultrasound flow phantom (409A, Radiation Measurements Inc., Middelton, WI, USA) was used. The phantom is made of tissue-mimicking material with an acoustic velocity of 1540 cm/s and an attenuation of 0.5 dB $cm^{-1}$ $MHz^{-1}$. A latex tube, with an inner diameter of 1 cm, was incorporated in the phantom. A flow setup was constructed by connecting the latex tube to a gear pump (5004U, Watson-Marlow Ltd., Cornwall, UK). A flow rate of 1.8 ml/s was obtained, which corresponds to an average velocity in the tube of approximately 2.3 cm/s. The phased-array transducer was mounted in the same motion device as used in chapter 4. The transducer was positioned 7 cm above the latex tube, and was continuously moving up and down. During its motion, the transducer was coupled to the phantom material through a water bath. The peak velocity as measured in the phantom was approximately 4 cm/s. The radio frequency (RF) data was recorded in triggered mode, synchronized to the motion of the transducer.

**Processing**

For HPD imaging, power profiles from six pulses before the release burst were calculated using power-Doppler processing with a polynomial regression clutter filter[9]. Second harmonic filtering was applied to the received signals. For the release burst method, three pulses before and after the release burst were combined, and power profiles were calculated using the new polynomial filtering algorithm.

The mean pixel intensity of two regions of interest (ROI) was calculated from the processed digital RF data. The ROI's are shown in the figure 5.5; one in the latex tube and one in the phantom, and are indicated by $C$ (= contrast) and $T$ (= tissue), respectively. The agent-to-tissue ratio (ATR) can be defined as a measure for the sensitivity of the techniques for contrast agent detection in moving tissue. The ATR was calculated by subtracting the mean pixel intensity of $T$ from the mean pixel intensity of $C$,. All processing and visualization were performed off-line using Matlab® (The Mathworks Inc., Natick, USA).

## 5.4 Results

### Tissue motion

The experimental data for Quantison™ with tissue motion, obtained from the same data as in chapter 4 was used. Figures 5.6A–D show the results of the release burst method together with the proposed polynomial filtering procedure. Different orders for the polynomial clutter filter were applied, *viz.*, N=0, N=1, N=2 and N=3, and the filtered results, as calculated by means of equation (A.9), are shown in figures A, B, C and D, respectively.

The 200-$\mu$m capillary fiber containing contrast was located at a depth of around 9.5 cm, indicated by the peak in the power profiles. The sensitivity or ATR of the method was calculated by subtracting a reference value from the peak value. Like described in chapter 4, the reference

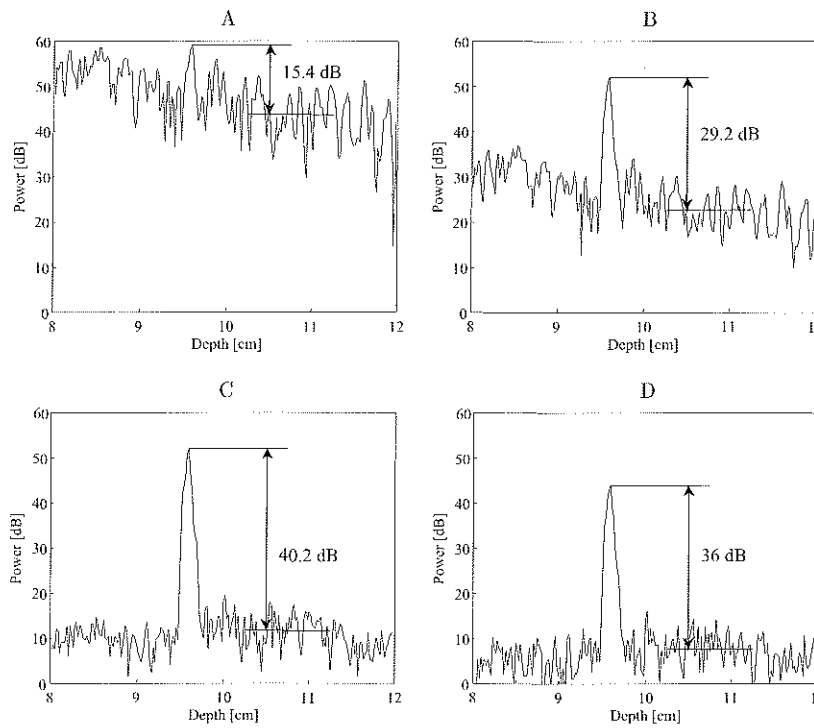


**Figure 5.6** *Difference profiles for the experiment with motion (1.5 cm/s) and Quantison™. Different polynomial clutter filter orders were used. A) N=0 ; B) N=1; C) N=2; D) N=3.*

value was calculated by averaging the response of the phantom over a 1-cm section next to the capillary fiber. The ATR increased from 15.4 dB (A) to 40.2 dB (C). For the zero order clutter filter, the ATR was smaller compared to figure 4.11B. This is due to the averaging character of the clutter filter. However, by using a second order clutter filter, the ATR was comparable to the ATR of the stationary situation (figure 4.10C), for a tissue velocity of 1.5 cm/s. Finally, it can be observed from figure 5.6D that a third order polynomial clutter filter was too high for this experiment, *i.e.*, the filter characteristic was such that a substantial part of the signals from the contrast agent was removed. Therefore, clutter filtering should be used with care since too much of the contrast signal can be removed by the clutter filter, which results in lower agent-to-tissue ratios.

### Release burst imaging vs. harmonic power Doppler imaging

With release burst imaging, a better ATR was obtained than with HPD, both for the 2- and 4-cycle transmitted pulses. The results are shown in figure 5.7A–C for Quantison™, Levovist® and SonoVue™, respectively. A higher ATR was obtained for the 4-cycle HPD over the 2-cycle HPD. This can be explained by the more destructive character of the 4-cycle transmitted pulses. For Quantison™, the ATR of HPD was close to zero for pressure amplitudes up to 0.7 MPa. At these low acoustic pressures, the ATR for the release burst method was more than 20 dB higher than for the HPD methods. For higher pressures, the difference in ATR between the release burst method and 4-cycle HPD decreased due to the increased disruption of the contrast agent by the relatively long transmitted pulses. However, the difference in ATR between the release burst method and 2-cycle HPD slightly increased as a function of pressure.

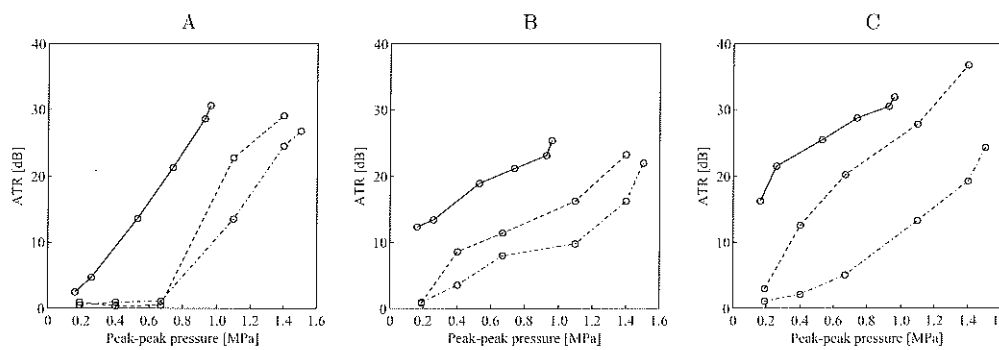


**Figure 5.7** *Agent-to-tissue ratio (ATR) vs. transmit pressure for (A) Quantison™, (B) Levovist® and (C) SonoVue™. ——= release burst imaging; -----= 4-cycle harmonic power Doppler imaging; -·-·-= 2-cycle harmonic power Doppler imaging. Second order clutter filtering was applied in all the examples.*

The gain in ATR of the release burst method over HPD, at an acoustic pressure of 0.2 MPa, was 12 and 15 dB for Levovist® and SonoVue™, respectively. The agents were hardly detectable with the HPD method at these pressure values. The high ATR for the release burst method may reflect contrast agent disruption, rather than detecting flow. For higher values of acoustic pressure, the ATR of HPD increased for both agents, probably due to flow detection and contrast agent disruption. However, the ATR for the release burst method was higher than the ATR for 2 and 4-cycle HPD, for acoustic pressures up to 1 MPa.

## 5.5 Discussion and conclusions

Release burst imaging exploits the rupture of the contrast agent and the subsequent release of free gas bubbles, which is mainly observed for Quantison™ and is described in chapter 3. However, the method generally detects changes in the scattering properties of contrast agents, and consequently works for different types of agents, as has been shown by the examples in this

chapter. Moreover, the method offers the possibility to optimize the release burst for all types of contrast agents, since rupture and detection are completely separated. Additionally, because the transient effect of disrupting contrast agents is used, contrast agents can be detected that move with the same velocity as the tissue.

The results shown in figure 5.7 indicate that for high acoustic pressures, the ATR obtained with 4-cycle HPD is close to or higher than the ATR obtained with the release burst method at 1 MPa. However, the same frequency was used for the release burst and the HPD pulses. In a new experimental transducer embodiment, the release burst elements can physically be separated from the elements that generate the detection pulses. Then, by optimal tuning of the release burst, a highly efficient contrast agent disruption can be obtained (this is explained in more detail in chapter 4). Additionally, in practical situations with more attenuation, the range of operation of the acoustic pressure will be lower than 1 MPa. The results presented in this chapter have shown that in this situation the ATR for release burst imaging is higher than for HPD imaging.

Good clutter suppression performance has been shown in figure 5.6, even with complex motion due to the small 'wiggles', which introduce lateral decorrelation (see M-mode recording of the alternating up and down motion of the transducer in figure 4.6). Higher order clutter filters could be used for more dynamic and irregular tissue motion but also may suppress a considerable part of the contrast agent signal. Furthermore, adaptive clutter filtering can be applied for specific contrast agent and tissue properties and depth dependent filtering, as described by Bjærum and Torp[10]. Also, a higher number of pulses is beneficial for better estimation of the polynomial. However, this increases the acquisition time, and possibly reduces the contrast specificity due to unwanted destruction of contrast agent by the imaging pulses.

The experiments described in this chapter mainly focused on the sensitivity of the release burst and HPD method rather than on the imaging resolution. However, from a theoretical point of view, release burst imaging offers the possibility for high ATR's with broad band detection pulses giving high spatial resolution. For HPD, on the other hand, the ATR were highest for long narrow band pulses resulting in poor axial resolution.

An alternative polynomial fitting procedure can be applied for agents that are easily disrupted, such as Levovist®. Such agents will be disrupted by the detection pulses, and will thereby show a random transient behavior before the release burst. The release burst will destroy most of the remaining contrast, and signals from the detection pulses after the release burst will essentially contain only the tissue clutter component. Estimation of the clutter polynomial therefore may be applied to the samples after the release burst, and a backward extrapolation should be applied to the samples acquired before the release burst.

A more generalized polynomial fitting procedure may be that any of the samples before and after the release burst are used for estimation of the polynomial. Then any of the samples (before or after the release burst) can be used when subtracting the observed samples from the estimated polynomial curve. Such an approach will be suitable for next generation agents such as SonoVue™, which have flexible encapsulating materials. These agents are more persistent to ultrasound, and produce strong scattering both before and after the release burst. This means that both the clutter and contrast components of the response is present before and after the release burst, and estimation of the clutter component should be based on all available samples.

Finally, the release burst method may be combined with second harmonic filtering or with Pulse-Inversion methods. Consequently, the transmit frequency of the pulses in the detection pulses must be chosen at a frequency which allows sufficient sensitivity for reception at the second harmonic frequency.

## Conclusions

In this chapter, the new contrast imaging technique as described in chapter 4 has been extended to an approach similar to those used in ultrasound Doppler processing. Through this strategy, a special clutter filter approach could be integrated in the release burst imaging method. Therefore, the high ATR, *i.e.*, sensitivity, of the proposed contrast imaging method is a result of the successful synergy of optimal contrast agent detection and the ability to suppress moving tissue clutter.

# References

1. S. A. Bigler, R. E. Deering, and M. K. Brawer, "Comparison of microscopic vascularity in benign and malignant prostate tissue," *Human Pathol*, vol. 24, no. 2, pp. 220–226, 1993.

2. J. W. Baish, Y. Gazit, D. A. Berk, M. Nozue, L. T. Baxter, and R. K. Jain, "Role of tumor vascular architecture in nutrient and drug delivery: An invasion percolation-based network model," *Microvasc Res*, vol. 51, no. 3, pp. 327–346, 1996.

3. P. A. Magnin, "A review of Doppler flow mapping techniques," in *IEEE Ultras Symp*, vol. 2, (Denver, USA), pp. 969–977, 1987.

4. J. A. Jensen, "Stationary echo cancelling in velocity estimation by time-domain cross-correlation," *IEEE Trans Med Imag*, vol. 12, pp. 471 477, 1993.

5. A. Kadi and T. Loupas, "On the performance of regression and step-initialized IIR clutter filters for color Doppler systems in diagnostic medical ultrasound," *IEEE Trans Ultrason Ferr Freq Con*, vol. 42, no. 5, pp. 927–937, 1995.

6. A. P. G. Hoeks, J. J. van de Vorst, A. Dabekaussen, P. J. Brands, and R. S. Reneman, "An efficient algorithm to remove low frequency Doppler signals in digital Doppler systems," *Ultrason Imag*, vol. 13, no. 2, pp. 135–144, 1991.

7. J. E. Powers, P. N. Burns, and J. Souquet, "Imaging instrumentation for ultrasound contrast agents," in *Advances in echo imaging using contrast enhancement* (N. Nanda, R. Schlief, and B. Goldberg, eds.), pp. 139–170, Dordrecht, The Netherlands: Kluwer Acedemic Publisher, 2nd ed., 1997.

8. J. A. Jensen, *Estimation of blood velocities using ultrasound: A signal processing approach (chp 3, pg 64)*. Cambridge: Cambridge University Press, 1996.

9. H. Torp, "Clutter rejection filters in color flow imaging: A theoretical approach," *IEEE Trans Ultrason Ferr Freq Con*, vol. 44, no. 2, pp. 417–424, 1997.

10. S. Bjærum and H. Torp, "Optimal adaptive clutter filtering in color flow imaging," in *IEEE Ultrason Symp*, vol. 2, (Toronto, Canada), pp. 1223–1226, 1997.

# CHAPTER 6

# Ultrasound contrast imaging: Current and new methods


## Abstract

*For 10 years, it was thought that ultrasound contrast agents could be sufficiently detected and imaged with the conventional imaging techniques, currently referred to as fundamental imaging. However, it appeared that fundamental imaging was not sensitive enough to detect the contrast agents in the presence of tissue. New imaging techniques that are based on specific properties, like nonlinear and transient scatter characteristics, proved to be more sensitive. Ultrasound contrast imaging modalities used today are, fundamental imaging, second harmonic imaging, harmonic power Doppler imaging and pulse inversion imaging. Second harmonic imaging is still not optimal for perfusion imaging applications. However, in combination with Doppler techniques such as power Doppler, it is one of the most sensitive techniques currently available. New modalities like release burst and subharmonic imaging are emerging. Nevertheless, a complete understanding of the ultrasound-contrast agent interaction is essential for further improvements of current detection methods, and the development of new imaging techniques.*


Based on the manuscript: "Ultrasound contrast imaging: Current and new methods" by Peter J.A. Frinking, Ayache Bouakaz, Johan Kirkhorn, Folkert J. ten Cate and Nico de Jong. Submitted for publication.

## 6.1 Introduction

The diagnostic applications of ultrasound imaging have been expanded enormously for the last decades. It has been recognized as a well-established diagnostic technique for clinical decision making. Significant improvements in equipment have contributed to the understanding of anatomy and function of different organs. With the introduction of real-time two-dimensional (2D) imaging, different anatomical structures in the body could be imaged non-invasively. Also, blood flow measurements in large vessels and the heart became feasible using ultrasound Doppler techniques. Nevertheless, new applications as well as technological innovations are continuously being developed. Real-time three-dimensional imaging, for example, provides volumetric information rather than cross-sectional information like obtained with conventional 2D imaging. Additionally, with the utilization of ultrasound contrast agents, perfusion imaging of the myocardium or tumors has become feasible, and provides meaningful physiological and pathological information for clinical decision making.

### Ultrasound contrast agents

In 1989, Ophir and Parker[1] gave a summary of the use of ultrasound contrast agents (UCA) in medical imaging. Five types of agents with different physical properties were classified, *viz.*, free gas bubbles, encapsulated gas bubbles, colloidal suspensions, emulsions and aqueous solutions. In those days, it was a main challenge to produce small microbubbles which could pass through the lung capillary circulation, and were stable enough to reach the left heart after an intravenous injection. Currently, most of the contrast agents reach the left ventricle cavity of the heart, and are based on free gas bubbles or are stabilized by encapsulation to avoid rapid disappearance. They are either air filled or contain gases which dissolve poorly in the blood, and have mean diameters smaller than 7$\mu$m. More than ten agents are currently under investigation and tested in clinical trials (table 1.1). However, there are only three transpulmonary agents commercially available, *viz.*, Levovist® (Schering AG, Berlin, Germany), Albunex® and Optison™ (Mallinckrodt, St. Louis, USA).

### Ultrasound-contrast agent interaction

When a gas bubble is hit by an ultrasound wave it generates two kinds of responses. First, the wave will be reflected at the surface of the bubble because of the large difference in acoustic impedance between the surrounding medium and the gas inside the bubble. More importantly is, however, that when the bubble size is much smaller than the wavelength of the ultrasound wave, it is forced into volume pulsation (for a 3 MHz ultrasound wave, the wavelength in water is 0.5 mm). In the simplest situation, the size of the bubble decreases in the positive half-cycle of the ultrasound wave, and the bubble expands in the negative half-cycle. The volume pulsation of the bubble is frequency dependent and shows a clear maximum at a specific frequency. This is referred to as the resonance frequency, which is inversely related to the bubble size[2]. The resonance phenomenon is an important effect, since a resonating bubble behaves as a source of sound rather than a passive reflector and, therefore, yields an enhancement of the backscatter signal.

The response of a gas bubble to an ultrasound wave depends on the acoustic pressure amplitude and can be divided into three regimes. For small amplitudes of the ultrasound wave, the relative compression and expansion of the bubble are the same and, therefore, the bubble size is linearly related to the applied acoustic pressure. For higher amplitudes, however, compression generally retards relative to expansion and non-linearity occurs. Consequently, the bubble size is not linearly related to the applied acoustic pressure[3], and the bubble vibration contains second and higher multiples of the transmitted frequency. In this way, the backscatter signal from the bubble does not only contain the fundamental (transmitted) frequency, but also harmonic frequencies, most notably at twice the fundamental frequency. This 'reflection' effect is not shown by tissue and, therefore, it offers the possibility to separate the response of the bubble from that of surrounding tissue.

If the amplitude of the acoustic wave is increased more, the scattering level of most of the contrast agents increases abruptly for a short time. This has been associated with bubble rupture and release of free gas bubbles (chapter 3). The irreversible effect is transient and lasts until the released free gas bubbles are dissolved in the surrounding liquid at a rate that depends on the type of gas and its dissolvability in the liquid. Furthermore, the scattered signal becomes highly nonlinear.

In this chapter, an overview is given of ultrasound contrast imaging methods that are currently available or under investigation. They all utilize one of the bubble signatures that are demonstrated in one of the regimes of the bubble response. Specific properties of each method are emphasized, and are given from a technical point of view, illustrated with some clinical examples. The following methods are described:

- Fundamental B-mode imaging
- Harmonic B-mode imaging
- Harmonic power Doppler imaging
- Pulse inversion imaging
- Release burst imaging
- Subharmonic imaging.

## 6.2 Fundamental B-mode imaging

With the introduction of UCA, it was thought that it would be sufficient to detect and image them with conventional imaging methods, currently referred to as fundamental imaging. In this mode, UCA simply enhance the backscatter signal, which is demonstrated by an increase in grey-scale level (figure 6.1A). This has been employed in combination with conventional 2D B-mode imaging to create images of greater clarity. For example, left ventricular opacification improves endocardial border detection, which results in a better assessment of wall motion abnormalities. However, for the myocardium, the ratio of blood volume and tissue is approximately 10%. Consequently, for concentrations used in clinical studies the increase in

scattering from UCA in the myocardium will only be several dB's. Therefore, fundamental B-mode imaging results in poor contrast agent detectability in the presence of tissue, generally expressed as agent-to-tissue ratio.

More recently, it appeared that for high acoustic amplitudes (high mechanical index) transient enhanced scattering may occur (chapter 3). The amplitude of the ultrasound wave is indicated on ultrasound scanners by the mechanical index (MI), which is defined as the ratio of the peak negative pressure, in MPa, and the square root of the frequency, in MHz[4]. In conventional B-mode imaging, the enhanced scattering may be visualized as bright echogenic areas (figure 3.1). Although the increase in echogenicity can be substantial, in hyperechoic regions or very small vessels where the number of bubbles is low, e.g. the myocardium, echoes from surrounding tissue can easily mask this increased echogenicity.

The transient enhanced scattering effect is most effective when the ultrasound wave hits the bubbles for the first time. This has resulted to the development of triggered imaging[5] as a new modality. In the triggered mode, single scans are made at regular time intervals (e.g. 0.1–1 Hz), resulting in an increased efficacy of the agent. However, ultrasound imaging looses its real-time character in this mode. This is not only limited to fundamental imaging but applies to all contrast imaging methods that use the transient characteristic of UCA.

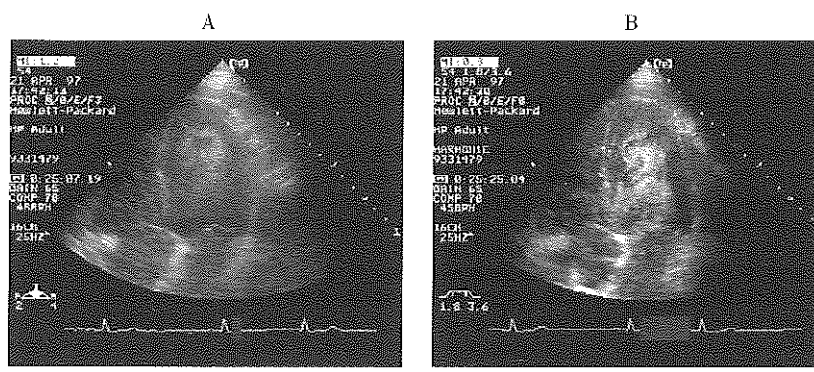


**Figure 6.1** *Apical four chamber view of a human heart after an intravenous administration of Levovist®. (A) Fundamental imaging, i.e., transmitting and receiving at 3 MHz. (B) Second harmonic B-mode imaging, i.e., transmitting at 1.8 MHz and receiving at 3.6 MHz.*

## 6.3 Harmonic B-mode imaging

New imaging techniques are continuously being developed and are based on contrast agent specific properties. By utilizing these properties, it is possible to detect UCA in tissue, even if the fundamental backscatter component is low compared to the scattering of surrounding tissue. Second harmonic (B-mode) imaging is a method where the ultrasound system separates the harmonic part of the received signal from the fundamental part and then processes the

harmonic signal alone. In figure 6.1, fundamental (A) and second harmonic (B) are shown after an intravenous injection of Levovist®. In the second harmonic mode, a complete and homogeneous opacification of the left ventricle cavity was obtained.

To increase the sensitivity of the system in detecting the agent, the spectral overlap between the fundamental and harmonic parts has to be reduced (figure 6.2). This is achieved by transmitting narrow-band signals, which, in turn, deteriorates the imaging resolution. Consequently, system optimization consists of finding the most optimal balance between these two aspects, and generally is called the contrast detectability and imaging resolution trade-off.

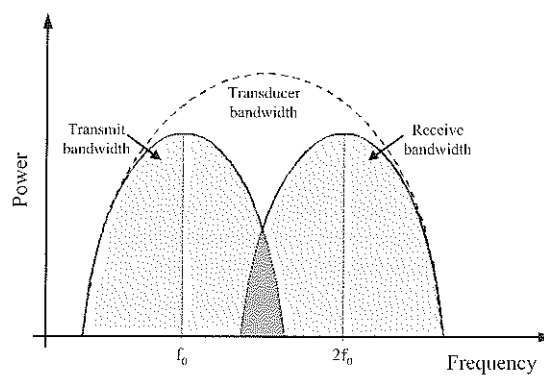


**Figure 6.2** *Overlap between transmit ($f_0$) and receive ($2f_0$) passbands (dark grey area) results in a residual signal of the fundamental image in the filtered harmonic image.*

For ultrasound waves transmitted at high acoustic pressures, slight non-linearities in sound propagation through tissue occur that gradually deform the shape of the waves (figure 6.3A)[6]. As a result, harmonic frequencies are generated, which were not present in the transmitted wave close to the transducer (figure 6.3B). The harmonic frequencies will linearly be reflected

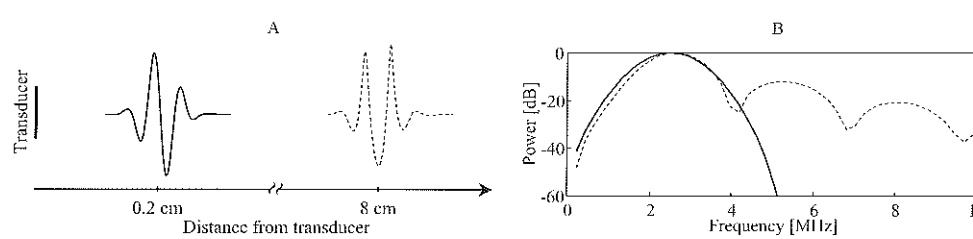


**Figure 6.3** *Simulation results for a propagating ultrasound wave transmitted by a focused single element transducer. (A) Change of shape of the ultrasound wave as it propagates through water at 0.2 cm (——), and 8 cm (-----) from the transducer. (B) Corresponding (normalized) spectra. The aperture of the transducer was 28 mm, the focus was at 75 mm, the frequency was 2.5 MHz and the peak negative pressure was 100 kPa.*

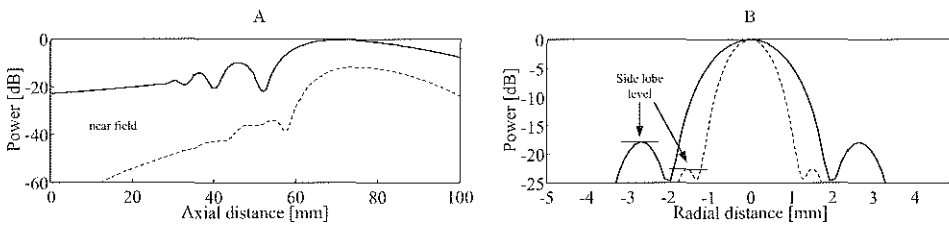


**Figure 6.4** *Same simulation as used for figure 6.3. (A) Normalized axial beam profile of the fundamental (——) and second harmonic (-----) beam. (B) Normalized lateral beam profile of the fundamental (——) and second harmonic (-----) beam at the focus.*

by surrounding tissue and, therefore, can mask the nonlinear response from UCA. Consequently, all imaging methods that exploit harmonic filtering for improved contrast agent detection are obscured by a residual tissue component due to nonlinear propagation. Therefore, the maximal obtainable agent-to-tissue ratio is limited for these methods.

Although harmonic imaging was originally developed for UCA, it turned out that also without UCA the image quality improved considerably compared with fundamental imaging. This is generally called 'native harmonic' or 'tissue harmonic' imaging to distinguish it from harmonics generated by UCA. There are two aspects that are critical for the improvement of tissue harmonic imaging[7]. First, harmonic frequencies are absent at the transducer face and they build up progressively. Consequently, there is hardly any harmonic energy in the near field, and most of the harmonics develop beyond the chest wall (figure 6.4A). Therefore, selective display of the harmonic frequency will show less near-field artifacts. Secondly, the harmonic component has

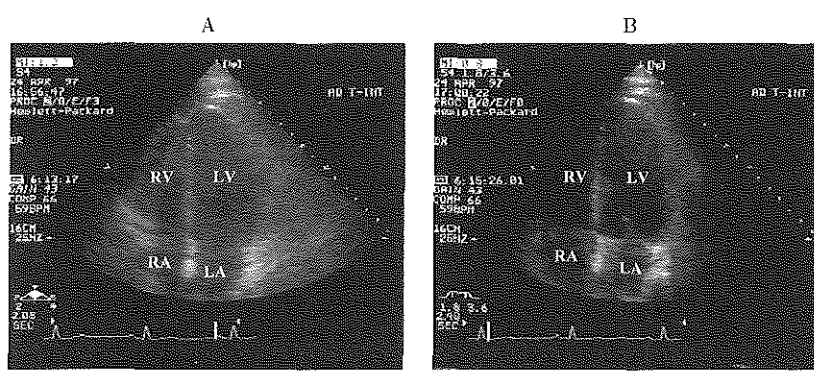


**Figure 6.5** *Apical four chamber view of the human heart. RV=right ventricle; LV=left ventricle; RA=right atrium; LA=left atrium. (A) Fundamental imaging, i.e., transmitting and receiving at 3MHz. (B) Tissue harmonic imaging, i.e., transmitting at 1.8 MHz and receiving at 3.6 MHz.*

a quadratic relationship to the fundamental one. Thus, most of the harmonic energy originates from the strongest part of the beam, whereas the weaker parts of the beam, *i.e.*, side lobes and grating lobes, give rise to a small contribution (figure 6.4B). Since side lobes and grating lobes are sources of noise and artifacts, selective harmonic imaging improves the signal-to-noise ratio, and thus results in cleaner images. Another consequence of the quadratic relationship between the harmonic and fundamental components is that the lateral beam width is narrower for the second harmonic beam than for the fundamental beam (figure 6.4B). This translates in a better lateral resolution of the second harmonic image compared to the fundamental image.

The aforementioned improvements explain why, for example, a better endocardial border definition can be obtained in harmonic mode. This is described by Kasprzak et al.[8], and shown in figures 6.5A and B.

## 6.4 Harmonic power Doppler imaging

With conventional ultrasound Doppler imaging, blood velocity can be measured by tracking scattering objects in a region of interest. Unlike conventional Doppler, power Doppler does not provide information about the direction of the flow but instead displays the power of the Doppler signal (figure 6.6). This has proven to be a more sensitive method in terms of signal-to-noise-ratio and low flow detectability[9]. With the addition of a contrast agent, the signals received from blood containing contrast are enhanced and the detectability of flow from small vessels is increased further. However, since most of the Doppler techniques are multi-pulse

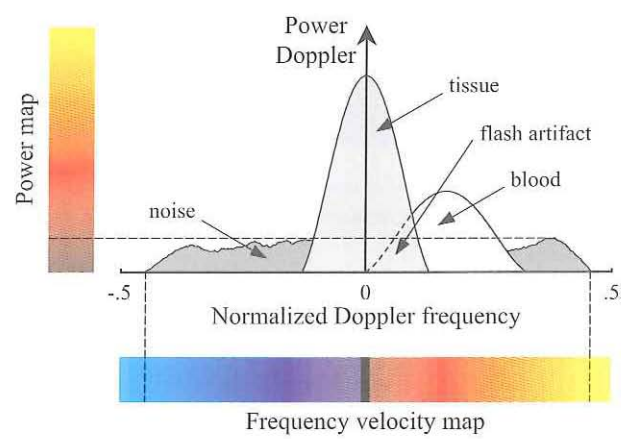


**Figure 6.6** *Diagram showing the advantage of power Doppler over color Doppler (velocity mode)[9]. In the power Doppler mode, the power of the Doppler signal is displayed instead of frequency. Consequently, noise from the Doppler receiver at high gain settings is mapped to a single color instead of many colors as in the velocity mode, resulting in an effective increase of the dynamic range. The 'tissue' signal overlapping the 'blood' signal causes a flash artifact.*

techniques, *i.e.*, a packet of pulses is transmitted in a given line of sight, they are susceptible to tissue motion which is not eminent in B-mode imaging. Tissue motion generates Doppler signals (clutter) that can be even stronger than the contrast-enhanced signals with the same Doppler shift frequencies as the signals from blood. This results in a flash artifact, which is a severe problem in Doppler applications. The flash artifact or clutter can be reduced by the combination with second harmonic filtering. This makes harmonic power Doppler an effective tool for the detection of flow in the small vessels of organs, which may be moving with cardiac pulsation or respiration. It is currently considered as one of the most sensitive techniques available in terms of agent-to-tissue ratio.

Another application of Doppler imaging in combination with UCA arises for ultrasound waves transmitted at a high MI. Every time a pulse (in the same direction) is transmitted, transient enhanced scattering occurs, *i.e.*, the contrast agent is disrupted or modified. In this way, changes in the scattering of the contrast agent are induced. This effect can be detected very accurately since Doppler is sensitive to changes between backscatter signals from successive pulses.

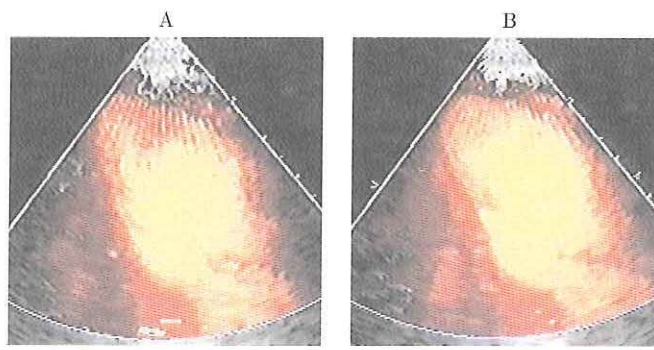


**Figure 6.7** *2-chamber view of a patient with an inferior infarction after thrombolysis. (A) Harmonic power Doppler imaging, triggered every heartbeat. (B) Harmonic power Doppler imaging, triggered every fifth heartbeat.*

An example of a harmonic power Doppler study performed on a patient is given in figure 6.7, where a constant intravenous infusion of Levovist® was administered. By changing the triggering interval from every heartbeat (figure 6.7A) to every fifth heartbeat (figure 6.7B), the myocardium appears to be enhanced. This is explained by the low flow rate in the myocardium. The reappearance rate of the contrast agent provides a measure of the mean myocardial blood velocity, and is sometimes called 'microbubble destruction/reperfusion method'[10]. By changing the trigger interval from 1 every heart beat to 1 every 5 heart beats, flash echo artifacts can be excluded, and the enhanced area in the image may be an indication of myocardial perfusion.

## 6.5 Pulse inversion imaging

The limited bandwidth of current transducers forces the transmit bandwidth to be narrow to minimize the spectral overlap between the fundamental and second harmonic parts of the received spectrum (see figure 6.2). A new technique, called pulse inversion, has been developed and largely overcomes the contrast detectability and imaging resolution trade-off[11]. In pulse inversion imaging, a sequence of two ultrasound waves is transmitted into tissue (figure 6.8). The second wave is transmitted after a suitable delay and is an inverted replica of the first wave. For a linear medium, the response of the second wave is an inverted copy of the response from the first wave and the sum of the two responses is zero. For a nonlinear system, e.g. gas bubbles, the responses will not be inverted copies. The sum is not zero and the rest value is related to the degree of non-linearity. The main advantage of pulse inversion over harmonic imaging and harmonic power Doppler imaging is that it can function over the entire bandwidth of the received echo signal and, therefore, achieves superior imaging resolution. It has been shown that pulse inversion imaging can be performed at low MI, prolonging the lifetime of the contrast agent and perhaps obviating the need for intermittent imaging[12]. In radiology, where continuous imaging is common, the method has improved the image quality substantially.

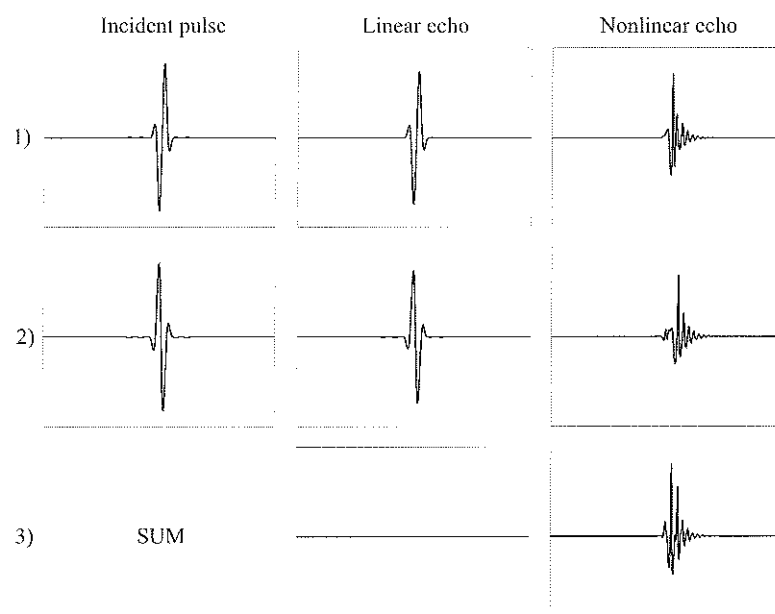


**Figure 6.8** *Principle of pulse inversion imaging[11]. 1) An acoustic pulse is transmitted and echoes from linear and nonlinear scatterers are detected. 2) An inverted copy of the same pulse is transmitted and echoes are detected again. When the two echoes are added, only the nonlinear echoes are retained.*

Nevertheless, pulse inversion is susceptible to motion since it is a multi-pulse technique. This implies that the method is less suitable for cardiology. Therefore, pulse inversion detection and Doppler detection have been combined into one technique called pulse inversion Doppler. This technique exploits the advantages of both detection schemes[11], which means that more than 2 pulses are transmitted and special Doppler filters are applied to remove tissue motion. However, nonlinear propagation effects still limit the maximal obtainable agent-to-tissue ratio.

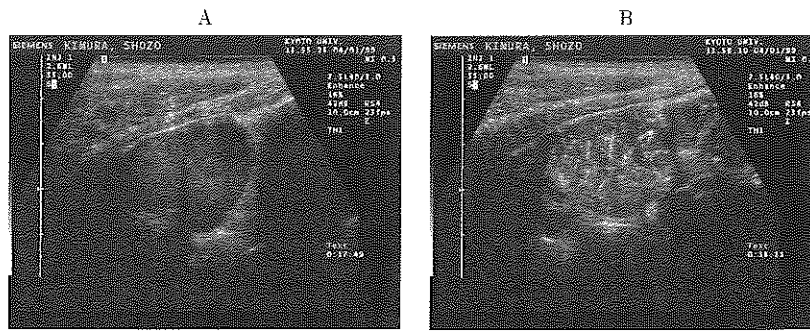


**Figure 6.9** *Example of pulse inversion imaging of a human liver with a hepacellular carcinoma[13]. (A) Baseline recording. (B) After Optison™ has been administered. The images were recorded in continuous mode (Courtesy: F. Moriyasu, Kyoto University, Japan).*

An example of pulse-inversion imaging is shown in figure 6.9[13]. Figure 6.9A shows a baseline recording of the liver of a patient with a hepacellular carcinoma (HCC). After the administration of Optison™, a tortuous and irregular, hyper-vascular pattern appears penetrating to the central area of the tumor, which can be an indication of a malignant tumor (figure 6.9B). Additionally, malignant tumors often show a pulsatile blood flow because it is supplied by the hepatic artery. In contrast, a benign tumor will show a regular vascular structure with a steady regular blood flow. Therefore, continuous high-resolution contrast imaging, *i.e.*, a high temporal and spatial resolution, is of great diagnostic value in tumor imaging applications.

## 6.6 Release burst imaging

Release burst imaging is a novel contrast imaging approach that optimally employs the transient characteristic of UCA. It is based on a combination of multiple high frequency, broadband-detection pulses and a separate release burst. The detection pulses are used to survey the target before and after transient enhanced scattering, which is forced by the release burst. In this way, both processes, *i.e.*, imaging and transient enhanced scattering, can be optimized separately. Therefore, this method circumvents the need to sacrifice either contrast sensitivity or imaging resolution (chapter 4). The presence of the contrast agent is simply detected by correlating or subtracting the signal responses from the detection pulses. Because the time-interval between the two detection pulses is minimal (approximately 200–400 $\mu$s, depending on

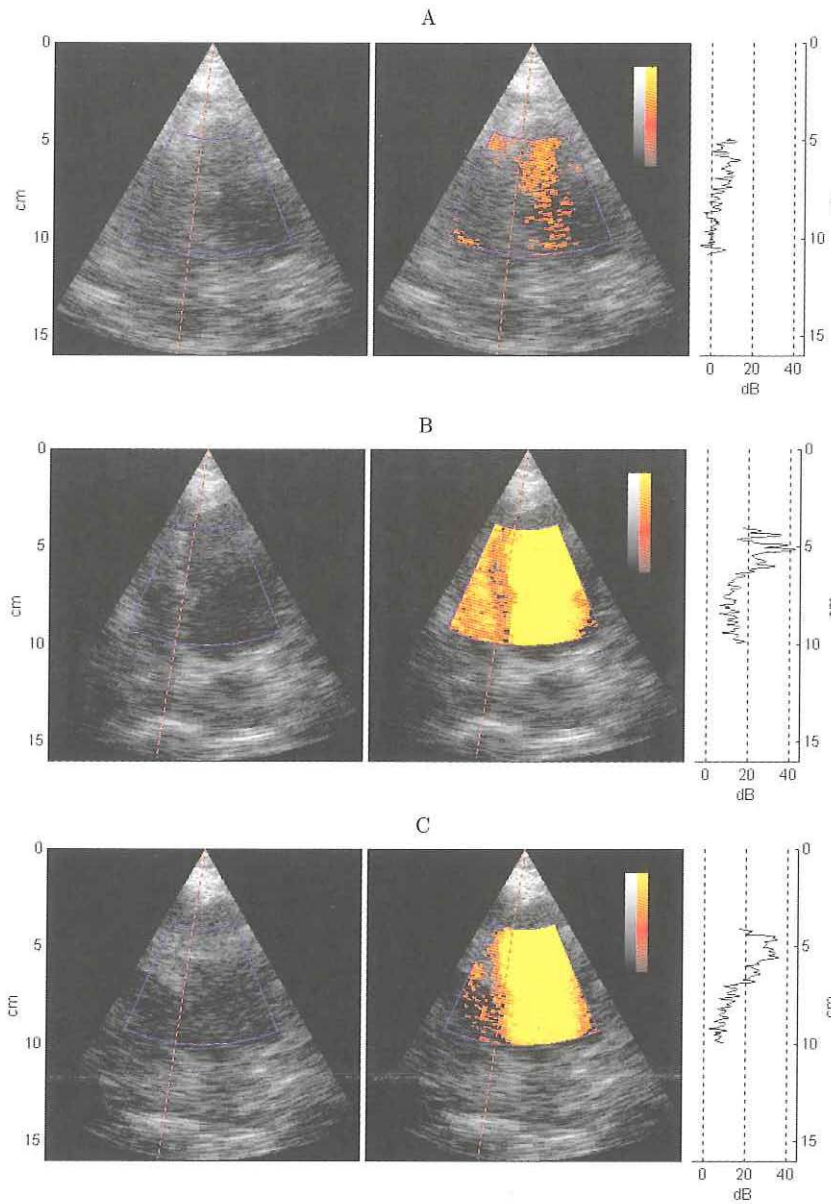


**Figure 6.10** *In vivo result of release burst imaging. Left panel: B-mode image with region of interest (ROI) for orientation. Middle panel: the processed release burst data is super imposed on the B-mode image. Right panel: power profile of the processed release burst data corresponding to the dashed red line in the left and middle panels. (A) Baseline recording without Levovist® and with release burst; (B) with Levovist® and with release burst; (C) with Levovist® and without release burst.*

the scan depth, size of the region etc.), the subtraction of the radio frequency (RF) data can be performed in real-time, and is less exposed to acquisition instabilities. In dynamic situations, this new method can be combined with a processing scheme to suppress clutter similar to those used in ultrasound Doppler (chapter 5).

In figure 6.10, the first experimental *in vivo* release burst images are presented. Digital RF data were recorded with a System Five ultrasound scanner (GE Vingmed Ultrasound, Horten, Norway) with a customized software version. All the data was processed and visualized off-line using Matlab® (The Mathworks Inc., Natick, USA). Triggered imaging was used at the end-diastolic phase of the heart cycle every third beat. Figure 6.10A shows the baseline recording before Levovist®was administered. The left panel shows the B-mode image for orientation with the 'release burst sector' or region of interest (ROI) indicated in blue. The quality of the B-mode image was suboptimal because the transmitted pulses were designed such that as little as possible of the contrast agent was disrupted by the B-mode scan. The middle panel shows the processed release burst data superimposed on the B-mode image. The right panel shows the power profile of the processed release burst data, corresponding to the cross-section as indicated by the dashed red line in the left and middle panels. Blooming artifacts may be excluded by using the additional information provided by the power profile. The baseline image shows that gain settings and clutter filtering were sufficient to suppress most of the motion of the myocardium. The remaining signals from the left ventricle cavity were due to high blood flow velocities.

During infusion of Levovist® (figure 6.10B), a clear opacification of the left ventricular (LV) cavity, and a part of the right ventricle (RV), was obtained. Especially at the interventricular septum (IVS), the LV cavity was clearly delineated. In this example, it is more emphasized because of the poor quality of the B-mode image. Additionally, an enhancement of the IVS was obtained, which is confirmed by the power profiles in figures A and B, and was approximately 10–15 dB.

Great care needs to be considered, however, to interpret the enhancement of the IVS as perfusion. Like with power Doppler, release burst imaging is a multi-pulse technique since a number of pulses are transmitted in a given line of sight. Therefore, motion artifacts originating from moving tissue can be interpreted as signals originating from contrast (flash artifact). However, a powerful utility of release burst imaging is that the release burst can instantaneously be switched on and off. The release burst modifies the UCA, which only occurs in a region where the contrast agent is present. Therefore, blooming and flash artifacts from clutter can be discriminated from real contrast enhanced signals. By displaying the images obtained in the release burst 'on' and 'off' mode simultaneously in a dual image mode, contrast rich areas can be accurately depicted. Figure 6.10C shows an example where the release burst was switched off, which is actually similar to power Doppler imaging at low MI. Indeed, the RV is less opacified and the IVS is hardly enhanced. The residual signals may be due to motion artifacts or contrast agent disruption by the detection pulses. The clear opacification of the LV is due to high blood flow and agent disruption.

The increased agent-to-tissue ratio for release burst imaging is clearly demonstrated in figure 6.10. It should be remarked, however, that the MI of the detection pulses was 0.4. At maximal MI, the agent-to-tissue ratio for harmonic power Doppler imaging obviously will

increase. Nevertheless, there are some limitations. Since a number of pulses are transmitted in a given line of sight, a high MI will result in a high disruption rate of the contrast agent. Decreasing the number of pulses has a lower limit because of clutter removal performances. Additionally, in harmonic power Doppler, the sample volume, *i.e.*, the length of the transmitted pulses, is generally increased to 3–5 cycles to get a more efficient disruption of the contrast agent (chapter 3). But this results in a degradation of the imaging resolution. Therefore, with harmonic power Doppler, a compromise between contrast sensitivity and imaging resolution has to be made. With release burst imaging, the release burst and imaging pulses are separated and, consequently, will be less susceptible for this trade-off.

Release burst imaging is very sensitive for UCA detection in fundamental mode and, therefore, nonlinear propagation effects do not limit the maximum obtainable agent-to-tissue ratio. However, due to the disruption of UCA, it has to operate in an intermittent way, like all imaging methods that rely on bubble disruption. In the intermittent mode, ultrasound imaging looses its real-time character, which can make it difficult to determine the position of the scanning plane. Nevertheless, a combination of continuous imaging and release burst imaging can be implemented. Real-time imaging can be displayed on one part of the monitor, while the information of contrast rich areas will be updated after every scan of release bursts and displayed on another part of the monitor, like with flash echo imaging[14].

## 6.7 Subharmonic imaging

The harmonic nature of oscillating gas bubbles has been exploited extensively with second harmonic imaging applications, like harmonic B-mode, harmonic power Doppler and pulse inversion. Nevertheless, new opportunities arise by exploiting the subharmonic component of an oscillating gas bubble. Under specific conditions, gas bubbles generate subharmonics, which occur at half the transmitted frequency. A potential advantage of subharmonic imaging is that, unlike with (second) harmonic imaging, the contribution of tissue is minimal at acoustic pressures currently used in diagnostic ultrasound, which will result in a high agent-to-tissue ratio[15]. Several investigators have described the possibility of subharmonic imaging for ultrasound contrast agents[15,16]. Recently, Shi et al.[17], described the implementation of subharmonic imaging in a ultrasound scanner and showed *in vivo* images.

According to theory, the onset of subharmonic scattering for a free gas bubble depends on the transmitted frequency and the applied acoustic pressure[18]. The acoustic pressure for the onset is minimal at twice the resonance frequency of the gas bubble. Additionally, narrow band signals are needed because the generated subharmonic components will be more dominant when the number of periods increase.

Figure 6.11 shows the scatter spectrum for SonoVue™ (Bracco Research S.A., Geneva, Switzerland). Apart from the transmitted (fundamental) and second harmonic components at 3.5 MHz and 7 MHz, respectively, the subharmonic and ultraharmonic components are clearly present at 1.75 MHz and 5.25 MHz, respectively. The measurement was not corrected for the sensitivity of the receiving transducer. Since the receiving transducer is less sensitive at the subharmonic component than at the second harmonic component, it can be expected that the corrected subharmonic component will be equal or higher than the second harmonic component.

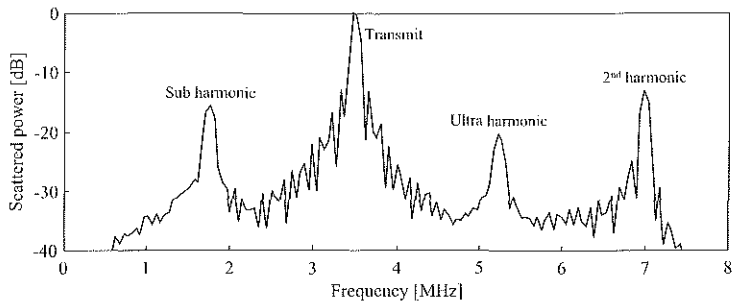


**Figure 6.11** *Scatter spectrum of SonoVue™, showing the fundamental, second harmonic, subharmonic and ultraharmonic components. The transmit burst had a frequency of 3.5 MHz, 40 cycles and a peak negative pressure of 75 kPa.*

The subharmonic signals in the received echoes can be extracted using filtering techniques like with second harmonic imaging. This gives subharmonic imaging a great potential. On the other hand, the narrow band character, necessary for optimal generation of subharmonics, will limit the imaging resolution.

The application of subharmonic imaging is currently at its infancy. The development of a new transducer design and imaging strategy will be essential to optimally exploit the advantages of subharmonic imaging.

## 6.8 Conclusions

Ultrasound contrast agents have unique signatures, which differ from surrounding tissue. Imaging methods like harmonic imaging, harmonic power Doppler imaging and pulse inversion imaging have improved the image quality of ultrasound contrast imaging considerably. New methods like release burst imaging and subharmonic imaging are being developed, and have to prove their additional value for ultrasound contrast imaging in the future. For further improvements of the current imaging methods and for the development of the new techniques, a complete understanding of the ultrasound-contrast agent interaction is essential. It is expected that new technical improvements will cause a further step forward in ultrasound contrast imaging. For example, specific machine settings and detection methods for different agents, *i.e.*, agent specific imaging templates, will probably be available on future ultrasound scanners.

# References

1. J. Ophir and K. J. Parker, "Contrast agents in diagnostic ultrasound," *Ultras Med Biol*, vol. 15, no. 4, pp. 319–33, 1989.

2. H. Medwin, "Counting bubbles acoustically: A review," *Ultrasonics*, no. 1, pp. 7–13, 1977.

3. N. de Jong, R. Cornet, and C. T. Lancée, "Higher harmonics of vibrating gas filled microspheres. Part one: Simulations," *Ultrasonics*, vol. 32, pp. 447–453, 1994.

4. J. G. Abbot, "Rationale and derivation of MI and TI: A review," *Ultras Med Biol*, vol. 25, no. 3, pp. 431 441, 1999.

5. T. R. Porter and F. Xie, "Transient myocardial contrast after initial exposure to diagnostic ultrasound pressures with minute doses of intravenously injected microbubbles. Demonstration and potential mechanisms," *Circulation*, vol. 92, no. 9, pp. 2391–2395, 1995.

6. A. Bouakaz, P. J. A. Frinking, and N. de Jong, "Ultrasound imaging based on nonlinear pressure field properties," in *15th Intern Symp Nonlin Acoust (ISNA)*, (Göttingen, Germany), 1999.

7. B. Ward, A. C. Baker, and V. F. Humphrey, "Nonlinear propagation applied to the improvement of resolution in diagnostic medical ultrasound," *J Acoust Soc Am*, vol. 101, no. 1, pp. 143–163, 1997.

8. J. D. Kasprzak, B. Paelinck, F. J. ten Cate, W. B. Vletter, N. de Jong, D. Poldermans, A. Elhendy, A. Bouakaz, and J. R. T. C. Roelandt, "Comparison of native and contrast-enhanced harmonic echocardiography for visualization of left ventricular endocardial border," *Am J Cardiol*, vol. 83, no. 2, pp. 211 217, 1999.

9. J. E. Powers, P. N. Burns, and J. Souquet, "Imaging instrumentation for ultrasound contrast agents," in *Advances in echo imaging using contrast enhancement* (N. Nanda, R. Schlief, and B. Goldberg, eds.), pp. 139–170, Dordrecht, The Netherlands: Kluwer Acedemic Publisher, 2nd ed., 1997.

10. K. Wei, A. R. Jayaweera, S. Firoozan, A. Linka, D. M. Skyba, and S. Kaul, "Quantification of myocardial blood flow with ultrasound-induced destruction of microbubbles administered as a constant venous infusion," *Circulation*, vol. 97, no. 5, pp. 473–483, 1998.

11. D. Hope Simpson, C. T. Chin, and P. N. Burns, "Pulse inversion Doppler: A new method for detecting nonlinear echoes from microbubble contrast agents," *IEEE Trans Ultrason Ferr Freq Con*, vol. 46, no. 2, pp. 372–382, 1999.

12. D. Hope Simpson, C. T. Chin, and P. N. Burns, "Perfusion imaging with pulse inversion Doppler and microbubble contrast agents: *In vivo* studies of the myocardium," in *IEEE Ultrason Symp*, vol. 2, (Sendai Japan), 1998.

13. F. Moriyasu, "*In vivo* behavior of microbubbles observed using harmonic grey-sacle imaging," in *4th Heart Centre Europ Symp Ultras Contrast Imaging*, (Rotterdam, The Netherlands), pp. 24–25, 1999.

14. N. Kamiyama, F. Moriyasu, Y. Mine, and Y. Goto, "Analysis of flash echo from contrast agent for designing optimal ultrasound diagnostic systems," *Ultras Med Biol*, vol. 25, no. 3, pp. 411–420, 1999.

15. P. M. Shankar, P. Dala Krishna, and V. L. Newhouse, "Advantages of subharmonic over second harmonic backscatter for contrast-to-tissue echo enhancement," *Ultras Med Biol*, vol. 24, no. 3, pp. 395–399, 1998.

16. O. Lotsberg, J. M. Hovem, and B. Aksum, "Experimental observation of subharmonic oscillations in infoson bubbles," *J Acoust Soc Am*, vol. 99, no. 3, pp. 1366–1369, 1996.

17. W. T. Shi, A. L. Forsberg F, Hall, R. Y. Chiao, J. Liu, S. Miller, K. E. Thomenius, M. A. Wheatley, and B. B. Goldberg, "Subharmonic imaging with contrast agents: Initial results," *Ultras Imag*, vol. 21, pp. 79–94, 1999.

18. A. Eller and H. G. Flynn, "Generation of subharmonics of order one-half by bubbles in a sound field," *J Acoust Soc Am*, vol. 46, no. 3 (II), pp. 722–727, 1969.

# CHAPTER 7

# Non-invasive pressure measurement in a fluid filled cavity


## Abstract

*A new method for non-invasive pressure measurement, based on the disappearance time of micron-sized free gas bubbles, is described in this chapter. An ultrasound contrast agent, consisting of encapsulated gas bubbles, was used as a vehicle to transport the free gas bubbles to the desired region where the pressure was measured. The small free gas bubbles were generated at the region of interest, from the encapsulated gas bubbles, which ruptured when they were exposed to a single low frequency (0.5 MHz), high acoustic amplitude ultrasound burst. The released gas bubbles persisted for only a few milliseconds and dissolved in the liquid, depending on their size, the gas, the liquid characteristics and ambient parameters like temperature, gas concentration and pressure. A pressure disappearance-time relationship was determined using a sequence of high frequency (10 MHz), low acoustic amplitude ultrasound pulses. From in vitro experiments, reproducible results show a significant difference between the disappearance time of the bubbles as a function of the local pressure, resulting in a quicker disappearance of the bubble for higher values of the local pressure. The sensitivity of the method to small pressure changes (50 mmHg) is demonstrated.*



Based on the publication: "Non-invasive measurement of the hydrostatic pressure in a fluid filled cavity based on the disappearance time of micron-sized free gas bubbles" by Ayache Bouakaz, Peter J.A. Frinking, Nico de Jong and Nicolaas Bom. *Ultrasound in Medicine and Biology, vol. 25, no. 9, pp. 1407–1415, 1999.*

## 7.1 Introduction

Blood pressure measurement in, for example, heart cavities and the peripheral vascular system, are important because they provide essential information concerning the state of health of this organ, and help the physician to determine the functional integrity of the cardiovascular system. Currently, pressure measurements are mainly performed by catheterization, consisting of a pressure-sensing catheter that is inserted into the heart chamber, or by Doppler echocardiography using the simplified Bernoulli equation[1]. The first method is accompanied by the disadvantages of creating pain and risk of infection. The second, non-invasive method does not provide reliable or reproducible blood pressure values[2]. Neither of the methods has found wide acceptance, and there are reports of substantial discrepancies between Doppler and catheterization measurements[3]. The complications involved and the conflicting results were the basis for the development of many alternative indirect non-invasive methods for blood pressure monitors. Most of the measuring techniques described in the literature are based on the interaction of ultrasound waves with individual gas bubbles. Due to the high compressibility of gas, the size of the gas bubble changes as a function of the local hydrostatic pressure. This change in size affects the acoustic characteristics of the gas bubble, such as resonance frequency, scattering and attenuation cross-section. Therefore, the pressure can be derived from these acoustic characteristics by injecting fluid-containing gas bubbles of uniform and known size into the organ in which the blood pressure is to be measured.

The majority of the techniques described in the literature concern the shift in resonance frequency as a function of the pressure variation[4,5,6,7]. These methods present, nevertheless, limitations, such as the sensitivity to measure small pressure variations. Also, these techniques were, at that time, limited because small stable microbubbles ($< 10$ $\mu$m) of uniform size were difficult to produce. Shankar et al.[8], however, suggested a double frequency technique as an accurate method for bubble size measurements. The change in bubble size is related to the change in hydrostatic pressure, and they showed that, with this method they were able to measure pressure differences ranging from 20 to 100 mmHg.

Hok[9] gave an extension of Fairbank's technique. Instead of using the bubble resonance frequency, he suggested using the echo amplitude from a single bubble. This is accomplished by means of modulation of the ambient pressure. Nevertheless, the main problem was to measure accurately the echo amplitude changes. Other factors that influence the accuracy are the magnitude of pressure changes (sensitivity) and the scattering from surrounding tissues (noise). The errors obtained in *in vitro* experiments exceeded 30%.

Miwa[10] proposed a different approach. Small gas bubbles were generated through cavitation by applying low-frequency ultrasonic waves. The generated gas bubbles were then detected by using high-frequency ultrasonic waves. The critical acoustic pressure for generating the gas bubbles is a function of the ambient pressure. However, the sensitivity of this method was low, especially for small pressure changes.

Recently, Shi et al.[11] showed that the amplitude of sub-harmonic signals generated by microbubbles, is strongly dependent on the local pressure, and suggested that this phenomenon can be used for non-invasive determination of the local pressure.

In this chapter, a novel method for non-invasive measurement of the hydrostatic pressure is proposed. The technique involves injection of shell-encapsulated gas bubbles into the circulatory

system. By transmitting a low-frequency, high-amplitude ultrasound burst, the encapsulated bubbles rupture and free gas bubbles are released (chapter 3) into the region where the local pressure is to be measured. The disappearance time of the released free gas bubbles is measured as a function of the local pressure by using a sequence of high-frequency, low-amplitude ultrasound pulses. Experiments and theoretical models validate this new method and the results are compared to methods employing the resonance frequency shift.

## 7.2 Bubble characteristics as a function of local pressure

### Bubble size

The scattering cross-section of a gas bubble is defined as the power scattered by the bubble divided by the incident acoustic intensity and, therefore, it expresses the scatter efficiency of the bubble. In ultrasound contrast imaging, this scatter efficiency is translated into the echogenicity of the contrast agent. Because the scattering cross-section is a function of the bubble radius, the echogenicity is likewise. *In vitro* and *in vivo* studies have demonstrated an accelerated shrinkage of microbubbles under increased local pressures[12,13]. As a result, contrast agents demonstarte a decrease of the reflectivity for local pressures similar to those produced within the heart chambers. The influence of the local pressure on the contrast echogenicity, after an intravenous injection of ultrasound contrast agents, has been reported in various papers[13,14,15].

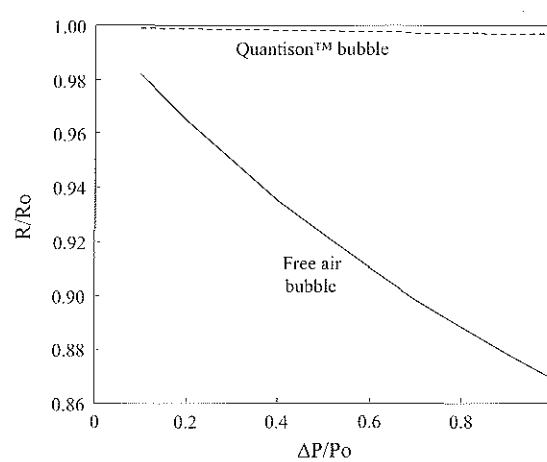


**Figure 7.1** *The relative radius of a 3-$\mu$m free-air bubble, ——, and a 3-$\mu$m Quantison™ bubble, -----, as a function of the relative change in local pressure.*

Bing et al.[16] and Bouakaz et al.[17] have given analytical expressions that demonstrate the change of bubble radius as a function of the local pressure. The solid line in figure 7.1 shows the radius of a 3-$\mu$m air bubble at different values of the local pressure. The results are presented

as the ratio of the radius to the initial radius, $R/R_o$, plotted against the ratio of the change in local pressure to the initial local pressure, $\Delta P/P_o$. The bubble shows a decrease of its size when the local pressure increases. According to Medwin[18], the difference in scattering cross-section is less than 1 dB for an air bubble with a diameter of 3 $\mu$m and a pressure difference of 200 mmHg. Therefore, non-invasive pressure measurement techniques based on the change in echogenicity, which is related to the scattering cross-section, are not very sensitive. For encapsulated gas bubbles, the effect of overpressure is even less. The dotted line in figure 7.1 represents the result for a 3-$\mu$m Quantison™ (Quadrant, Nottingham, UK) bubble, where a correction has been applied for the presence of the shell. Due to the shell, the Quantison™ bubbles are less compressible compared to free gas bubbles. For hydrostatic pressures up to twice the atmospheric pressure, the change in radius is less than 0.5%. Additionally, figure 7.2 shows the insensitivity of Quantison™ to overpressure, which makes it an excellent pressure-independent carrier for free gas bubbles.

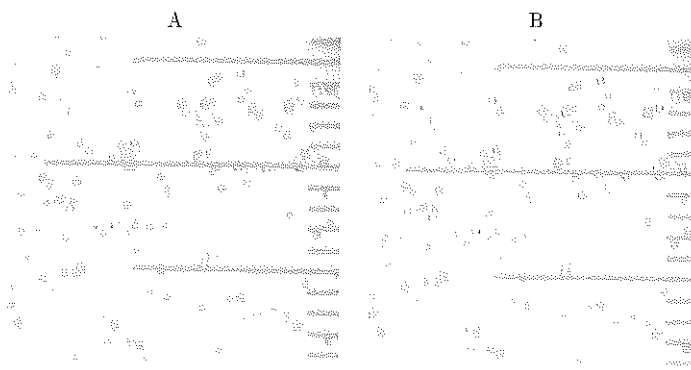


**Figure 7.2** *Microscopic view of diluted Quantison™ (magnification of 500×). Left panel: just before applying an overpressure of 100 mmHg, Right panel: 60 seconds after applying an overpressure of 100 mmHg.*

## Resonance frequency shift

de Jong et al.[19], have shown that for an ideal gas, at slow pressure and volume changes the resonance frequency of a gas bubble depends on the local pressure according to:

$$\frac{\Delta f}{f_r} = \frac{5}{6}\frac{\Delta P}{p_o}, \tag{7.1}$$

where

$\Delta f$ = frequency change
$f_r$ = resonance frequency
$\Delta P$ = pressure change
$p_o$ = ambient pressure.

From equation (7.1), it can be seen that the shift in resonance frequency due to a variation in pressure is linearly related to the relative pressure change. For an air bubble with a radius of 3 $\mu$m and an overpressure of 200 mmHg, the shift in resonance frequency is about 0.6 MHz. However, in practice, a distribution of bubbles is used resulting in a wide resonance peak. This will, in turn, decrease the resolution of the method. In addition, for encapsulated bubbles, a resonance peak is hardly detectable because of the increased stiffness of the microspheres caused by the presence of the shell. However, Hoff et al.[20] showed, by means of the attenuation spectra, that, for Sonazoid™(Nycomed Amersham, Oslo, Norway), which consists of particles containing perfluorcarbon gas encapsulated in a surfactant membrane, an increase in resonance frequency could be detected when the agent was exposed to a hydrostatic overpressure.

## Disappearance time of gaseous microbubbles

The disappearance time of gaseous microbubbles is mainly influenced by gas diffusion and surface tension. It has been demonstrated by Epstein and Plesset[21] and de Jong et al.[19] that spherical air bubbles with radii of 10 $\mu$m completely disappear in 6 seconds in gas-saturated water at room temperature and ambient pressure. The bubbles disappear through gas diffusion due to pressure elevation caused by surface tension.

To study the effect of overpressure on the disappearance time of gas bubbles, a differential equation, describing the change of bubble radius as a function of time, was derived. This equation is based on equation (13) of Epstein and Plesset[21] and equation (3.4) given in chapter 3:

$$\frac{dR}{dt} = DL \left( \frac{\frac{C_i}{C_o} - 1 - \frac{2\sigma}{Rp_o} - \frac{p_{ov}}{p_o}}{1 + \frac{4\sigma}{3Rp_o}} \right) \left( \frac{1}{R} + \frac{1}{\sqrt{\pi Dt}} \right), \tag{7.2}$$

where

$R$ = radius of the bubble
$t$ = time
$D$ = diffusion coefficient
$L$ = Ostwald coefficient
$\frac{C_i}{C_o}$ = ratio of the dissolved gas concentration to the saturation concentration
$\sigma$ = surface tension
$p_{ov}$ = overpressure.

This equation shows that the disappearance time of gas bubbles is related to the local pressure. Hence, the gas bubbles disappear more quickly when the medium is under pressure. For example, for an air bubble with a diameter of 3 $\mu$m, the disappearance time with and without an overpressure of 200 mmHg is 25.1 and 33.8 ms, respectively.

## 7.3 Method and materials

The principle of the current approach is to use encapsulated microspheres as vehicles for free gas bubbles. In this way, the gas bubbles are stabilized and are, therefore, protected against dissolution in the surrounding liquid during their transport. The release of the free gas bubbles is provoked by a low-frequency, high-amplitude ultrasound burst after they arrive in the desired region, which allows better control of the bubble characteristics. The variation in local pressure is deduced from the disappearance time of the released free gas bubbles, measured by the scattering responses of a sequence of high-frequency, low-amplitude pulses.

The scattering of encapsulated gas bubbles (Quantison™) at moderate and high acoustic pressures are described in detail in chapter 2 and 3, respectively. For acoustic pressures below a threshold, the bubbles act as encapsulated gas bubbles and are stable linear or nonlinear scatterers, depending on the applied acoustic pressure. For acoustic pressures above the threshold, the bubbles rupture and release the contained gas, subsequently acting as free gas bubbles. This explanation was investigated experimentally and evaluated by theoretical models. The results were: a 15–20 dB increase in scattering, the appearance of higher harmonics of the transmitted frequency and a finite duration of the effect. The finite duration is ascribed to the fact that the released free gas bubbles persist only for few milliseconds.

### Experimental setup and procedure

The experimental setup is illustrated in figure 7.3. A 0.5-MHz single-element transducer (Panametrics, Waltham, USA) focused at 75 mm, with an aperture of 37 mm, was mounted in a water tank. This low-frequency (LF) transducer was used to generate the free gas bubbles by transmitting a high-amplitude ultrasound burst (duration=10 $\mu$s; acoustic pressure=1.6 MPa).

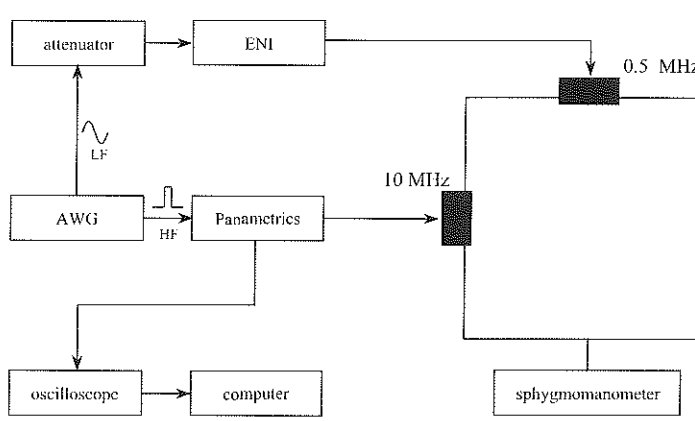


**Figure 7.3** *Block diagram of the instrumentation for producing the high acoustic amplitude low frequency (LF) burst and the low acoustic amplitude high frequency (HF) pulses.*

The peak negative acoustic pressures were measured with a calibrated hydrophone (PVDFZ44-0400, Specialty Engineering Associates, Soquel, USA). A sine wave burst, 5 cycles, was generated by an arbitrary waveform generator (LeCroy LW 420A, Chestnut Ridge, USA) and amplified by a 60-dB linear power amplifier (A-500, ENI, Rochester, USA). The amplitude was adjusted by a separate variable attenuator (355C/D, HP, Palo Alto, USA).

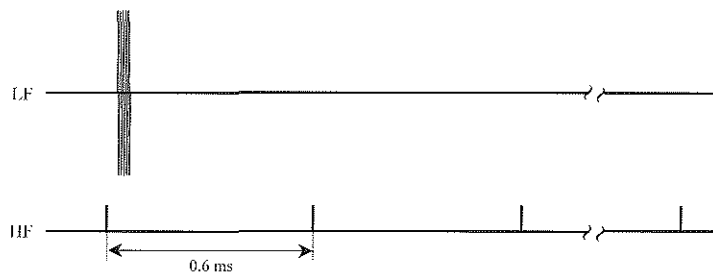


**Figure 7.4** *Diagram showing the synchronization of the LF and HF signals.*

The released gas bubbles were detected by a broad band (flat response within 3 dB between 1 and 10 MHz) single-element transducer, with a center frequency of 10MHz (Panametrics), that was mounted perpendicularly to the first transducer. The high-frequency (HF) transducer was focused at 75 mm and had an aperture of 12 mm. Short, single-cycle, low-amplitude ultrasound pulses (acoustic pressure of 100 kPa) were generated with a pulse-repetition interval (PRI) of 0.6 ms, to measure the evolution of the generated free gas bubbles over time. Figure 7.4 shows a schematic representation of the time synchronization of the HF pulses and LF burst. Note that the LF burst was switched on directly after the first HF pulse. The responses of the HF signals were received by a pulser/receiver (5052 PR, Panametrics) and could be amplified from −40 dB to +40 dB. The amplified signal responses were filtered to minimize noise and avoid aliasing and were digitized by a LeCroy 9400A (LeCroy) digital oscilloscope (100 MHz, 8 bits). The signal responses were recorded over a time window of 10 $\mu$s, were sampled at 50 MHz and transferred to a personal computer for further analysis. The final results were averaged over 30 measurements.

The experiments were conducted at room temperature. The water tank was positioned over a stirring device and was filled with Isoton® II (Coulter Electronics, Luton, UK), which was left standing overnight and, therefore, was air saturated. The ambient pressure was increased from 0 to 200 mmHg in steps of 50 mmHg by using a sphygmomanometer. Quantison™ was used at a dilution of 1/4500, which corresponds to $3.3\times10^5$ microspheres per ml. The mean diameter of Quantison™is 3.2 $\mu$m and less than 0.5% of the bubbles are larger than 6 $\mu$m. The size distribution is shown in figure 2.1

## 7.4 Results and discussion

### Free gas bubble release

Figure 7.5 illustrates the phenomenon of free gas bubble release from Quantison™ microspheres. The solid lines represent the measured scattering (= scattering cross-section per unit volume) of Quantison™, *i.e.*, before applying the LF burst. This curve shows the typical scatter spectrum for Quantison™ (chapter 2), which means that it shows no peak, and above 4 MHz, the scattering is independent of frequency. The dotted line shows the scattering directly after applying the LF burst, and represents the scatter spectrum of the released gas bubbles. The maximum around 3.8 MHz indicates the resonance frequency. From the two curves, an increase of 15 to 20 dB can be noticed for the scattering of the released gas bubbles compared to the scattering of Quantison™. This result is supported by simulating the scattering of free air bubbles (figure 7.6A), that is obtained from linear theory according to Medwin[18]. The best fit between theory and measurement is obtained by using the size distribution given in figure 7.6B, which has a mean diameter of 1.95 $\mu$m.

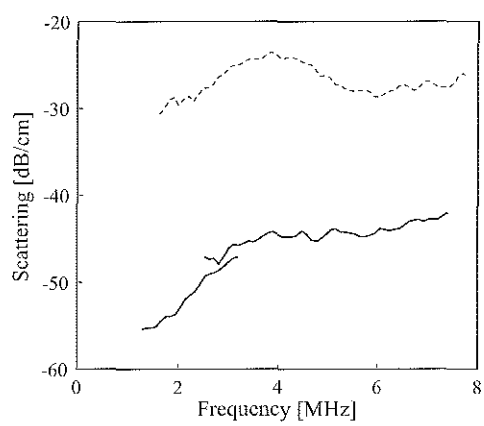


**Figure 7.5** *Scattering as a function of frequency for Quantison™ at ambient pressure. The solid line represents the scattering before the LF burst. The dotted line represents the scattering measured directly after the LF burst. The dilution used was 1/4500 ($3.3\times10^5$ microspheres per ml).*

### Resonance frequency shift

Figure 7.7, lines a and b, show the scattering of the generated gas bubbles at ambient pressure and at an overpressure of 200 mmHg, respectively. The simulated curves are plotted in the same figure, where a' corresponds to the situation at ambient pressure and b' corresponds to the situation at an overpressure of 200 mmHg. Two phenomena can be noticed, *viz.*, a decrease of the scattering and a shift of the resonance frequency towards a higher value. This is supported by the results shown in figure 7.1 that, for an increase of the local pressure, the bubble

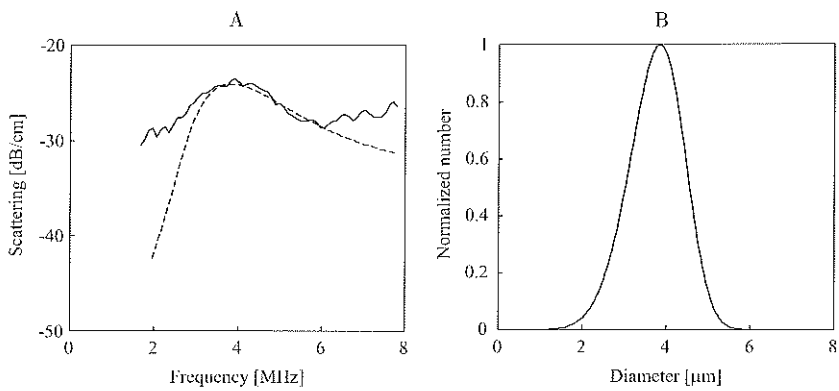


**Figure 7.6** *Scattering vs. frequency for the released gas bubbles. (A): Experiment (——) and simulation (-----). The size distribution (B) is obtained by fitting the theoretical spectrum to the measured spectrum.*

radius decreases. From the simulated results shown in figure 7.7, it can be concluded that an overpressure of 200 mmHg leads to a decrease of maximum of the scattering of 0.75 dB/cm and to a shift of the resonance frequency from 3.8 to 4.2 MHz (the resonance frequency is inversely related to the radius). However, a difference of 0.75 dB/cm in scattering is usually smaller than the variation of the measured scattering itself. Also, it may be difficult to accurately obtain small frequency shifts from the experimental results, especially for small changes of the hydrostatic pressure. Therefore, measurements of the hydrostatic pressure based on changes in scattering or frequency shifts are less sensitive.

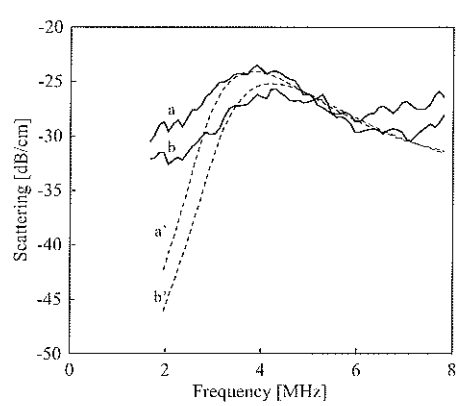


**Figure 7.7** *Scattering vs. frequency for the released free gas bubbles at ambient pressure (a and a') and at 200 mmHg overpressure (b and b'). The solid lines (a and b) show the measured spectra. The dotted lines (a' and b') show the simulated spectra.*

## Disappearance time of gaseous microbubbles

Figure 7.8A shows a sequential representation of the scattered signal responses from Quantison™ and from the released bubbles at ambient pressure. The first signal response is received from intact Quantison™ microspheres, *i.e.*, before transmitting the LF burst. After applying the LF burst, an increase of the scattered signal can be appreciated, in agreement with figure 7.5. The amplitude of the scattered signals decreases as a function of time. This is ascribed to the dissolution of the gas into the surrounding liquid that, eventually, leads to the disappearance of the released gas bubbles. The baseline scattering level, corresponding to the scattering of Quantison™, is reached in less than 30 ms, which is indicated as the disappearance time of the released gas bubbles. After applying an overpressure of 200 mmHg (figure 7.8B), a faster decrease of the amplitude of the scattered signals can be observed. This means that the free bubbles disappear more quickly. In this situation, the disappearance time of the released gas bubbles is 15 ms.

Figure 7.9A and B (solid lines) show the measured energy (mean ± STD) within each time trace of the recorded sequences as a function of time, at 0 mmHg and 200 mmHg overpressure, respectively. For an overpressure of 0 mmHg, the theoretical curve (dotted line in figure 7.9A) at

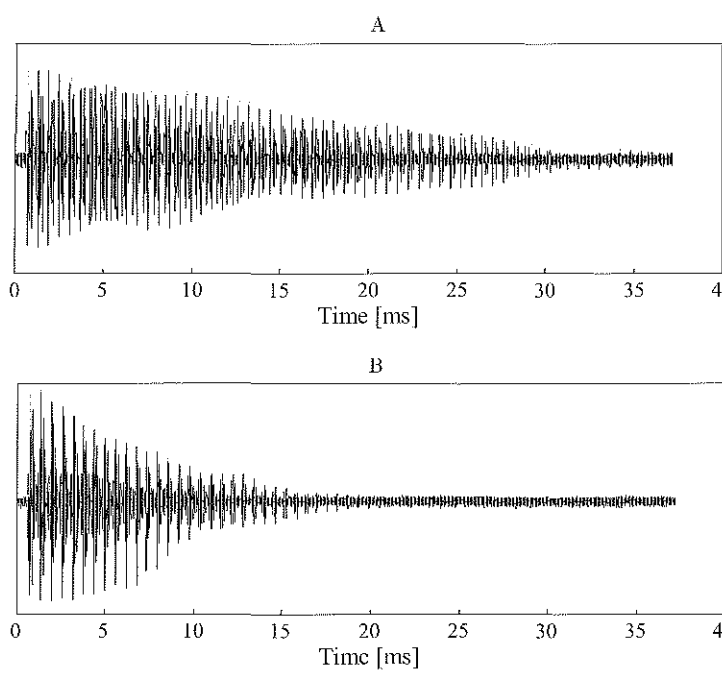


**Figure 7.8** *Sequential recording of the scattered signals as function of time at ambient pressure (A) and at 200 mmHg overpressure (B).*

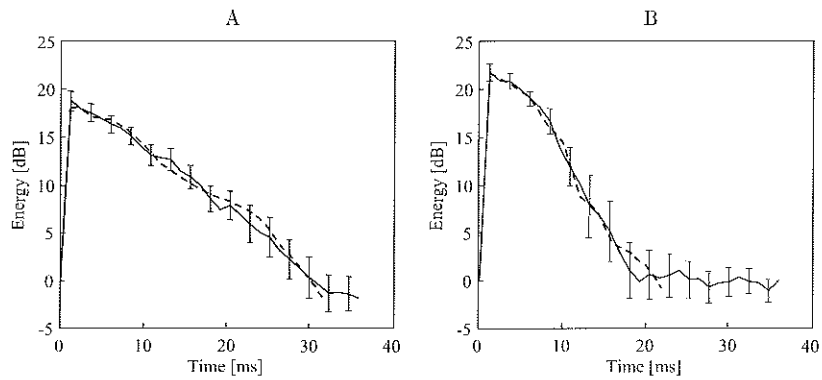


**Figure 7.9** *Scattered energy (mean ± STD) of the released air bubbles as a function of time at ambient pressure (A) and at 200 mmHg overpressure (B). The solid lines show the mean measured energy of 30 recordings. The dotted line represent the theoretical values obtained from linear theory.*

$t = 0$ s was calculated by using the size distribution shown in figure 7.6B. For an overpressure of 200 mmHg (dotted line in figure 7.9B), the initial size distribution was determined from figure 7.6B, where the radius was corrected for the overpressure according to figure 7.1. For both figures, the size distributions were recalculated after 0.6 ms by means of equation (7.2). The new size distributions were then used to calculate the scattering spectra at the corresponding time points according to Medwin[18]. The spectra include the theoretical linear scattering of Quantison™ (chapter 2). Finally, the energy was calculated at each time point by integrating the scattering over a frequency band ranging from 2 8 MHz. For both the theoretical and measured curves, the disappearance time, $t_{d,theory}$, and $t_{d,measure}$, were estimated from the 95% decay point in the energy-time curves.

Additionally, the disappearance time was calculated and measured at values for the overpressure of 50 and 100 mmHg. The mean value and standard deviation of a set of 30 sequential recordings are listed in table 7.1 (top row) and show a significant decrease of the disappearance time for increasing values of the overpressure. The bottom row of table 7.1 shows the corresponding theoretical values as obtained with equation (7.2), which are in close agreement with the measured values.

**Table 7.1** *Disappearance time as a function of the applied overpressure (0, 50, 100 and 200 mmHg). The top row shows the measured values (mean ± STD). The bottom row shows the theoretical values obtained from equation (7.2).*

| Overpressure [mmHg] | 0 | 50 | 100 | 200 |
|---|---|---|---|---|
| $t_{d,measure}$ [ms] | 28.8 ± 2.9 | 25.2 ± 3.2 | 22.2 ± 5.1 | 15.6 ± 3.2 |
| $t_{d,theory}$ [ms] | 30.1 | 24.5 | 21.4 | 15.5 |

### Final remarks

The indirect methods proposed in the literature for non-invasive pressure measurement present different limitations as a result of the insensitivity to measure small pressure changes. Indeed, when the variation of the pressure is small, the corresponding variation in the echo amplitude or resonance frequency is hard to detect from the scattered signals, as shown in this chapter. The new technique, as described in this chapter, is based on the analysis of the disappearance time of free gas bubbles as a function of the local pressure, and is sensitive for pressure differences of 50 mmHg. However, further improvement of the detection sensitivity is required to make the technique applicable, for example, for cardiac applications, where pressure differences smaller than 20 mmHg are important[22].

The size and number of the generated gas bubbles depend on the transmitted frequency and acoustic pressure, and can be controlled in *in vitro* situations. However, the technique described in this chapter is based on the disappearance time of released gas bubbles of known size. For *in vivo* situations, the transmitted frequency and acoustic pressure varies from patient to patient and for different locations in the human body and, consequently, the generated gas bubbles will vary in size and number, as well. Therefore, with the current technique, only variations of the local pressure can be measured. For absolute values of the local pressure, a calibration method needs to be developed.

It has been shown that the free gas bubbles can be generated using encapsulated gas bubbles and ultrasonic intensities available on the current diagnostic ultrasound scanners. Additionally, the method is easy to implement in current diagnostic ultrasound scanners. For example, the LF burst can be transmitted at the center frequency of the used transducer. The HF pulses can, subsequently, be transmitted at a frequency, say 40% higher than the center frequency. This way the acoustic pressure of the HF pulses will be approximately 50% of the acoustic pressure of the center frequency. To obtain larger frequency differences between the LF burst and HF pulse, a redesign of the transducer should be considered because of the limited bandwidth of current transducers. An alternative could be to divide the transducer into two parts with different types of acoustic elements. One part can be used for transmitting the LF burst and should preferably have a transmit frequency as low as possible. At lower frequencies, the estimated size of the released gas bubbles would be larger than at higher frequencies (chapter 3). Because larger bubbles are more susceptible to small pressure variations than small bubbles, the sensitivity would increase. The second part of the transducer could be used for transmitting the HF low-amplitude pulses.

## 7.5 Conclusions

In this chapter, a novel method has been described to measure internal cavity pressure from outside using free gaseous microbubbles as a pressure sensor. The free gas bubbles are delivered to the region of interest by using an ultrasound contrast agent, *i.e.*, encapsulated gas bubbles, as a vehicle. In this way, the gas bubbles are protected against dissolution by the surrounding shell. The free gas bubbles are then locally released from the contrast agent under the effect of a LF, high-amplitude ultrasound burst. The local pressure is estimated from the disappearance

time of the released free gas bubbles. Theory and experiments confirm the high reproducibility and sensitivity regarding the pressure-disappearance time relationship.

# References


1. C. Burton, *Physiology and biophysics of the circulation.* Chicago: Year Book, 2nd ed., 1972.

2. A. L. Strauss, F. J. Roth, and H. Rieger, "Non-invasive assessment of pressure gradients across iliac artery stenosis: Duplex and catheter correlative study," *J Ultras Med*, vol. 12, no. 1, pp. 17–22, 1993.

3. H. Baumgartner, H. Schima, G. Tulzer, and P. Kuhn, "Effect of stenosisgeometry on the Doppler-catheter gradient relation *in vitro*: A manifestation of pressure recovery," *J Am Coll Cardiol*, vol. 21, no. 4, pp. 1018–1025, 1993.

4. W. M. Fairbank and M. O. Scully, "A new non-invasive technique for cardiac pressure measurement: Resonant scattering of ultrasound from bubbles," *IEEE Trans Biomed Eng*, vol. 24, pp. 107–110, 1977.

5. E. G. Tickner, "Precision microbubbles for right site intracardiac pressure and flow measurements," in *Contrast echocardiography* (R. S. Melzter and J. R. T. C. Roelandt, eds.), vol. 15, pp. 313–324, London: Martinus Nijhoff, 1082.

6. K. Ishihara, A. Kitabatake, J. Tanouchi, K. Fujii, M. Uematsu, Y. Yoshida, T. Kamada, T. Tamura, K. Chihara, and K. Shirae, "New approach to non-invasive manometry based on pressure dependent resonant shift of elastic microcapsules in ultrasonic frequency characteristics," *Jap J App Phys*, vol. 27, no. Supp 27-1, pp. 125–127, 1988.

7. R. Schlief and H. Poland, *Ultrasonic manometry process in a fluid by means of microbubbles.* Patent nr.: US5195520, Mar 23 1993.

8. P. M. Shankar, J. Y. Chapelon, and V. L. Newhouse, "Fluid pressure measurement using microbubbles insonified by two frequencies," *Ultrasonics*, vol. 24, pp. 333–336, 1986.

9. B. Hök, "A new approach to non-invasive manometry: Interaction between ultrasound and bubbles," *Med Biol Eng Comp*, vol. 19, pp. 35–39, 1981.

10. H. Miwa, *Pressure measurement system with ultrasonic wave.* Patent nr.: US4483345, Nov 20 1984.

11. W. T. Shi, F. Forsberg, J. S. Raichlen, L. Needleman, and B. B. Goldberg, "Pressure dependence of subharmonic signals from contrast microbubbles," *Ultras Med Biol*, vol. 25, no. 2, pp. 275–283, 1999.

12. N. de Jong, F. J. ten Cate, W. B. Vletter, and J. R. T. C. Roelandt, "Quantification of transpulmonary echocontrast effects," *Ultras Med Biol*, vol. 19, no. 4, pp. 279–288, 1993.

13. N. de Jong and F. J. ten Cate, "New ultrasound contrast agents and technological innovations," *Ultrasonics*, vol. 34, no. 2-5, pp. 587–590, 1996.

14. J. S. Shapiro, S. A. Reisner, G. S. Lichtenberg, and R. S. Meltzer, "Intravenous contrast echocardiography with use of sonicated albumin in humans: Systolic disappearance of left ventricular contrast after transpulmonary transmission," *J Am Coll Cardiol*, vol. 7, pp. 1603–1607, 1990.

15. J. Mottley and E. C. Everbach, "Decay of ultrasonic integrated backscatter from saccharide contrast agent is accelerated by increased pressure," *Circulation*, vol. 82, pp. 139–140, 1990.

16. R. Bing and J. Katz, "The response of microscopic bubbles to sudden changes in the ambient pressure," *J Fluid Mech*, vol. 224, pp. 91–115, 1991.

17. A. Bouakaz, N. de Jong, C. Cachard, and K. Jouini, "On the effect of lung filtering and cardiac pressure on the standard properties of ultrasound contrast agent," *Ultrasonics*, vol. 36, no. 1-5, pp. 703–8, 1998.

18. H. Medwin, "Counting bubbles acoustically: A review," *Ultrasonics*, no. 1, pp. 7–13, 1977.

19. N. de Jong, F. J. ten Cate, C. T. Lancée, J. R. T. C. Roelandt, and N. Bom, "Principles and recent developments in ultrasound contrast agents," *Ultrasonics*, vol. 29, no. 4, pp. 324–330, 1991.

20. L. Hoff, P. C. Sontum, and J. M. Hovem, "Acoustic characteristics of Nycomed's NC100100 contrast agent," in *16$^{th}$ Intern Congr Acoustics and 135$^{th}$ Meeting Acoust Soc Am*, vol. 3, (Seattle, USA), pp. 1835–1836, 1998.

21. P. S. Epstein and M. S. Plesset, "On the stability of gas bubbles in liquid-gas solutions," *J Chemical Physics*, vol. 18, no. 11, pp. 1505–1509, 1950.

22. W. F. Ganong, *Review of medical physiology*. Los Altos: Lange Medical Publications, 4th ed., 1969.

# CHAPTER 8

# Ultrasound directed drug delivery: A preliminary study


## Abstract

*Currently, ultrasound is used in medical diagnostics and therapies. However, only recently it has been recognized as a method for external controlled delivery of drugs. Novel drug delivery systems have been described using microspheres comprising a therapeutic compound. Especially gas containing microspheres, used as ultrasound contrast agents in the medical diagnostic field, can be visualized during their transport in the human body using standard ultrasound imaging systems. Once the microspheres reach the site of interest, ultrasound can subsequently be applied in order to rupture the microspheres and release the therapeutic compound. Therefore, the release can be controlled externally once the microspheres reach a diseased region.*

*In this chapter, a brief literature overview is given on drug delivery and its combination with ultrasound. Additionally, preliminary measurements are described of the release of a model drug (Hexabrix) from a microspheric polymer carrier under ultrasound irradiation.*



Based on the publication: "Effect of ultrasound irradiation on the release of encapsulated drugs," by Peter J.A. Frinking, Ayache Bouakaz, Nico de Jong, Folkert J. ten Cate and Siobhan Keating. *Ultrasonics, vol. 36, no. 1–5, pp. 709–712, 1998.*

## 8.1 Introduction

For many years, the major focus of drug research has been on the synthesis or discovery of new drugs. While this continues to be important, the last few years attention is being paid on research aimed at creating new drug delivery systems. In the early days, sustained delivery was achieved by combining drugs with substances that decreased there solubility, *viz.*, coating them with materials that did not dissolve in stomach acid, compressing them in dense tablets or putting them into suspensions or emulsions. Although the drugs were effective for a longer period of time, the release kinetics were still strongly influenced by patient variations. To improve the delivery systems, new approaches have been developed like[1,2]:

- Drug modification by chemical means. A drug may be chemically modified to alter properties like biodistribution, pharmacokinetics, solubility or antigenicity.
- Drug entrapment within pumps or polymer materials that are placed into the desired bodily compartments. In these delivery systems, the release rate is almost exclusively controlled by the design of the polymer system or pumps.
- Drug entrapment in small vesicles that are injected into the bloodstream.

## 8.2 Controlled release systems

Controlled drug release systems provide several advantages over conventional drug therapies[1,2]. For instance, these systems maintain the drug in the desired therapeutic range. Hence, the need for follow-up care can be reduced, and the patient comfort can be increased. Moreover, the drugs can be administered locally to a particular region in the body and, lowering the systemic drug level.

Langer[1,2] described several ways to embed drugs into polymer materials, each depending on different release mechanisms, such as diffusion, chemical control or solvent activation. Diffusion may occur through a reservoir in which a drug core is surrounded by a polymer film, or in a matrix where the drug is uniformly distributed through the polymeric system. Chemical control is accomplished by polymer degradation or chemical cleavage of the drug from the polymer. Solvent activation involves swelling of the polymer or osmotic effects.

Polymer drug release systems provide a sustained release of drugs over a long period of time. However, these systems are unable to change the drug release on demand once it has started. Therefore, the drug release should be activated and controlled by external means. Different approaches have been proposed, such as magnetic fields, electric pulses and ultrasound irradiation[1,3,4]. The remainder of this chapter focuses on the approach using ultrasound to externally control the release of embedded drugs.

## 8.3 External drug control by ultrasound

Ultrasound has been used extensively for medical diagnostics and, to a certain extent, for medical therapy (physiotherapy, ultrasonic surgery, hyperthermia). Nevertheless, it has become

popular only recently as a technique to enhance drug release from drug delivery systems. A number of studies suggested to use ultrasound as an external mean of controlling the delivery of drugs. Some of them are mentioned below.

Transcutaneous drug delivery can be enhanced by means of ultrasound[5,6,7,8,9]. Since the skin represents a major barrier for delivering drugs, low frequency ultrasound (20 kHz to 1 MHz), has been used to increase the permeability of the skin. Although the exact mechanism, which is responsible for the enhanced drug delivery, is not clearly understood, the increase is explained by cavitation and heating.

Ultrasound combined with drug release from polymer systems have been tested in the field of cancer chemotherapy[10]. 5-fluorouracil (5-FU) was embedded in an ethylene-vinyl alcohol copolymer using both the reservoir and matrix system. Ultrasound at 1 MHz was used and caused an increase in release rate in both cases. The release returned back to baseline after the ultrasound irradiation was stopped. It was suggested that a temperature increase of the delivery system was the main cause of increased diffusion of the 5-FU from the polymer.

Kost et al.[11] investigated the effect of ultrasound on the degradation of polymers and the release rate of drugs incorporated in these polymers. An increase of polymer degradation and the release of the drugs were observed, and several mechanisms were mentioned to cause these effects. For example, the release rate increased as a function of the applied ultrasound intensity, and cavitation appeared to play a significant role, whereas temperature and mixing were relatively unimportant in effecting enhanced polymer degradation. Increased release rates were also observed when ultrasound was applied to biodegradable polymers implanted in rats.

## 8.4 Novel drug delivery systems

An optimal drug delivery system would be non-invasive, detectable from outside the body and should be able to target a diseased region. Furthermore, the release should be controllable by external means. Novel drug delivery systems have been described using microspheres comprising a therapeutic compound[12]. These systems can be administered intravenously or by using special drug delivery catheters[13,14]. Once the microspheres have reached a diseased region, the release of the therapeutic compound may be controlled by ultrasound[15,16]. Additionally, gas containing microspheres, used as ultrasound contrast agents, can be visualized during their transport in the human body using standard ultrasound imaging systems. Ishihara[17], for example, described a method for using 'micromachines', *i.e.*, gas-filled microspheres, as drug carriers to selectively administer the drug to a localized region. The 'micromachines' are introduced into the diseased region while they are observed with B-mode echo. Additionally, the microspheres are irradiated by ultrasound at the resonance frequency. In this way, ultrasound energy is absorbed most effectively and, consequently, the release of embedded drugs can be accelerated.

Unger[18], also described the use of gas-filled microspheres as delivery devices of drugs. The microspheres contain a therapeutic compound and a temperature activated gaseous precursor, which becomes a gas upon activation at a specific temperature (fluid-gas phase shift). After administering the microspheres into the human body, the microspheres are detectable for diagnostic ultrasound through the fluid-gas phase shift. They can be monitored in real time until they have reached the region of interest. Therapeutic ultrasound, *i.e.*, lower frequency and

higher intensity compared to diagnostic ultrasound, can then be applied to the region in order to rupture the microspheres and release the therapeutic compound. Several ways to incorporate the therapeutic compound within the microspheres were mentioned.

## 8.5 Experimental procedure and results

A preliminary experiment was carried out as a fundamental test of forced release of an encapsulated compound from a microspheric carrier by ultrasound. Small polymeric microspheres were produced by spray-drying a 50/50 Poly (DL Lactide-co-Glycolide) polymer. Hexabrix, a standard X-ray contrast agent, which is highly soluble in water, was used as a model drug. As a result of spray-drying, the microspheres were gas-filled, and the Hexabrix was embedded within the shell. The product obtained was a dry powder consisting of microspheres with a mean diameter of 2–3 $\mu$m (figure 8.1), and with a 5% loading of Hexabrix in the shell.

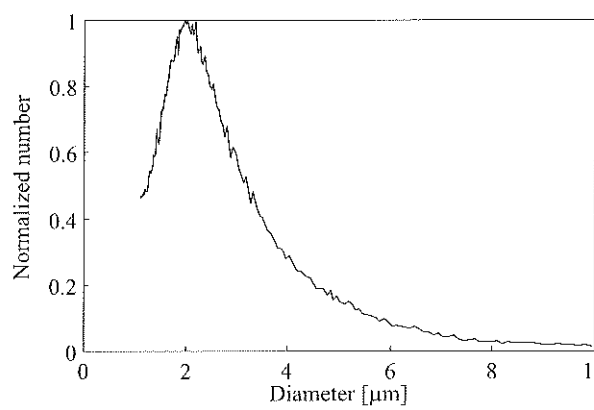


**Figure 8.1** *Normalized size distribution of the polymeric microspheres, with diameters ranging from 1.46 to 10 $\mu$m, as measured with the Coulter Counter® Multisizer II with an aperture of 70 $\mu$m employing 256 channels.*

Ultrasound images were acquired with a standard diagnostic ultrasound scanner (HP Sonos 1500, HP, USA) to determine if the microspheres could be detected. First, a baseline image was obtained (figure 8.2A) of 250 ml of Isoton® II (Coulter Electronics, Lutton, UK) in a beaker, which was positioned on a mechanical stirrer. Second, 27 mg of the microspheres was suspended in 5 ml Isoton®, gently inversed and added into the beaker. Again an ultrasound image was obtained, and a significant increase in echo response can be appreciated (figure 8.2B). The echo response had vanished after 15 minutes (figure 8.2C). Figure 8.2B demonstrates that the microspheres can be detected by ultrasound and, therefore, may be visualized during their transport in the body.

To measure the release of Hexabrix, 5.2 mg of the microspheres was suspended in phosphate buffered saline. At $t = 0$ minute, 1 ml of the sample was filtered through a 0.2 $\mu$m Sartorius RCI5 filter, and analyzed by a Beckman UV/VIS spectrophotometer, which was calibrated for

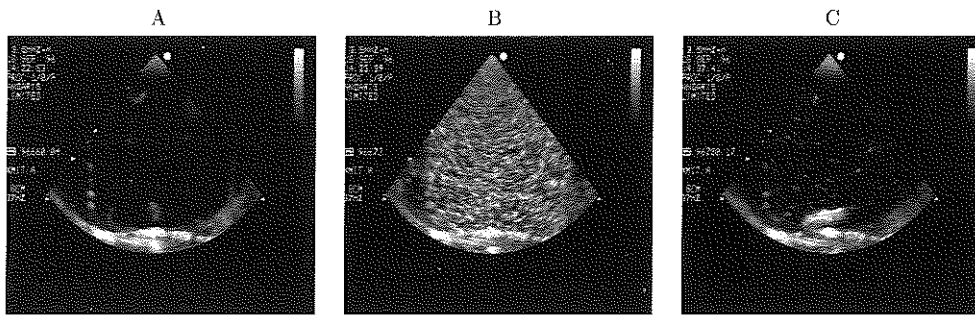


**Figure 8.2** *(A) Baseline echo image. (B) Echo response after addition of the polymeric microspheres. (C) Echo response 15 minutes after addition.*

Hexabrix at 243 nm using quartz cuvettes. At this wavelength, the absorbens of UV light is maximal for Hexabrix and does not overlap the maximal absorbens of the polymer material. Every 5 minutes, a new sample was analyzed up to 30 minutes. The product was left on a rollermixer and gently mixed during the experiment. The release was calculated by taking the theoretical loading of 5% into account, and is shown by the solid line in figure 8.3. After 30 minutes, only 30% of the Hexabrix was released from the microspheres. A similar experiment was conducted but now the product was irradiated by ultrasound for 10 minutes, at 3.5 MHz and maximum intensity, starting after 10 minutes. As appears by the dashed line in figure 8.3, there was a slight increase in release up to 40%, and the total release after 30 minutes was 45%. Additionally, the release without ultrasound (sustained release) was measured up to 140 minutes (not shown). The maximum measured release of Hexabrix from the microspheres did not exceed 35%.

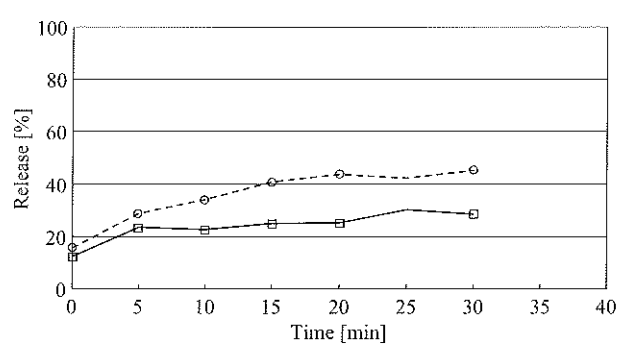


**Figure 8.3** *Percentage release of Hexabrix as a function of time. ——= sustained release, i.e., without ultrasound. ---- = release after ultrasound, after t=10 minutes.*

Next, a measurement was conducted in the same way as described previously but now the microspheres were put in a ultrasonic bath after 120 minutes and were irradiated for 1.5 minute at 35 kHz at maximum intensity. The sustained released of Hexabrix was 35% after 120 minutes. However, a significant increase in release, up to 100%, was measured after ultrasound was applied (figure 8.4).

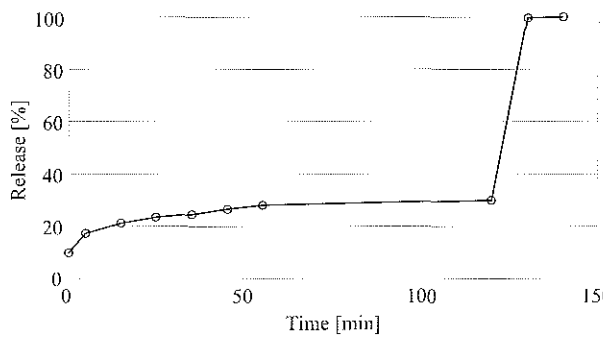


**Figure 8.4** *Percentage release of Hexabrix as a function of time with ultrasound for 1.5 minute, starting after 120 minutes.*

An offset of the released Hexabrix at $t = 0$ minute can be observed in figures 8.3 and 8.4, and was due to Hexabrix which was weakly bounded to the outer surface of the microspheres. Experiments to determine the actual loading subscribed this explanation[19] (actual loading of 90–95%). The degradation of the polymer material was not taken into account in the experiments.

## 8.6 Discussion and conclusions

Ultrasound is used in medical diagnostics and therapy. However, it has been recognized only recently as a method for external controlled delivery of drugs. The release rate of drugs from a carrier can be controlled depending on three predominant parameters: 1) carrier composition, 2) drug incorporation and 3) ultrasonic parameters. The physical characteristics of the drug carrier influence the release rate, depending on its degradation, rupture rate or temperature rise. It has been shown in this chapter that the release of a compound embedded in the shell of a microsphere can be controlled by ultrasound. Additionally, several studies have shown that the release rate is directly related to the ultrasound intensity, and that ultrasound has an effect on polymer degradation[5]. However, the exact underlying mechanism is not entirely understood yet. Other ultrasound parameters, such as frequency, duty cycle and duration may have an effect on the release rate and the local absorption of drugs.

Drugs can be coupled with a microsphere carrier in different ways. The drugs can be embedded in the microsphere, *i.e.*, within the gas containing lumen. However, placing a compound in the core of a microsphere changes the compressibility and, therefore, the acoustic behavior of a

microsphere. Moreover, it is difficult to produce this kind of delivery systems. An alternative is to embed the drug in the shell of the microsphere. In this way, the microsphere will maintain its acoustic properties, besides changed shell properties, and can easily be detected in the human body. Other methods consist of attaching or chemically linking the drugs to the outer surface of the shell. Also antibodies may be attached to the outer surface of the shell, which makes targeted delivery feasible, *i.e.*, delivery of embedded drugs to a specific site such as a tumor or a thrombus.

Specific research needs to be performed to fully understand the mechanisms involved in the release of an encapsulated compound from microspheric carriers. From the field of ultrasound contrast agents, knowledge and experience concerning the interaction of ultrasound and gas-filled microspheres is available. This expertise will be useful for developing ultrasound directed drug delivery systems.

# References

1. R. Langer, "New methods of drug delivery," *Science*, vol. 249, no. 4976, pp. 1527–1533, 1990.

2. R. Langer, "Novel drug delivery systems," *Chemistry in Britain*, pp. 232–236, 1990.

3. D. S. T. Hsieh, R. Langer, and J. Folkman, "Magnetic modulation of release of macromolecules from polymers," *Proc Natl Acad Sci USA*, vol. 78, no. 3, pp. 1863–1867, 1981.

4. M. R. Prausnitz, V. G. Bose, R. Langer, and J. C. Weaver, "Electroporation of mammalian skin: A mechanism to enhance transdermal drug delivery," *Proc Natl Acad Sci USA*, vol. 90, pp. 10504 10508, 1993.

5. J. Kost, "Ultrasound for controlled delivery of therapeutics," *Clinic Mat*, vol. 13, pp. 155–161, 1993.

6. J. Kost, "Ultrasound induced delivery of peptides," *J Control Rel*, vol. 24, pp. 247 255, 1993.

7. N. N. Byl, "The use of ultrasound as an enhancer for transcutaneous drug delivery: Phonophoresis," *Phys Ther*, vol. 75, no. 6, pp. 539–553, 1995.

8. S. Mitragotri, D. A. Edwards, B. Blankschtein, and R. Langer, "Mechanistic study of ultrasonically-enhanced transdermal drug delivery," *J Pharm Sc*, vol. 84, no. 6, pp. 697–706, 1995.

9. S. Mitragotri, B. Blankschtein, and R. Langer, "Ultrasound-mediated transdermal protein delivery," *Science*, vol. 269, no. 5225, pp. 850–853, 1995.

10. S. Miyazaki, W. M. Hou, and M. Takada, "Controlled drug release by ultrasound irradiation," *Chem Pharm Bull (Tokyo)*, vol. 33, no. 1, pp. 428–431, 1985.

11. J. Kost, K. Leong, and R. Langer, "Ultrasound-enhanced polymer degradation and release of incorporated substances," *Proc Natl Acad Sci USA*, vol. 86, no. 20, pp. 7663–7666, 1989.

12. R. L. Wilensky and K. L. March, "Microspheres," *Semin Interv Cardiol*, vol. 1, no. 1, pp. 48–50, 1996.

13. R. L. Wilensky, K. L. March, and D. R. Hathaway, "Direct intra-arterial wall injection of microparticles via a catheter: A potential drug delivery strategy following angioplasty," *Am Heart J*, vol. 122, no. 4 (I), pp. 1136–1140, 1991.

14. L. A. Guzman, V. Labhasetwar, C. Song, Y. Jang, A. M. Lincoff, R. Levy, and E. J. Topol, "Local intraluminal infusion of biodegradable polymeric nanoparticles: A novel approach for prolonged drug delivery after ballon angioplasty," *Circulation*, vol. 94, no. 6, pp. 1441–1448, 1996.

15. T. R. Porter, S. Li, K. Kilzer, J. Desjardins, and P. Iversen, "Enhanced delivery of antisense oligonucleotides when bound to intravenous perfluorcarbon-filled microbubbles: Effect of ultrasound and therapeutic implication (abstract)," in *2nd Thoraxcenter Europ Symp Ultras Contrast Imaging*, (Rotterdam), p. 25, 1997.

16. E. C. Unger, "Delivery applications of ultrasound contrast agents (abstract)," in *2nd Thoraxcenter European Symposium on Ultrasound Contrast Imaging*, (Rotterdam), pp. 54–56, 1997.

17. K. Ishihara, "Microrobotic drug delivery system: controlling drug release by resonant ultrasound," in *Proc Sec Int Micromach Symp*, pp. 69–75, 1996.

18. E. Unger, T. Fritz, T. Matsunaga, V. Ramaswami, D. Yellowhair, and G. Wu, *Therapeutic delivery systems related applications.* Patent nr.: US5542935, Aug 6 1996.

19. S. Keating, "Personal communication," 1997.

# CHAPTER 9

# Optical imaging of contrast agent microbubbles in an ultrasound field with a 100 MHz camera: A preliminary study


## Abstract

*Ultrasound contrast agents, used for medical diagnostic imaging, contain small microbubbles of a mean diameter of about 3 $\mu m$. The acoustic behavior of these bubbles in an ultrasound field has been subject to many investigations. In this chapter, a method is proposed to visualize the oscillation of the bubbles in a 0.5 MHz ultrasound field using a microscope and a high frame rate camera. For low acoustic pressures (peak negative pressure of 0.12 MPa), the radius-time curve as measured from the optical images, was in agreement with theory. For higher acoustic pressures (peak negative pressure of 0.6 MPa), the measured radius was significantly larger than predicted by theory, and a unexpected change in the bubbles shapes was observed. The proposed method enables the study and characterization of individual bubbles and their encapsulation. It is expected that this enables the development of new techniques for quality control, ultrasound contrast imaging and ultrasound-guided drug delivery.*



Based on the publication: "Optical imaging of contrast agent microbubbles in an ultrasound field with a 100 MHz camera," by Nico de Jong, Peter J.A. Frinking and Ayache Bouakaz. Accepted for publication in: *Ultrasound in Medicine and Biology, 1999.*

## 9.1 Introduction

Theoretical descriptions and mathematical modeling of a free gas bubble under ultrasound insonification has been subject to numerous studies over many years[1]. The behavior of a free gas bubble in an ultrasound field at low and moderate acoustic pressures is, therefore, well understood. Ultrasound contrast agents (UCA), used in medical diagnostic imaging, are generally based on free or shell-encapsulated gas bubbles. For encapsulated bubbles, the shell serves as a stabilizing goal, and thus, the microbubbles can circulate throughout the peripheral vasculature. However, the presence of the shell has a dominant effect on the acoustic properties such as linear, nonlinear and transient scattering of the microsphere[2,3] (chapter 3). Since current UCA detection methods are based on these acoustic properties, they are of crucial importance for the sensitivity of an ultrasound system in detecting the UCA in the presence of tissue. Consequently, a complete understanding of the ultrasound-contrast agent interaction is essential for improving the current and new imaging techniques, and for the development of new contrast agents. Since the stiffness of the microspheres can be controlled, e.g. by changing the material and thickness of the shell, contrast agent manufacturers are specifically interested in the effect of changing shell properties in order to produce an agent that optimally manifests specific acoustic signatures.

Acoustical measurements provide useful information about the interaction between ultrasound and the contrast agent. However, optical techniques may provide direct visual information. Such techniques have been described by Morgan[4] and Dayton[5]. In these studies, an undersampled reconstruction of an oscillating bubble was produced by stepping the delay of a laser pulse by an additional increment for each consecutive cycle until the entire oscillation period is recorded. The main limitation of this method is that a reproducible and stable phenomenon is a prerequisite. Therefore, bubbles destroyed within one or a few ultrasound cycles can not be investigated by this method.

In this chapter, a method is described to study the oscillations of single bubbles in a ultrasound field with a light microscope, in real time. The temporal resolution is sufficient to record the bubble oscillation within one acoustic cycle. Consequently, the complete bubble behavior during insonification can be recorded, and the onset of subharmonics and transient phenomena, for example, may be studied.

## 9.2 Materials and method

### Contrast agent

The contrast agent SonoVue™ (Bracco Research S.A., Geneva, Switzerland) was used in the experiments. SonoVue™ consists of sulfur hexafluoride gas bubbles encapsulated by a flexible phospholipid shell and has a mean diameter of 3 $\mu$m [6].

## Experimental setup

The experimental setup is illustrated in figure 9.1A. A gated sine wave burst (10 cycles) was generated by an arbitrary waveform generator (LW 420A, LeCroy, Chestnut Ridge, NY, USA), which was manually triggered. The signal was amplified by a 60-dB linear power amplifier (A-500, ENI, Rochester, USA), and the amplitude was adjusted by a separate variable attenuator (355C/D, HP, Palo Alto, CA, USA). In this way, the amplitude could be controlled between 10 kPa and 1 MPa. The peak negative pressures were measured at the site of interest with a calibrated hydrophone (PVDFZ44-0400, Specialty Engineering Associates, Soquel, USA). The amplified electrical signal was directed to a 0.5 MHz single element transducer (Panametrics, Waltham, MA, USA), which was focused at 75 mm and had an aperture of 37 mm. The transducer was mounted in a perspex block under an angle of 45 degrees relative to the top of the block. A synthetic Cuprophan® capillary fiber (Akzo Nobel Faser AG, Germany) with an inner diameter of approximately 180 $\mu$m was placed horizontally in the focus of the transducer. The contrast agent could freely flow through the fiber.

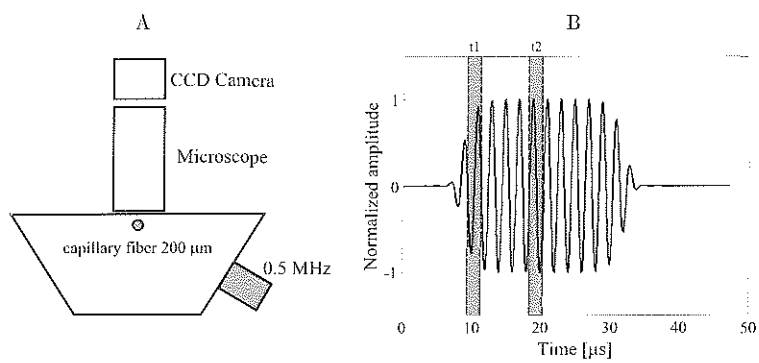


**Figure 9.1** *(A) Schematic set-up for the optical recordings. (B) Gated sine wave of 500 kHz. The shaded bars indicate the time intervals where the optical images were recorded.*

A microscope (BH2, Olympus Optical Co. GmbH, Hamburg, Germany) was positioned above the perspex block, and projected images of the contrast agent particles with a magnification of 100× on the fast framing camera (Imacon 468, DRS Hadland, UK). An optical beam splitter inside the camera projected the images on 8 separate Charge Coupled Devices (CCD, 576×385 elements). The camera was computer controlled, and the start and exposure time of each CCD was set independently. The shortest exposure time of the CCD's is 10 ns, which relates to a repetition frequency of 100 MHz. For most of the experiments, the exposure time and interframe time was 250 ns for all CCD's, which relates to a repetition frequency of 4 MHz. Consequently, the total recording of 8 images took 2 $\mu$s, which corresponds to one period of the 0.5 MHz transmitted ultrasound burst. A Short Arc Flashlamp (1100 series, EG&G, Scotland) with a duration of 2 $\mu$s and a peak intensity of 0.5 J was used for illumination. A separate standard CCD camera (FA851, Grundig Electronic, Fürth, Germany), with a frame

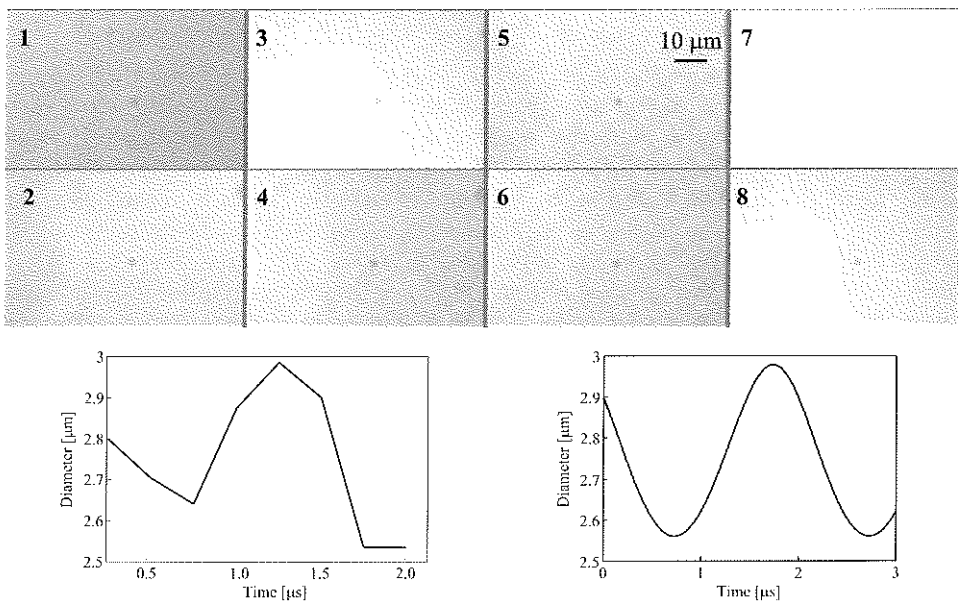


**Figure 9.2** *Optical images of a SonoVue™ microsphere. $P_-$=0.12 MPa. Exposure and inter frame time for all images was 250 ns. Bottom left: measured diameters for a SonoVue™ microsphere as a function of time. Bottom right: Calculated diameters as a function of time for a SonoVue™ microsphere.*

rate of 25 Hz and shutter time of 2 ms, was mounted on the microscope (not shown in figure 9.1A) at the same focal distance as the fast framing camera. In this way, the flowing agent could continuously be observed. The high framing camera and flashlamp were synchronised to the acoustical signal with an adjustable delay. The diameters of the recorded bubbles were estimated by thresholding and counting the number of pixels within the maximum cross-section of the projected area. Calibration was obtained by recording a 10-$\mu$m grid (Olympus).

## 9.3 Results

Figure 9.2 shows a sequential recording of SonoVue™ during 2 $\mu$s at a peak negative pressure ($P_-$) of 0.12 MPa (MI=0.16). The recording of the images started in the middle of the transmitted burst as shown by the dashed area (t2) in figure 9.1B. The 8 images show the oscillation of one SonoVue™ bubble as a function of time. The average brightness of the images is not uniform due to a variation in light intensity during exposure. The estimated mean diameter of the bubble was 2.75 $\mu$m, and the variation of the diameter ranged between 3 $\mu$m at maximum and 2.5 $\mu$m at minimum. Simulations were performed for an encapsulated gas bubble[2] with a resting diameter of 2.75 $\mu$m. The values for the shell parameters were based on measurements

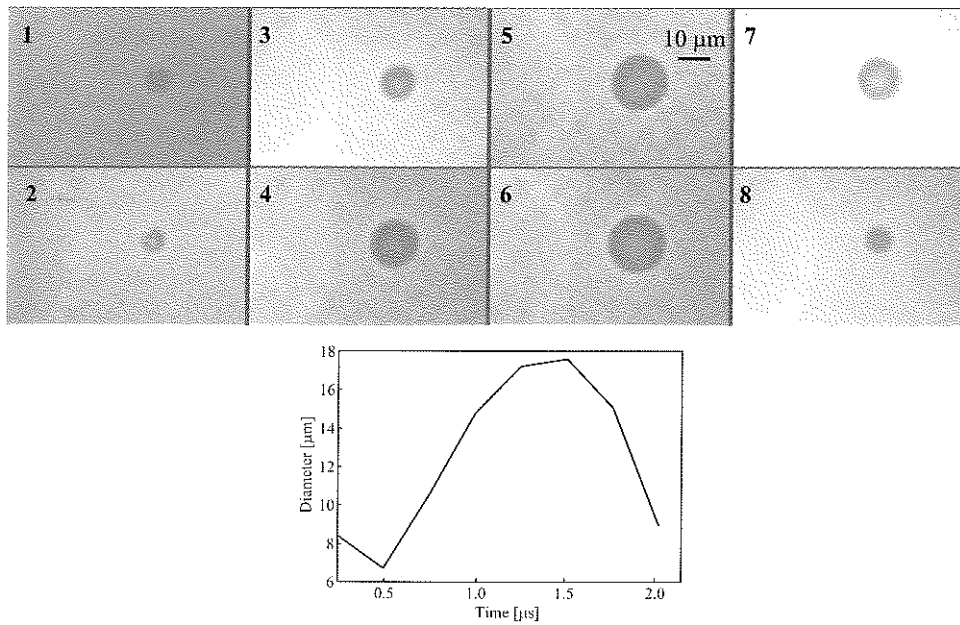


**Figure 9.3** *Optical images of a SonoVue™ microsphere. $P_-$=0.24 MPa. Exposure and inter frame time for all images was 250 ns. Bottom: measured diameters for a SonoVue™ microsphere as a function of time.*

reported by Gorce and Arditi[7], which were 0.44 MPa and 0.0038 Pa·s for the shell stiffness and shell viscosity, respectively. The exposure time of the camera was not included in the simulation, and the result is shown at the bottom of figure 9.2 (bottom right). Note the close agreement between the simulated and the measured results for this low acoustic pressure.

Figure 9.3 shows a sequential recording of a SonoVue™ microsphere insonified by an acoustic burst with a $P_-$ of 0.24 MPa (MI=0.32). The recording of the images started in the middle of the transmitted burst. The estimated mean diameter of the bubble was large, *i.e.*, about 12 $\mu$m.

Figure 9.4 shows 8 observations for a high acoustic pressure ($P_-$=0.6 MPa, MI=0.85), and the recording started in the middle of the transmitted burst. The images show a big diversity in bubble sizes. A cloud of bubbles can be observed containing small bubbles with an average diameter of 3.5 $\mu$m and one large bubble with a diameter of 12 $\mu$m. The time between images 7 and 8 was 2.75 $\mu$s. Although the relative diameter change of the small bubble **a** and the big bubble **b** shows the same variation, it seems that the larger bubble splits into two parts as can be noticed in image 8. The relative diameter change of the two bubbles is shown in the bottom of the figure and show the same course up to image 7.

Figure 9.5 shows the 8 observations also at an acoustic pressure ($P_-$=0.6 MPa, MI=0.85). Nevertheless, the recording of the images started at the beginning of the transmitted burst

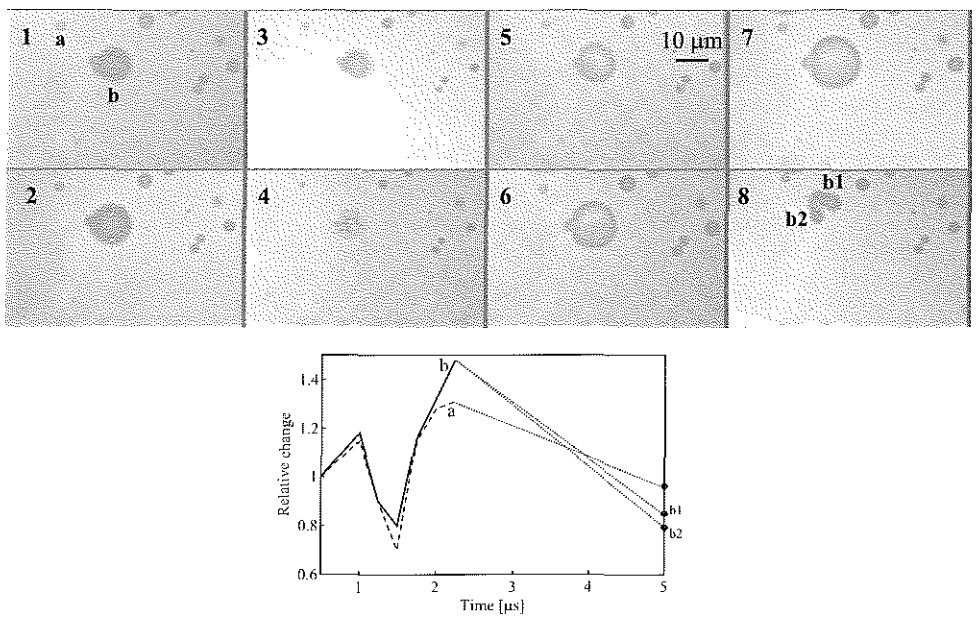


**Figure 9.4** *Optical images of SonoVue™ microspheres. $P_{-}$=0.24 MPa. Inter frame time of images 2–3 was 500 ns. Images 4–7 were recorded with an inter frame time of 250 ns. Inter frame time between image 7 and 8 was 2.75 µs. Exposure time for all images was 250 ns. Bottom: measured diameters for SonoVue™ microspheres as a function of time.*

(see figure 9.1B, t1), *i.e.*, the moment the ultrasound wave reached the ensemble of bubbles. In this experiment, the inter frame time of the first 2 images was set to 500 ns, and the rest of the images were recorded with an inter frame time of 250 ns, resulting in a total acquisition time of 2.5 µs. The exposure time of all the images was 250 ns. The first images show a minor change in diameter of the bubbles, however, the diameter increases dramatically in image 6, 7 and 8. The course of the change of diameter of 2 bubbles is given in the figure. The initial diameter of bubble **a** is 1 µm. It first decreases and then increases up to 7 µm. In this example, all the different bubbles show a similar behavior (see bubble **b**). The change in radius was underestimated by simulated results, which showed only an increase of 20–50% of the initial diameter.

## 9.4 Discussion and conclusions

During the exposure time (250 ns) the bubble continuously expands or contracts. Therefore, the motion of the bubble wall will be integrated and appears on the images as a dark ring (blurring). This is noticeable in figures 9.3 to 9.5. Nevertheless, the maximum diameter during

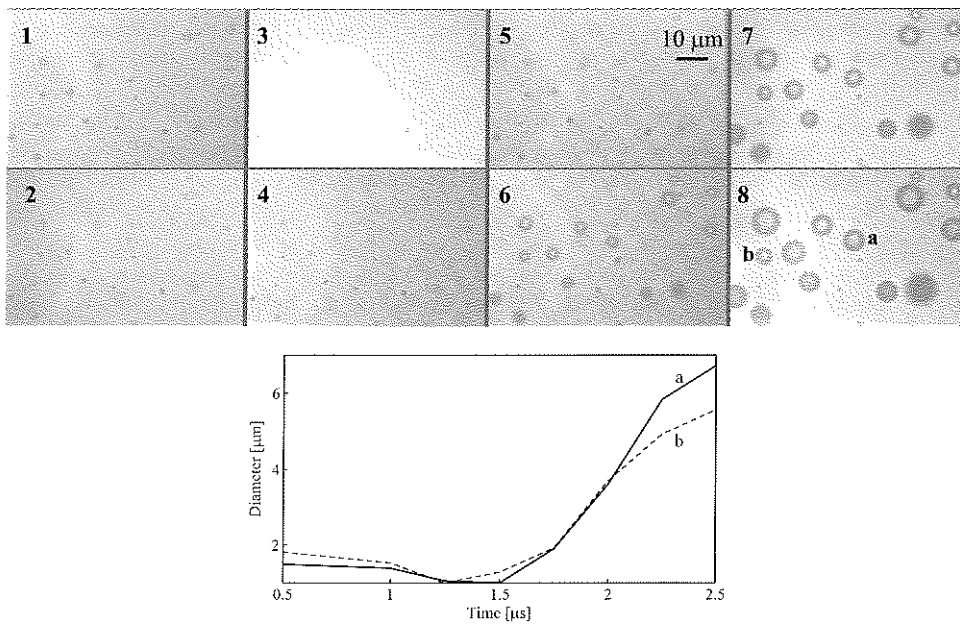


**Figure 9.5** *Optical images of SonoVue™ microspheres. P_=0.6 MPa. First image recorded at t=t1 (figure 9.1). Image 2 at t = t1 + 500 ns. Image 3 at t=t1+750 ns. Image 4 at t1+1000 ns. Image 5, 6, 7, 8 have an inter frame time of 250 ns. All images have an exposure time of 250 ns. Bottom: measured diameters for SonoVue™ microspheres as a function of time.*

exposure was considered for the analysis. In the simulations, this blurring effect was not taken into account.

The contrast agent was freely flowing through the capillary fiber during experiment. There was no need for fixation (e.g. with a pipette), which is necessary if stroboscopic investigation is considered[5] and, therefore, the experiment described in this chapter approaches the *in vivo* situation. Flow was low and exposure time short and, therefore, bubble displacement during experiment was negligible as can be seen in all the figures.

The optical observations of ultrasound contrast agents in an ultrasound field with a high frame rate camera as described in this chapter are the first reported. In other areas, e.g. cavitation or lithotripsy, the use of high frame rate camera has been reported[8]. However, big bubbles with a size of 100 $\mu$m and low frequencies of 100 kHz were used in these studies.

High frame rate recordings are essential for the development of different areas in which contrast agents can be used. First, this includes the development of detection methods. Some of the current methods are based on the change in scatter response of the bubble from successive pulses (chapter 3). For these methods, the exact response during insonification is not taken into account. The described optical observations show that the bubble diameter increases during

insonfication and exceeds the values expected from theory[3]. This opens ways to interrogate the bubble differently, and to use the acquired information directly without repeated interrogation. Also the optimal response as a function of frequency and acoustic amplitude can be determined.

Secondly, acoustic characterization always relates to a cloud of bubbles. The elasticity and the viscosity of the shell are derived from the acoustic measurements, and so they give only average values. Through real-time optical visualization, the exact contribution to the backscattered signal of each bubble can be determined and, consequently, the elasticity and viscosity of the shell of each bubble. Statistics can be carried out as a function of the diameter and new contrast agents can be rapidly evaluated and quality control is feasible.

A third aspect is the application of ultrasound directed drug delivery. Locally delivering the drugs under ultrasound irradiation has proven to be a new opportunity using contrast agent microspheres (chapter 8). With optical observation the exact mechanism behind the release can be studied.

# References

1. T. G. Leighton, *The acoustic bubble*. London: Academic Press, 1994.

2. N. de Jong and L. Hoff, "Ultrasound scattering properties of Albunex® microspheres," *Ultrasonics*, vol. 31, no. 3, pp. 175 181, 1993.

3. N. de Jong, R. Cornet, and C. T. Lancée, "Higher harmonics of vibrating gas filled microspheres. Part one: Simulations," *Ultrasonics*, vol. 32, pp. 447–453, 1994.

4. K. Morgan, P. Dayton, D. Kruse, A. Klibanov, G. Brandenburger, and K. Ferrara, "Changes in the echoes from ultrasonic contrast agents with imaging parameters," *IEEE Trans Ultrason Ferr Freq Con*, vol. 45, no. 6, pp. 1537–1547, 1998.

5. P. Dayton, K. Morgan, A. Klibanov, G. Brandenburger, and K. Ferrara, "Optical and acoustical observations of the effects of ultrasound on contrast agents," *IEEE Trans Ultrason Ferr Freq Con*, vol. 46, no. 1, pp. 220 232, 1999.

6. M. Schneider, M. Arditi, M. B. Barrau, J. Brochot, A. Broillet, R. Ventrone, and F. Yan, "BR1: A new ultrasonographic contrast agent based on sulfur hexafluoride-filled microbubbles," *Invest Radiol*, vol. 30, no. 8, pp. 451 457, 1995.

7. J. M. Gorce and M. Arditi, "Experimental and simulated acoustic properties of SonoVue™: Predited behavior in fundamental and harmonic imaging modes (abstract)," in *4th Heart Centre Europ Symp Ultra Contrast Imaging*, (Rotterdam), pp. 80–81, 1999.

8. T. Kodama and K. Takayama, "Dynamic behavior of bubbles during extracorporeal shockwave lithotripsy," *Ultras Med Biol*, vol. 24, no. 5, pp. 723 38, 1998.

# CHAPTER 10

# Summary and general discussion

## 10.1 Introduction

The application of ultrasound for clinical decision making has been expanded enormously during the last decades. Significant improvements in equipment have contributed to the understanding of anatomy and function of different organs. For instance, with the introduction of real-time two-dimensional imaging, it is possible to image different anatomical structures in the body non-invasively. Ultrasound can also be used for blood flow measurements in large vessels and the heart by using Doppler techniques. Nevertheless, for the assessment of perfusion of the myocardium or tumors for example, the scattering of blood is too low, *viz.*, approximately 30 40 dB lower than that of myocardial tissue[1,2]. By injecting an ultrasound contrast agent, the scattering of blood is enhanced. Thus additional information can be obtained, which can be combined with anatomy.

Diagnostic imaging modalities like magnetic resonance imaging (MRI) and computed tomography (CT) have shown great promise as a non-invasive technique by the use of a contrast agent. However, these techniques use ionizing radiation, are not repeatable and are relatively expensive. Diagnostic ultrasound imaging, on the other hand, does not use ionizing radiation, is repeatable and relatively cheap. Unfortunately, in comparison to MRI and CT, ultrasound contrast imaging has lagged behind, until recently, due to the lack of effective contrast agents, sensitive detection methods and the difficulties of quantifying ultrasound images.

Current contrast agents meet most of the criteria to make ultrasound contrast imaging an effective tool for clinical diagnosis. Therefore, contrast agents may prove great value in perfusion imaging of the myocardium and tumors. Additionally, some ultrasound manufacturers have recognized that contrast agents may significantly increase the diagnostic capabilities of ultrasound, and have developed contrast specific detection strategies.

The aim of the study reported in this thesis was to characterize ultrasound contrast agents, and to develop a contrast-specific detection strategy based on contrast-specific characteristics. In the following sections, the findings and results of each chapter will successively be summarized and discussed.

## 10.2 Acoustic characterization

Theoretical descriptions and mathematical modeling of a free gas bubble under ultrasound insonification has been the subject of numerous studies over many years[3]. The response of a free and encapsulated gas bubble to an ultrasound field at low and moderate acoustic pressures is well understood[4,5,6,7,8]. Chapter 2, reports on the results of the measured acoustic properties of encapsulated air bubbles, *viz.*, Quantison™ and Myomap™, at moderate acoustic pressures. An adapted version of the Rayleigh-Plesset equation, where the shell is described as a viscoelastic solid, was proposed and validated for these agents. The linear attenuation and scattering properties were predicted based on the measured size distribution. From the results presented in chapter 2, it can be concluded that the shell has a dominant effect on the linear and nonlinear scattering properties of encapsulated gas bubbles.

With previous reported models[6,7,8,9] it is not possible to calculate the acoustic properties of Quantison™ and Myomap™. These models were specifically developed for Albunex® and were

based on the assumption that the shell is much thinner than the bubble radius. For Albunex®, the shell thickness is approximately 15 nm [8], whereas for Quantison™, it ranges between 200 300 nm. Therefore, the thin shell assumption is not valid for agents such as Quantison™ and Myomap™, where the shell occupies a considerable part of the bubble volume. The fact that the transmission and scattering of Albunex® could be predicted with the model described in chapter 2, indicates that this model may be used for contrast agents with a thick or a thin shell. The scattering-to-attenuation ratio ($STAR$) may be used, in addition to the scattering or backscatter coefficient, to describe the scatter efficiency of ultrasound contrast agents. The $STAR$ can be used as a measure for the acoustic performance of a contrast agent. In this way, contrast agents could be compared to each other. However, the values for the $STAR$ are only valid for low acoustic pressures, and nonlinear effects are not taken into account.

Acoustic characterization, as described in chapter 2, is always related to a distribution of bubbles. Since the estimated shell parameters, such as the effective bulk modulus and friction parameter, are based on acoustic measurements, they represent average values and cannot directly be related to parameters for single bubbles. Additionally, the effective bulk modulus and friction parameter are derived from linear theory and are independent of the applied acoustic pressure. For high acoustic pressures, *i.e.*, in the nonlinear range, the shell material may loose its elastic characteristic. Thus, the material properties may change, and, accordingly, the acoustic properties may change.

The transient enhanced scattering phenomenon, shown by encapsulated types of contrast agents at high acoustic pressures, is of particular interest. This phenomenon cannot be predicted by the theoretical model that was introduced in chapter 2, and is described in chapter 3. It has been explained by a "dualistic" scattering characteristic of the bubbles, which is not shown by tissue, and, therefore, represents a unique signature of the contrast agent. For acoustic pressures below a threshold, the bubbles act as encapsulated gas bubbles. For acoustic pressures above the threshold, the bubbles rupture and release the contained gas, subsequently acting as free gas bubbles. The transient part of the effect is explained by the disappearance of the released gas due to diffusion in the surrounding liquid. These explanations were investigated experimentally and evaluated by theoretical models.

In comparison to free gas bubbles, encapsulated gas bubbles are robust and last in the circulation, but their scatter efficiency and nonlinear response are suboptimal. The scatter efficiency and nonlinear response of free gas microspheres, however, are far superior but their life span is limited to milliseconds. Therefore, ultrasound in combination with the "dualistic" scattering characteristic suggests that encapsulated gas bubbles can be construed as a robust vehicle for localized delivery of free gas bubbles, the 'ultimate' ultrasound contrast agent.

The explanation of free gas bubble release has been validated for Quantison™and has been described for other agents[10,11]. However, this explanation might be too simplistic or incomplete for the whole range of contrast agents available. Dayton and colleagues[12] have shown that a complex set of phenomena may affect the echoes from ultrasound contrast agents depending on the shell material and gas core. The changes reported include deformation or breakage of the encapsulating or stabilizing material, generation of free gas bubbles, reshaping or resizing of gas volumes including splitting of gas bubbles or fusion of bubbles into larger gas bubbles, or a combination of the aforementioned effects. Although the exact underlying mechanism for

contrast agent disruption may be very complex, the combination of the induced changes will alter the acoustic properties of the agent and can be detected by subjecting the contrast agent to ultrasound pulses.

## 10.3 Ultrasound contrast imaging

In chapter 4, a new ultrasound contrast imaging technique is proposed that exploits the use of the transient phenomenon, which was discussed previously. The general idea is to separate the agent disruption and the agent detection processes. This was performed in three steps. First, a low power pulse, *i.e.*, the detection pulse, was transmitted to obtain a reference signal. This pulse was chosen for optimal imaging and minimal contrast agent disruption. Secondly, a release burst was transmitted to disrupt or modify the contrast agent. Since the release burst is not used for imaging, it has no limitations concerning the number of cycles of the transmitted pulse. Furthermore, the frequency can be tuned without regard to reception sensitivity in the harmonic band. Finally, a second detection pulse was transmitted to detect the changes induced by the release burst. By comparing the scattering responses of the detection pulses before and after the release burst, a contrast specific signal was constructed. The method has been evaluated *in vitro* for three contrast agents, *viz.*, Quantison™, Levovist® and SonoVue™. An enhancement of the sensitivity of contrast agent detection compared to imaging methods without a release burst, was demonstrated.

The purpose of the release burst is to impose sufficient changes of the acoustic properties of the contrast agent that are uniform along the ultrasound beam. Considerations regarding imaging quality, such as pulse length and spatial resolution, are not required. Therefore, the release burst can be implemented as a single, high amplitude pulse of arbitrary length. Additionally, it can consist of a number of short pulses transmitted in succession with variable frequency, amplitude, length and focusing.

The contrast imaging approach described in chapter 4 is a multi-pulse technique, which means that multiple pulses are transmitted in a given line of sight. Consequently, it is susceptible to tissue motion, which can result in clutter signals that may be stronger than contrast-enhanced signals. Therefore, release burst imaging was combined with a Doppler based processing scheme to suppress the clutter signal (chapter 5). This implies that an ensemble of pulses was transmitted in the same direction, and that one of the pulses was replaced by a release burst. A clutter filter, based on polynomial prediction, was specifically developed for release burst imaging. The new method was evaluated against harmonic power Doppler (HPD) imaging. The sensitivity of the new method for contrast agent detection, expressed in terms of agent-to-tissue ratio (ATR), was higher than the ATR for 2 and 4-cycle HPD, for acoustic pressures up to 1 MPa. In general, the sensitivity of release burst imaging to contrast agent detection, in combination with its motion suppressing capabilities, was higher compared to HPD, for the contrast agents Quantison™, Levovist® and SonoVue™.

The clutter estimation was implemented by polynomial fitting. In appendix A, it is demonstrated that the polynomial prediction can be expressed as a linear operation on the observed samples, which can be expressed as a matrix multiplication. Moreover, the subtraction of the observed samples from the predicted samples can be incorporated in the same matrix. There-

fore, the complexity of the method is limited, and can efficiently be implemented on existing ultrasound scanners.

The transmit sequence for release burst imaging was implemented on the System Five ultrasound scanner (GE Vingmed Ultrasound, Horten, Norway), *i.e.*, the detection pulses and the release burst were transmitted by the same phased array transducer. An approach currently under investigation is a specialized phased array transducer with two different types of transducer elements arranged in an interleaved pattern. One type (e.g. the odd elements) will be used for transmitting the release burst, while the other type (e.g. the even elements) will be used for transmitting the detection pulses. The primary advantage of the proposed approach is that frequencies of the release burst and the detection pulses can be separated, *i.e.*, there will be hardly any overlap between the transmitted spectrum of pulses generated by the 'release' elements, and the transmit and receive spectrum of the pulses generated by the 'detection' elements. Thus, artifacts due to cross-talk (electrical and acoustical) can be minimized through bandpassed filtering. Also, in the current configuration one detection pulse is replaced by the release burst. This effectively increases the time delay between the detection pulses adjacent to the release burst, which may influence the clutter filter performance. Through separation of the release burst and the detection pulses, the time delay between the detection pulses adjacent to the release burst can be minimized, resulting in a better clutter estimation.

Release burst imaging has only been described as a technique for contrast agent detection, and not as a method for quantification. However, the information obtained with release burst imaging is based on real time subtraction where background tissue is suppressed from the contrast signal. Unlike video densitometry, the method is less susceptible to acquisition instabilities, and the full dynamic range of the contrast signal can be used. Additionally, there could be a linear relation between the contrast signal and the concentration of the contrast agent, which would make it ideal for contrast quantification.

In chapter 6, an overview is given of ultrasound contrast imaging methods that are currently available or under investigation. Imaging methods like harmonic B-mode imaging, harmonic power Doppler imaging and pulse inversion imaging have improved the image quality of ultrasound contrast imaging considerably. New methods like release burst imaging and subharmonic imaging are being developed and have to prove their additional value for ultrasound contrast imaging in the near future.

## 10.4 Non-imaging applications

Alternative non-invasive pressure measurements techniques, as described in literature, are based on the interaction of ultrasound waves with individual gas bubbles. Chapter 7, describes a novel technique for the non-invasive determination of the local pressure in a fluid filled cavity. The general idea was to use encapsulated gas bubbles as a 'vehicle' for free gas bubbles. The small free gas bubbles were released from the encapsulated gas bubbles by a release burst, and the disappearance time of the free gas bubbles was measured. From *in vitro* experiments, reproducible results showed a significant difference between the disappearance time of the bubbles as a function of the local pressure, resulting in a quicker disappearance of the bubbles for higher values of the local pressure. The sensitivity of the method to small pressure changes (50 mmHg)

was also demonstrated. Further improvement of the detection sensitivity is, however, required to utilize the technique in cardiology and radiology, where pressure differences are generally smaller than 20 mmHg.

A new potential technique for local drug treatment is 'ultrasound directed drug delivery' (UDDD). Therapeutic drugs can be incorporated or linked to microspheres, and can be released by ultrasound induced bubble rupture. Chapter 8, reports the results of a preliminary study of UDDD. It is shown that for a compound encapsulated in a polymeric shell, a significant increase in release could be obtained by ultrasound irradiation, which suggests that UDDD is feasable.

Although UDDD is at an early stage of research, the perspectives seem to be realistic. The first application of UDDD will probably be for sonothrombolysis[13], *i.e.*, blood clot or thrombus dissolution by ultrasound induced rupture of gas filled microspheres. Targeted thrombus-specific agents may be used to detect the blood clot. Selective binding mechanism through antibodies can be used for targeting[14]. Another interesting possibility is the adherence of albumin microspheres to inflammatory endothelium. This has been shown by Villanueva et al.[15], who reported that Albunex® bubbles preferentially adhere to inflammatory endothelial extracellular matrix. They suggested that albumin microspheres can be used to non-invasively study endothelial integrity, which may have implications for the assessment of preclinical atherosclerotic heart disease. Moreover, the detection of endothelial cell dysfunction in an early stage, might open a new potential in medicine for the treatment of endothelial cell dysfunction before thrombosis occurs[16].

Molecular binding mechanisms are only effective over distances on the order of nanometers. Therefore, effective targeting would be increased if the agent is concentrated near the specific site that has to be treated. Dayton et al.[17] have shown that primary and secondary radiation forces can be used to manipulate flowing contrast agents by ultrasound. Primary radiation forces may be used to direct bubbles to a specific region of the vessel wall where the flow velocity is lower. Bubbles can even be stopped in a flow by primary radiation forces at high acoustic pressure and high pulse repetition frequencies (PRF)[18]. Additionally, secondary radiation forces may be used to form aggregates of bubbles in the location to be treated.

## 10.5 Optical visualization and characterization

Acoustical measurements provide useful information about the interaction between ultrasound and the contrast agent. However, optical techniques may reveal direct visual information of the complete ultrasound-contrast agent interaction. This information could be used to explain phenomena that are not fully understood, such as bubble rupture. In chapter 9, a method is proposed to visualize the oscillation of the bubbles in a 0.5 MHz ultrasound field using a microscope and a high frame rate camera, at a frame rate of 4 MHz. For low acoustic pressures (peak negative pressure of 0.12 MPa), the radius-time curve as measured from the optical images was in agreement with theory[7]. For higher acoustic pressures (peak negative pressure of 0.6 MPa), the measured radius was significantly larger than predicted by theory, and a unexpected change in the bubbles shapes was observed. These results could provide additional information regarding single bubble behavior in an ultrasound field, which may be inconclusive

from acoustical measurements. The proposed method enables the study and characterization of individual bubbles and their encapsulation. Such a study is of crucial importance for developing new detection strategies, like subharmonic imaging, and to explore and develop new areas like ultrasound directed drug delivery.

## 10.6 General discussion

New contrast-specific detection strategies are continuously being developed and have resulted in improved ultrasound contrast agent detection. An established technique such as harmonic power Doppler imaging is known to be one of the most sensitive imaging modes currently available in terms of agent-to-tissue ratio. However, the information that is obtained with ultrasound contrast agents within the finest branch of the vascular system has not yet been fully utilized.

For optimal utilization of ultrasound contrast imaging, the most important issue is a solid education of current investigators, and more importantly, future clinical users. Ultrasound contrast imaging is still a research tool and appears to be a modality that has to be performed with dedication, persistence and patience. Numerous studies on the acoustical characteristics of gas bubbles have contributed to our knowledge of the behavior of contrast agents in an ultrasound field. However, a profound understanding of the bubble characteristics is necessary to find the optimal machine settings. Therefore, collaboration between physicists and physicians is mandatory to understand the fundamentals of the behavior of contrast agents in an ultrasound field, and to apply techniques based on novel contrast-specific characteristics in the clinical environment. Additionally, clinical studies involving contrast agents have to be made in a manner that includes correct interpretation of the measured imaging variables. This in order to obtain reliable physiological measurements, and not to bring ultrasound contrast imaging into disrepute. Without these considerations, the huge potential of ultrasound contrast imaging will be hard to recognize.

## 10.7 Conclusions

The results of the work reported in this thesis demonstrate that the scattering properties of encapsulated gas bubbles is highly dependent on the acoustic pressure amplitude. At high acoustic pressures, these properties are unique for contrast agents. Optimal utilization of the transient enhanced scattering phenomenon significantly improves the sensitivity of ultrasound contrast agent detection. Furthermore, it has been demonstrated in this thesis that new challenging applications like non-invasive pressure measurement and ultrasound drug delivery by means of encapsulated gas bubbles, are feasible. Finally, it has been demonstrated that radius-time curves of oscillating gas bubbles in an ultrasound field can be obtained, in real-time, with a light microscope and a high frame rate camera.

# References

1. K. K. Shung, R. A. Sigelmann, and J. M. Reid, "Scattering of ultrasound by blood," *IEEE Trans Biomed Eng*, vol. 23, no. 6, pp. 460–467, 1976.

2. J. G. Miller, J. E. Perez, and J. G. Mottley, "Myocardial tissue characterization: An approach based on quantative backscatter and attenuation," in *IEEE Ultrason Symp*, pp. 782–793, 1983.

3. T. G. Leighton, *The acoustic bubble*. London: Academic Press, 1994.

4. Lord Rayleigh (J. W. Strutt), "On the pressure developed in a liquid during the collapse of a spherical cavity," *Philos Mag*, vol. 34, pp. 94–98, 1917.

5. H. Medwin, "Counting bubbles acoustically: A review," *Ultrasonics*, no. 1, pp. 7–13, 1977.

6. N. de Jong and L. Hoff, "Ultrasound scattering properties of Albunex® microspheres," *Ultrasonics*, vol. 31, no. 3, pp. 175–181, 1993.

7. N. de Jong, R. Cornet, and C. T. Lancée, "Higher harmonics of vibrating gas filled microspheres. Part one: Simulations," *Ultrasonics*, vol. 32, pp. 447 453, 1994.

8. C. C. Church, "The effect of an elastic solid surface layer on the radial pulsations of gas bubbles," *J Acoust Soc Am*, vol. 97, no. 3, pp. 1510–1521, 1995.

9. N. de Jong, L. Hoff, T. Skotland, and N. Bom, "Absorption and scatter of encapsulated gas filled microspheres: Theoretical considerations and some measurements," *Ultrasonics*, vol. 30, no. 2, pp. 95–103, 1992.

10. V. Uhlendorf and C. Hoffmann, "Nonlinear acoustical response of coated microbubbles in diagnostic ultrasound," in *IEEE Ultrason Symp*, vol. 3, (Cannes, France), pp. 1559 1562, 1994.

11. Y. Takeuchi, "Industrial use of thermoplastic micro-balloon to mimic the contrast agents and its *in vitro* behaviour including increased gas dynamics," in *IEEE Ultrason Symp*, vol. 2, (Toronto, Canada), pp. 1579–1582, 1997.

12. P. A. Dayton, K. A. Morgan, A. L. Klibanov, G. H. Brandenburger, and K. W. Ferrara, "Optical and acoustical observations of the effects of ultrasound on contrast agents," *IEEE Trans Ultrason Ferr Freq Con*, vol. 46, no. 1, pp. 220–232, 1999.

13. E. C. Unger, T. P. McCreery, Y. Wu, D. Shen, G. L. Wu, A. Santanen, and V. Caldwell, "How far from clinical use? Ultrasound directed drug delivery in clinical radiology," in *3rd Heart Centre Europ Symp Ultrasound Contrast Imaging*, (Rotterdam, The Netherlands), pp. 64–65, 1998.

14. F. S. Villanueva, R. J. Jankowski, S. Klibanov, M. L. Pina, S. M. Alber, S. C. Watkins, G. H. Brandenburger, and W. R. Wagner, "Microbubbles targeted to intercellular adhesion molecule-1 bind to activated coronary artery endothelial cells," *Circulation*, vol. 98, no. 1, pp. 1–5, 1998.

15. F. S. Villanueva, R. J. Jankowski, C. Manaugh, and W. R. Wagner, "Albumin microbubble adherence to human coronary endothelium: Implications for assessment of endothelium function using myocardial contast echocardiography," *J Am Coll Cardiol*, vol. 30, no. 3, pp. 689–693, 1997.

16. E. C. Unger, E. Gertz, T. P. McCreery, D. Shen, G. L. Wu, Y. Wu, and R. Sweitz, "Visualization of intravascular thrombosis: Practical implications," in *4th Heart Centre Europ Symp Ultrasound Contrast Imaging*, (Rotterdam, The Netherlands), pp. 37–43, 1999.

17. P. A. Dayton, K. A. Morgan, A. L. Klibanov, G. H. Brandenburger, K. Nightingale, and K. W. Ferrara, "A preliminary evaluation of the effects of primary and secondary radiation forces on acoustic contrast agents," *IEEE Trans Ultrason Ferr Freq Con*, vol. 44, no. 6, pp. 1264–1277, 1997.

18. P. A. Dayton, A. L. Klibanov, G. H. Brandenburger, and K. W. Ferrara, "Acoustic radiation force *in vivo*: A mechanism to assist targeting of microbubbles," *Ultras Med Biol*, vol. 25, no. 8, pp. 1195–1201, 1999.

# APPENDIX A

# Matrix implementation of polynomial regression filtering for release burst imaging

The clutter filtering operation, as applied in chapter 5, can be expressed as a linear operation on the observed samples. The signal vector $\vec{x}$ denotes the vector of observed complex demodulated samples from the same direction and depth, taken at time points defined by the vector $\vec{t}$. The signal and time vectors are split into samples before the release burst ($\vec{x}_1$ and $\vec{t}_1$) and samples after the release burst ($\vec{x}_2$ and $\vec{t}_2$). Fitting an $N^{th}$ order polynomial to the samples before the release burst, then becomes finding the coefficients $a_0$, $a_1$, ... $a_N$ which best fits the polynomial:

$$p(t) = a_0 + a_1 t + \cdots + a_N t^N = \sum_{n=0}^{N} a_n t^n \tag{A.1}$$

to the observed samples $\vec{x}_1$ taken at $\vec{t}_1$. The problem can be formulated as a vector equation:

$$a_0[\vec{t}_1]^0 + a_1[\vec{t}_1]^1 + \cdots + a_N[\vec{t}_1]^N = \vec{x}_1, \tag{A.2}$$

where $[\vec{t}_1]^n$ denote column vectors found by taking each element of the time vector $\vec{t}_1$ to the power of $n$. If the number of time samples in $\vec{x}_1$ is greater than $N + 1$, the system of equations (A.2) becomes inconsistent, and the solution must be approximated. Equation (A.2) can be rewritten into a matrix notation where the matrix $T_1$ and the coefficient vector $\vec{a}$ can

Based on the manuscript: "Three-stage approach to ultrasound contrast detection" by Johan Kirkhorn, Peter J.A. Frinking, Nico de Jong and Hans Torp. To be submitted.

be defined as:

$$\underbrace{\begin{bmatrix}[\vec{t}_1]^0 & [\vec{t}_1]^1 & \cdots & [\vec{t}_1]^N\end{bmatrix}}_{T_1}\underbrace{\begin{bmatrix}a_0\\a_1\\\vdots\\a_N\end{bmatrix}}_{\vec{a}} = \vec{x}_1. \tag{A.3}$$

To solve with respect to $\vec{a}$, equation (A.3) is multiplied by the transpose of $T_1$:

$$T_1^T T_1 \vec{a} = T_1^T \vec{x}_1. \tag{A.4}$$

Since the columns of $T_1$ are linearly independent, the matrix $T_1^T T_1$ is invertible, and an expression for $\vec{a}$ can be obtained:

$$\vec{a} = (T_1^T T_1)^{-1} T_1^T \vec{x}_1. \tag{A.5}$$

This is a *Least-Squares* solution to the problem, giving the polynomial coefficients of equation (A.1). An expression for the predicted samples $\hat{\vec{x}}_2$ after the release burst is then given by:

$$\begin{aligned}\hat{\vec{x}}_2 &= a_0[\vec{t}_2]^0 + a_1[\vec{t}_2]^1 + \cdots + a_N[\vec{t}_2]^N = \underbrace{\begin{bmatrix}[\vec{t}_2]^0 & [\vec{t}_2]^1 & \cdots & [\vec{t}_2]^N\end{bmatrix}}_{T_2}\vec{a}\\ &= \underbrace{T_2(T_1^T T_1)^{-1}T_1^T}_{B}\vec{x}_1.\end{aligned} \tag{A.6}$$

The signal vector $\vec{y}$ is the difference between the predicted samples, $\hat{\vec{x}}_2$, and the observed samples, $\vec{x}_2$, after the release burst:

$$\vec{y} = \vec{x}_2 - \hat{\vec{x}}_2 = \vec{x}_2 - B\vec{x}_1. \tag{A.7}$$

More generally, it can be expressed as a linear filtering operation on the entire signal vector:

$$\vec{y} = \underbrace{\begin{bmatrix} -B & | & I \end{bmatrix}}_{A}\underbrace{\begin{bmatrix}\vec{x}_1\\\vec{x}_2\end{bmatrix}}_{\vec{x}} = A\vec{x} \tag{A.8}$$

The elements of the matrix $A$ are real valued, and only depend on the polynomial order $N$ and the time vectors $\vec{t}_1$ and $\vec{t}_2$. The power of the signal vector $\vec{y}$ can be found as:

$$||\vec{y}||^2 = \vec{y}^*\vec{y} = \vec{x}^* A^T A \vec{x}, \tag{A.9}$$

where $\vec{x}^*$ denotes the conjugate transpose of $\vec{x}$.

# Samenvatting

De doorbloeding (zuurstofvoorziening) van organen zoals de hartspier, lever en nieren, geeft informatie over het functioneren van deze organen. Ultrageluids contrastmiddelen maken het mogelijk om de doorbloeding van deze organen op een eenvoudige manier te bepalen met behulp van echografie. In dit proefschrift zijn de akoestische eigenschappen en toepassingen van ultrageluids contrastmiddelen onderzocht.

In hoofdstuk 2 worden akoestische eigenschappen zoals verzwakking en scattering (verstrooiing) van het contrastmiddel Quantison™ beschreven. Dit contrastmiddel bestaat, zoals de meeste contrastmiddelen, uit ingekapselde gasbellen met een gemiddelde diameter van ongeveer 3 $\mu$m. Een model, speciaal ontwikkeld voor dit contrastmiddel, is getoetst aan de hand van metingen. De resultaten laten zien dat voor niet al te hoge waarden van de akoestische druk ($<$ 200 kPa) de akoestische eigenschappen aanzienlijk verschillen van die van vrije luchtbellen binnen een frequentie bereik van 1–10 MHz.

Bij akoestische drukken boven een bepaalde waarde ($>$ 200 kPa), treedt er een tijdelijke verandering op in de scattering van Quantison™. In hoofdstuk 3 wordt dit effect gemeten en verklaard aan de hand van een "dualistisch" karakter van het contrastmiddel. Voor lage akoestische drukken gedraagt het contrastmiddel zich als ingekapselde gasbellen. Deze worden daardoor waargenomen als stabiele scatteraars. Bij hoge akoestische drukken komt het ingekapselde gas vrij en het contrastmiddel gedraagt zich als vrije luchtbellen. De toename in scattering, die op kan lopen tot 10–20 dB, en het niet-lineair scatteren wordt verklaard aan de hand van het efficiënte scatter gedrag van vrije luchtbellen. Het tijdelijke karakter van de vrijgemaakte gasbellen, die een diameter hebben van enkele micrometers, wordt verklaard door de beperkte levensduur van deze gasbellen in een vloeistof ($<$ 20 ms). De metingen worden ondersteund door bestaande theoretische modellen. De combinatie van ultrageluid en dit "dualistische" karakter van ultrageluids contrastmiddelen, maakt het mogelijk om het contrastmiddel op een unieke wijze te detecteren.

In hoofdstuk 4 wordt een nieuwe detectiemethode geïntroduceerd, die optimaal gebruik maakt van het "dualistische" scattergedrag van ingekapselde gasbellen. Hierdoor is het mogelijk om het contrastmiddel, en daardoor het bloed, op een unieke wijze te detecteren. Kort achter elkaar worden twee ultrageluidpulsjes uitgezonden; dit zijn de zogenaamde detectiepulsjes. Een derde puls zorgt voor het veranderen van het scattergedrag en wordt tussen de twee detectiepulsjes uitgezonden. Op deze manier wordt de detectie van het contrastmiddel en het genereren van het veranderde scattergedrag van elkaar gescheiden. Hierdoor kunnen deze processen onafhankelijk van elkaar geoptimaliseerd worden. Dit in tegenstelling tot de detectiemethoden die op dit moment klinisch worden toegepast. Door de echoresponsies van

beide detectiepulsjes met elkaar te vergelijken, en ervan uitgaande dat het omliggende weefsel in de tussentijd niet veranderd, wordt er een signaal gegenereerd dat specifiek is voor het contrastmiddel. In hoofdstuk 5 wordt de methode uitgebreid, zodat deze ook toegepast kan worden in situaties waarbij beweging als gevolg van ademhaling of het kloppen van het hart problemen kan opleveren voor een eenduidige detectie van het contrastmiddel. Een speciale filtertechniek wordt beschreven, waarmee gecompenseerd kan worden voor het bewegende weefsel. De methode is getest voor verschillende contrastmiddelen (Quantison™, Levovist® en SonoVue™) en levert zowel in een stilstaande als in een bewegende omgeving resultaten op die vergelijkbaar of beter zijn dan resultaten verkregen met de huidige toegepaste detectiemethoden. Naar verwachting zal met behulp van een speciale transducent de voorgestelde methode aanzienlijk beter presteren dan de huidige methoden. Deze methoden worden uitvoerige beschreven in hoofdstuk 6, en de beperkingen van ieder methode worden genoemd en geïllustreerd aan de hand van voorbeelden. Tevens worden de eerste *in vivo* resultaten van de nieuwe detectiemethode, zoals voorgesteld in dit proefschrift, gepresenteerd.

Nieuwe toepassingen voor ingekapselde gasbellen in combinatie met ultrageluid worden beschreven in hoofdstuk 7 en 8. Deze betreffen het niet-invasief bepalen van de omgevingsdruk in een met vloeistof gevulde ruimte en het lokaal toedienen van medicijnen met behulp van ultrageluid. Beide methoden zijn gebaseerd op het "dualistische" scattergedrag zoals beschreven in hoofdstuk 3. Voor de niet-invasieve drukmeting wordt met behulp van ultrageluid de verdwijntijd gemeten van de vrijgemaakte gasbellen. Aan de hand van *in vitro* experimenten wordt aangetoond dat er een significant verschil is tussen de verdwijntijden bij verschillende waarden van de omgevingsdruk, resulterend in een snellere verdwijntijd voor een hogere druk. De methode is geschikt om drukverschillen van ongeveer 50 mmHg waar te nemen.

Tevens is het mogelijk om de ingekapselde gasbellen te gebruiken als dragers voor medicijnen. Met behulp van ultrageluid kunnen de bellen enerzijds worden waargenomen in het menselijk lichaam, en anderzijds is het mogelijk om onder invloed van ultrageluid de medicijnen op een gecontroleerde manier vrij te maken. Een van de grote voordelen van deze techniek is dat de concentratie aan medicijnen in het lichaam laag is, met als gevolg dat schadelijke bijeffecten beperkt en gecontroleerd kunnen worden. Hoofdstuk 8 laat zien dat het mogelijk is om een stof opgesloten in de schil van een bel vrij te maken met behulp van ultrageluid.

Tenslotte worden in hoofdstuk 9 microscoop opnamen beschreven van individuele SonoVue™ bellen onder invloed van ultrageluid. Door gebruik te maken van een snelle camera is het mogelijk om real-time het trillen van de bel te registreren. Voor lage akoestische drukken is er een overeenkomst tussen de radius-tijd curve, afgeleid uit de optische opnames, en de radius-tijd curve volgens theorie. Voor hoge akoestische drukken verschillen theorie en metingen significant. Dergelijke opnamen leveren belangrijke informatie op over de interactie tussen contrastbellen en het ultrageluid. Dit is essentieel voor de ontwikkeling van nieuwe detectiestrategieën, en voor de ontwikkeling van technieken zoals 'ultrasound directed drug delivery'.

Concluderend kan worden gesteld dat ultrageluids contrastmiddelen de toepassingen van medisch ultrageluid aanzienlijk zullen uitbreiden. Vooral het meten van de doorbloeding/zuurstofvoorziening van de hartspier (of andere organen) zal met behulp van ultrageluids contrastmiddelen een enorme uitbreiding en vereenvoudiging betekenen voor de klinische diagnostiek.

# Dankwoord

Tijdens mijn studie Technische Natuurkunde aan de TU Delft was het gebruikelijk om voor een tentamenperiode te studeren in de bibliotheek van het Hoboken complex van de Erasmus Universiteit in Rotterdam. Door de regelmatige tripjes naar de 24ste verdieping van dit complex werd ik gegrepen door het uitzonderlijke uitzicht. Het was dan ook geen moeilijke beslissing om de AIO positie op het Laboratorium voor Experimentele Echocardiografie te accepteren, welke zich bevindt op de 23ste etage van ditzelfde complex, met als schitterend uitzicht 'de Kop van Zuid'.

Het eerste bezoek aan het lab staat me nog helder voor de geest, vooral de eerste ontmoeting met Nico de Jong. Nico, het enthousiasme waarmee jij iemand kan vertellen over je werk is uitzonderlijk. Daarbij is je gedrevenheid en enorme kennis op het gebied van ultrageluids contrastmiddelen en ultrageluidtechnieken in het algemeen, voor mij een unieke gelegenheid geweest om in dit wereldje mijn plaats te vinden. Ik beschouw het dan ook als een grote eer dat we de afgelopen 5 jaar samen gewerkt hebben. Tevens wil ik Folkert ten Cate, een van de pioniers op het gebied van ultrageluids contrastmiddelen, bedanken voor zijn steun en samenwerking. Folkert, helaas zijn alle wilde ideeën wat betreft 'ultrasound directed drug delivery' nog niet uitgekomen zoals we ons voorgesteld hadden. Desondanks denk ik dat je ook hierin zal volharden en een belangrijke rol zal gaan spelen.

This thesis carries the name of one person, however, it would have never been in its current form without the help and contribution of many people. In particular, I would like to thank Ayache Bouakaz, Ignacio Céspedes and Johan Kirkhorn.

Ayache, we have been working closely together since I started in the lab. This has resulted in a significant contribution in the thesis from your part. I enjoyed all the discussions, and besides a slight French accent, I even start to notice a small Dutch accent (achtentachtig scheerschuim prachtig).

Ignacio, your skill in generating new ideas has been of crucial importance for the development of the multi-pulse method. You have urged me to writing and taught me how to write a solid scientific paper. It was always a surprise how a manuscript would look after your corrections.

Johan, your input has been important for the development of the release burst imaging modality. Your knowledge of the GE Vingmed System Five scanner and programming skills have contributed to the implementation of the release burst method so that it could be tested *in vivo*. Although you sometimes call your programs 'quick and dirty hack versions', they were always of great help and value for analyzing data (by the way, I lost count of how many Kwak I have promised you).

Writing a thesis in a language that is not your native language demands some persistence, especially from the people who helped with reviewing and proof reading all the chapters. My sincere gratitude and thanks go to Marcel Arditi, Ayache Bouakaz, Marvin Doyley, Johan Kirkhorn, Chris de Korte and Fermin Lupotti, who spend extra time in reading the chapters. Their comments and suggestions are greatly appreciated.

Van het lab wil Klaas Bom bedanken voor zijn zorg dat dit proefschrift binnen afzienbare tijd geschreven is. Verder heb ik bewondering voor Charles Lancée omdat hij zich vol overgave kan storten op problemen die voor anderen te moeilijk zijn, Ton van der Steen vanwege zijn organisatie talent, Frits Mastik omdat zijn kennis op het gebied van alles wat met computers te maken heeft veel ellende voorkomt, Frans van Egmond omdat hij er steeds weer voor zorgt dat niemand op het lab het aan iets ontbreekt, Jan Honkoop die schema's van bijna alle elektronische apparaten uit z'n hoofd kent en daardoor alles repareren kan en Stéphane Carlier omdat hij onuitputtelijk lijkt. Verder bedank ik Chris de Korte vanwege zijn pioniers rol in alle zaken die te maken hebben met promoveren, waarvan ik de vruchten heb kunnen plukken, Corrie Eefting voor haar hulp bij alledaagse problemen en voor het corrigeren van de samenvatting, Fermin Lupotti because of the constant supply of cookies, and that I had the privilege of being your personal translator, Marvin Doyley for being a LaTeX expert and Peggy Palanchon, sorry that I ever said 'pattee' to 'foie gras'.

Sommige mensen hebben er nooit een probleem van gemaakt als er weer iets snel, tussendoor gedaan moest worden. Hiervoor ben ik dank verschuldigd aan Leo Bekkering, Jan Ekas, Wim van Alphen en Jan Honkoop voor het vervaardigen van de meest uiteenlopende onderdelen, Wim Vletter omdat hij altijd bereid is om iets nieuws te proberen en Rene Frowijn voor zijn 1-dag-dia service. Heleen van Beuzekom wil ik bedanken voor haar hulp en enthousiasme, Jolanda Wentzel voor haar gezelschap tijdens de vele 'bami/nasi-happen' en JHI, je had gelijk.

Special thanks to Xu Jingping, Marlies Goorden and Thomas Schuurmans for their help and contribution for acquiring the optical images. Thanks are also due to the people at Andaris Ltd., in particular Richard Johnson, Sarah Bailey and Siobhon Keating, who helped me during my stay in Nottingham.

De volgende mensen wil ik bedanken voor de prettige samenwerking en collegialiteit de afgelopen tijd: Kie Djoa, Sigmund Frigstad, Ceriel Haesen, Carola Janssen, Jarek Kasprzak, Trude Matla, Youssef Nosir en Li Wenguang.

Mijn ouders wil ik bedanken omdat ze me geleerd hebben om altijd iets af te maken waaraan je begonnen bent. Dit komt goed van pas tijdens het schrijven van een proefschrift. Als laatste ben ik veel dank verschuldigd aan Barbara vanwege haar steun, vertrouwen en interesse, maar vooral vanwege het geduld dat ze heeft weten op te brengen als ik weer eens geen tijd had.

# Curriculum vitae

Peter Frinking was born on September 6, 1966 in Bussum, The Netherlands. He completed his high school education in 1986 at the Samenwerkingsschool (Atheneum), Waddinxveen, The Netherlands. The same year, he served the army with the 59 Tank Battalion in 't Harde, The Netherlands.

In 1987, he started his study at the Delft University of Technology, faculty of Applied Physics. He obtained his Master of Science degree in 1994 at the Laboratory of Seismics and Acoustics headed by Prof.dr.ir. A.J. Berkhout. The subject of his Master's thesis was 'Integration of $L_1$ and $L_2$ filtering with applications to seismic data processing'.

In 1995, he started as a Ph.D. student (AIO) at the Erasmus Universiteit Rotterdam, at the Laboratory of Experimental Echocardiography, headed by Prof.dr.ir. N. Bom. The Ph.D. work focused on the characterization of ultrasound contrast agents and the application for diagnostic ultrasound imaging, and was supervised by Dr.ir. N. de Jong. From March 1, 2000, he will join Bracco Research S.A., Geneva, Switzerland.

# List of publications

## International journals

- P.J.A. Frinking, A. Bouakaz, N. de Jong, F.J. ten Cate and S. Keating, "Effect of ultrasound on the release of micro-encapsulated drugs," *Ultrasonics*, vol. 36, no. 1 5, pp. 709–712, 1998.

- P.J.A. Frinking and N. de Jong, "Acoustic Modeling of shell-encapsulated gas bubbles," *Ultrasound in Medicine and Biology*, vol. 24, no. 4, pp. 523–533, 1998.

- P.J.A. Frinking, N. de Jong and E.I. Céspedes, "Scattering properties of encapsulated gas bubbles at high ultrasound pressures," *Journal of the Acoustic Society of America*, vol. 105, no. 3, pp. 1989–1996, 1999.

- A. Bouakaz, P.J.A. Frinking, N. de Jong and N. Bom, "Non-invasive pressure measurement in a fluid filled cavity based on the disappearance time of micron-sized free gas bubbles," *Ultrasound in Medicine and Biology*, vol. 25, no. 9, pp. 1407–1415, 1999.

- N. de Jong, P.J.A. Frinking, and A. Bouakaz, "Imaging methods of ultrasound contrast agents," *Cardiology*, vol. 6, pp. 292 295, 1999.

- N. de Jong, P.J.A. Frinking, A. Bouakaz, and F.J. ten Cate, "Detection procedures of ultrasound contrast agents," Accepted for publication in: *Ultrasonics*, 1999.

- P.J.A. Frinking, E.I.Céspedes, J. Kirkhorn, H. Torp and N. de Jong, "A new ultrasound contrast imaging approach based on the combination of multiple imaging pulses and a separate release burst," Accepted for publication in: *IEEE Transactions on Ultrasonics Ferroelectrics and Frequency Control*, 1999.

- N. de Jong, P.J.A. Frinking and A. Bouakaz, "Optical imaging of contrast agent microbubbles in an ultrasound field with a 100 MHz camera," Accepted for publication in: *Ultrasound in Medicine and Biology*, 1999.

- P.J.A. Frinking, A. Bouakaz, J. Kirkhorn, F.J. ten Cate and N. de Jong, "Ultrasound contrast imaging: Current and new methods," Submitted to: *Ultrasound in Medicine and Biology*, 1999.

## Patents (pending)

- N. de Jong and P.J.A. Frinking, "Ultrasound contrast imaging," *WO 98/32378; PCT/GB98/00159.*
- P.J.A. Frinking, E.I. Céspedes and N. de Jong, "Improved ultrasound contrast imaging; method and apparatus," *WO 99/35967; PCT/GB99/00144.*
- N. de Jong and P.J.A. Frinking, "Improved ultrasound contrast imaging; method and apparatus," *Filed: Jan. 1999.*

## Awards

- P.J.A. Frinking, E.I. Céspedes and N. de Jong, "A new multi-pulse and decorrelation detection strategy for improved ultrasound contrast imaging," *Finalist of the Rotterdam Young Investigator Contrast Imaging Award, Third Thoraxcenter European Symposium on Ultrasound Contrast Imaging, Rotterdam, The Netherlands*, 1998.
- J. Kirkhorn, P.J.A. Frinking, N. de Jong and H. Torp, "Improving the sensitivity of power-Doppler for ultrasound contrast imaging by using a high power release burst," *Finalist of the Rotterdam Young Investigator Contrast Imaging Award, Fourth Heartcenter European Symposium on Ultrasound Contrast Imaging, Rotterdam, The Netherlands*, 1999.

## Conference proceedings

- N. de Jong, P.J.A. Frinking, F.J. ten Cate and P. van der Wouw, "Characteristics of contrast agents and 2D imaging," in *IEEE Ultrasonics Symposium Proceedings*, vol. 2, (San Antonio, USA), pp. 1449–1458, 1996.
- N. de Jong, P.J.A. Frinking, F.J. ten Cate and P. van der Wouw, "Characteristics of contrast agents and 2D imaging," *ThoraxCentre Journal*, vol. 9, no. 2, pp. 7 16, 1997.
- P.J.A. Frinking, A. Bouakaz, N. de Jong, F.J. ten Cate and S. Keating, "Ultrasound directed drug delivery," *ThoraxCentre Journal*, vol. 9, no. 2, pp. 23–25, 1997.
- P.J.A. Frinking and N. de Jong, "Modeling of ultrasound contrast agents," *IEEE Ultrasonics Symposium Proceedings*, vol. 2, (Toronto, Canada); pp. 1601–1604, 1997.
- N. de Jong, P.J.A. Frinking and F.J. ten Cate, "Properties of ultrasound contrast agents," *The Leading Edge in Diagnostig Ultrasound, Ultrasound Contrast Agents, 4$^{th}$ International Symposium Proceedings* (Atlantic City, USA), 1998.

- N. de Jong, P.J.A. Frinking and E.I. Céspedes, "Characteristics of ultrasound contrast agents," *16$^{th}$ International Congress on Acoustics and 135$^{th}$ Meeting Acoustical Society of America Proceedings*, vol. 3, (Seatle, USA), pp. 1829 1830, 1998.

- P.J.A. Frinking, E.I. Céspedes and N. de Jong, "Multi-pulse ultrasound contrast imaging based on a decorrelation detection strategy," *IEEE Ultrasonics Symposium Proceedings*, vol.2, (Sendai, Japan), pp. 1787–1790, 1998.

- A. Bouakaz, P.J.A. Frinking and N. de Jong, "Ultrasound imaging based on nonlinear pressure field properties," *15$^{th}$ International Symposium on Nonlinear Acoustics (ISNA) proceedings*, (Göttingen, Germany), 1999.

## Conference abstracts

- N. de Jong and P.J.A. Frinking, "Characteristics of contrast agents and 2D imaging," *1$^{st}$ European Symposium on Ultrasound Contrast Imaging*, Rotterdam, The Netherlands; 1996.

- N. de Jong, F.J. ten Cate, P. van der Wouw, P.J.A. Frinking and R. Johnson, "Characteristics of contrast agents and 2D imaging," *The 11$^{th}$ Annual Advances in Echocardiography: Contrast Echocardiography and Perfusion Imaging*, Chicago, USA, 1996.

- N. de Jong and P.J.A. Frinking, "Characteristics of contrast agents and 2D imaging," *IEEE Ultrasonics Symposium*, San Antonio, USA, 1996.

- L. Varga, F.J. ten Cate and P.J.A. Frinking, "Which conditions are needed for a successful left ventricle pacification and myocardial perfusion by using Quantison™," *2$^{nd}$ Thoraxcenter European Symposium on Ultrasound Contrast Imaging*, Rotterdam, The Netherlands, 1997.

- P.J.A. Frinking, N. de Jong and S. Keating, "Release of encapsulated x-ray contrast agent by ultrasound irradiation," *2$^{nd}$ Thoraxcenter European Symposium on Ultrasound Contrast Imaging* Rotterdam, The Netherlands, 1997.

- N. de Jong and P.J.A. Frinking, "Ultrasound contrast imaging," *2$^{nd}$ Thoraxcenter European Symposium on Ultrasound Contrast Imaging*, Rotterdam, The Netherlands, 1997.

- N. de Jong and P.J.A. Frinking, "Instrumentation characteristics in relation to echocardiography," *12$^{th}$ Symposium on Echocardiology and 9$^{th}$ Meeting of the International Cardiac Doppler Society*, Rotterdam, The Netherlands, 1997.

- N. de Jong and P.J.A. Frinking, "Properties of ultrasound contrast agents," *Ultrasonics International*, Delft, The Netherlands, 1997.

- P.J.A. Frinking, A. Bouakaz, N. de Jong, F.J. ten Cate and S. Keating, "Effect of ultrasound irradiation on the release of encapsulated drugs," *Ultrasonics International*, Delft, The Netherlands, 1997.

- S. Carlier, P.J.A. Frinking, R. Krams, E. Gailly and P.W. Serruys, "Improvement of coronary flow studies by the acquisition of raw Doppler signals and the use of echocontrast enhancement," *Europopean Heart*, Stockholm, Sweden, 1997.

- P.J.A. Frinking and N. de Jong, "Characteristics of contrast agents," *Congres of the World Federation of Ultrasound in Medicine and Biology*, Buenos Aires, Argentina, 1997.

- P.J.A. Frinking and N. de Jong, "Modelling of ultrasound contrast agents," *IEEE Ultrasonics Symposium*, Toronto, Canada, 1997.

- P.J.A. Frinking, E.I. Céspedes and N. de Jong, "A new multi-pulse and decorrelation detection strategy for improved ultrasound contrast imaging," *3rd Thoraxcenter European Symposium on Ultrasound Contrast Imaging*, Rotterdam, The Netherlands, 1998.

- H. van Beusekom and P.J.A. Frinking, "Survey of pathofysiological and physical principles for therapeutic delivery of drugs," *3rd Thoraxcenter European Symposium on Ultrasound Contrast Imaging*, Rotterdam, The Netherlands, 1998.

- A. Bouakaz, P.J.A. Frinking and N. de Jong, "Non-invasive pressure measurement in a cavity using encapsulated microspheres and a multi-pulse approach," *3rd Annual Ultrasound Contrast Research Symposium in Radiology*, San Diego, USA 1998.

- P.J.A. Frinking, N. de Jong and E.I. Céspedes, "Transient enhancement of scattering from encapsulated microbubbles insonified at high acoustic power," *Houston Society Of Biomedical Engineering*, Houston, USA, 1998.

- P.J.A. Frinking, E.I. Céspedes and N. de Jong, "Improved ultrasound contrast imaging using a new multi-pulse and decorrelation detection based strategy," *23rd International Symposium on Ultrasound Imaging and Tissue Characterization*, Virginia, USA, 1998.

- A. Bouakaz, P.J.A. Frinking and N. de Jong, "A new non-invasive technique for pressure measurement in a fluid filled cavity," *23rd International Symposium on Ultrasound Imaging and Tissue Characterization*, Virginia, USA, 1998.

- N. de Jong and P.J.A. Frinking, "Specific characteristics of ultrasound contrast agents," *16th International Congress on Acoustics and 135th Meeting of the Acoustical Society of America*, Seattle, USA, 1998.

- P.J.A. Frinking, E. I. Céspedes and N. de Jong, "High resolution multi-pulse contrast imaging based on a decorrelation detection strategy," *IEEE Ultrasonics Symposium*, Sendai, Japan, 1998.

- J. Kirkhorn, P.J.A. Frinking, N. de Jong and H. Torp, "Improving the sensitivity of power-Doppler for ultrasound contrast imaging by using a high power release burst," *The Fourth Heart Centre European Symposium on Ultrasound Contrast Imaging*, Rotterdam, The Netherlands, 1999.

- A. Bouakaz, P.J.A. Frinking, N. de Jong, "Non-invasive pressure measurement in a fluid filled cavity," *The Fourth Heart Centre European Symposium on Ultrasound Contrast Imaging*, Rotterdam, The Netherlands, 1999.

- N. de Jong and P.J.A. Frinking, "Subharmonic properties of ultrasound contrast agents," *The Fourth Heart Centre European Symposium on Ultrasound Contrast Imaging*, Rotterdam, The Netherlands, 1999.

- N. de Jong and P.J.A. Frinking, "Subharmonic imaging," *4$^{th}$ Annual Ultrasound Contrast Research Symposium in Radiology*, San Diego, USA, 1999.

- N. de Jong, P.J.A. Frinking and A. Bouakaz, "Imaging methods for ultrasound contrast agents," *Ultrasonics International*, Lyngby, Denmark, 1999.

- P.J.A. Frinking, A. Bouakaz and N. de Jong, "Measurements and simulations of subharmonic scattering of ultrasound contrast agents," *IEEE Ultrasonics Symposium*, Lake Tahoe, USA, 1999.

- J. Kirkhorn, P.J.A. Frinking, N. de Jong and H. Torp, "Improved ultrasound contrast detection combining harmonic power Doppler with a release burst," *IEEE Ultrasonics Symposium*, Lake Tahoe, USA, 1999.

- A. Bouakaz, C.T. Lancée, P.J.A. Frinking, and N. de Jong, "Numerical simulations of nonlinear pressure field generated by linear array transducers," *IEEE Ultrasonics Symposium*, Lake Tahoe, USA, 1999.

- A. Bouakaz, P.J.A. Frinking and N. de Jong, "Ultrasound imaging based on nonlinear pressure field properties," *15$^{th}$ International Symposium on Nonlinear Acoustics (ISNA)*, Göttingen, Germany, 1999.

- N. de Jong, P.J.A. Frinking and A. Bouakaz, "Nonlinear effects for UCA imaging," *1$^{st}$ International Kyoto Symposium on Ultrasound Contrast Imaging*, Kyoto, Japan, 1999.

- N. de Jong, P.J.A. Frinking and A. Bouakaz, "Subharmonic imaging," *1$^{st}$ International Kyoto Symposium on Ultrasound Contrast Imaging*, Kyoto, Japan, 1999.